UNIVERSITÀ DEGLI STUDI DI NAPOLI "FEDERICO II"

SCUOLA POLITECNICA E DELLE SCIENZE DI BASE

Department of Chemical, Materials and Industrial Production Engineering

PhD Thesis in
INDUSTRIAL PRODUCT AND PROCESS ENGINEERING
XXXII CYCLE

Multi-functional emulsion based nanocapsules for active targeting

Supervisor:
Prof. Paolo Antonio Netti
Advisor:
Dr. Ing. Raffaele Vecchione
Coordinator:
Prof. Giuseppe Mensitieri

PhD candidate:
Alberta De Capua

Academic years 2017-2020

TABLE OF CONTENTS

CHAPTER 1: Introduction

Nanotechnologies in the medical field: Nanomedicine

Cancer remains one of the leading causes of death worldwide. Over the past several decade significant advancements have been made in our fundamental understanding of cancer biology leading to better diagnostic and treatment methods. The main trouble is the inability to administer therapeutic agents selectively to the targeted diseased tissue without adverse effects on healthy sites. Up-to-date therapeutic strategies for cancer treatments involve a combination of surgical resection, radiation therapy, and chemotherapy. These therapies often fail to improve patient mortality and the incidence of many unpleasant diseases, primarily due to their non-specific effects on ‘‘normal’’ cells and because of the nonspecific distribution and rapid clearance of many anti-cancer agents[1]. The increase in efficacy of a therapeutic formulation is directly correlated to its ability to selectively target diseased tissue, overcome biological barriers, and ‘‘smartly respond’’ to the disease environment to release therapeutic agents. The intrinsic limits of conventional cancer therapies encouraged the development and application of various nanotechnologies for more effective and safer cancer treatments, herein referred to as *nanomedicine*[2]. Nanomaterials can be applied in nanomedicine for medical purposes in three different areas: diagnosis (nano-diagnosis), controlled drug delivery (nano-therapy), and regenerative medicine. A new area that combines diagnostics and therapy termed “theranostics” is emerging and it is a promising approach that holds in the same system both the diagnosis/imaging agent and the medicine[3].

Nanotechnology represents a powerful tool in the field of medicine, where it has been utilized for the development of novel drug delivery systems (DDS) through the entrapment of the pharmaceutical agent in nanoparticulate systems aimed to the treatments of a variety of diseases and disorders. Traditional drugs available now for oral or injectable administration are not always manufactured as the optimal formulation for each product because they contain proteins, nucleic acids or some bio-molecules that can be easily degraded in biological environment. The use of a drug delivery system is meant for the enhancement of loading and transport of therapeutic agents and overcome drawbacks of the agents, such as toxicity, low water solubility, and poor bioavailability due to physiological degradation[4]. Moreover, one of the most important advantages of nano-DDS is the capability to perform targeting by utilizing physiology of a normal tissue or pathophysiological properties unique of an ill tissue to address the nano-DDS to a specific target.

Nanoparticles (NPs) are generally defined as particulate materials of any shape with dimensions in the 1–100 nm range, as defined by the International Union of Pure and Applied Chemistry (IUPAC). Despite the size restriction, the term is commonly used for systems that are up to several hundred nanometers in size. NPs are mostly appealing for cancer treatments because they have several unique properties, which include high surface-to-volume ratio, high surface energy and unique mechanical, thermal, electrical, magnetic, and optical behaviors as well as biocompatibility, stability and possibility to incorporate hydrophilic and hydrophobic drugs if properly designed. These properties make them suitable for a wide range of applications, ranging from electronics, to energy harvesting and storage, to communications, to biology and medicine[5,2]. In recent years, outstanding progress has been made in developing new approaches to:

- Target drugs to tumor cells through surface ligands
- Increase localized delivery by increasing serum residence time.

Although these strategies have reduced systemic toxicity, significant improvement on delivery strategies is still necessary to increase patient compliance and reduce chemotherapy related side effects in cancer patients[6].

Different kinds of drug delivery systems (DDS)

A wide variety of nanoparticles composed of different materials including lipids, polymers and inorganic materials have been developed, as reported in Figure 1, resulting in delivery systems that vary in their physicochemical properties, each with its own advantages and limitations, but with the common purpose to enhance bioavailability, reduce drug toxicity, target to a particular organ, and increase the loading capacity and stability of the drug.
Anti-cancer NPs in clinical development can be broadly divided into different types: liposome, polymeric nanoparticles, polymeric micelles, and others, although there is some overlap between categories.

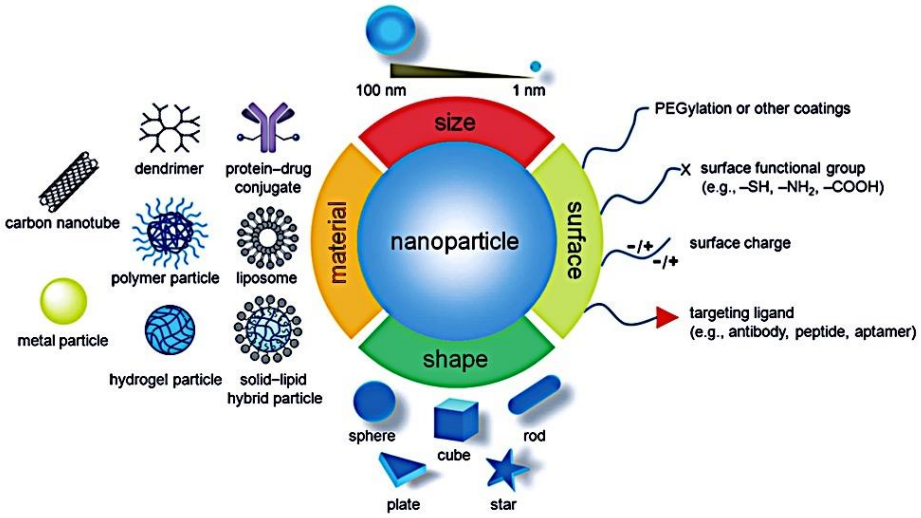

Figure 1: *A summary of nanoparticles that have been explored as carriers for drug delivery in cancer therapy, together with illustrations of biophysicochemical properties*[7]*.*

Liposome vesicles consist of single or multiple concentric phospholipid bilayers membranes, called lamellae, encapsulating an aqueous compartment. Their diameters range from 30 nm to several micrometres. Because of the amphipathic properties of lipids, the self-assembling of their hydrophobic sections into spherical bilayers in aqueous media is entropically driven[8]. Hydrophilic drugs can be encapsulated in the aqueous core by dissolving them in the liquid phase used for liposomes formation, while hydrophobic drugs can be integrated in the lipid bilayer by direct addition to the lipid solution, creating a layer of drug molecules between the lipid bilayer. Liposomes developed by Couvreur *et al.* were the first class of therapeutic NPs to receive clinical approval for Kaposi's sarcoma and ovarian cancer treatment, with the name of DOXIL in 1995[9,10], and along with other lipid based NPs, still represent a large proportion of clinical stage nanotherapeutics. The main advantages of this kind of nanocarrier that differentiates them from others, it's their mechanism of cellular crossing. In fact, the composition of lipid bilayer is

very similar to cellular membrane, so it is easy for the liposomes to fuse and internalize with the plasma membrane. Instead, some key limitations of liposomes include: their propensity to burst release cargo *in vivo*, a lack of compatibility with various active agents, a limited drug loading volume, the oxidation of liposomal phospholipids, and short half-life[11].

Nanoemulsions are a biphasic system in which one phase is dispersed in the other in the form of minute droplets, which generally have an average diameter between 50 and 500 nm[12]. The dispersed phase is also known as an internal phase or a discontinuous phase while the external phase is called dispersion medium or continuous phase. The term "nanoemulsions" (NEs) refers to the nanometric size of the droplets that constitute the fine dispersion of oil in water (O/W NEs) or water in oil (W/O NEs), stabilized by a surfactant which is placed at the interface between the two phases. Nanoemulsions are biodegradable, biocompatible, and used as carriers for lipophilic drugs that are prone to hydrolysis. Nanoemulsions are easily produced in large quantities by high shear stress or mechanical extrusion process that is available worldwide; and they can be obtained using surfactants approved for human consumption and common food substances that are “generally recognized as safe” (GRAS) by the the United States Food and Drug Administration FDA[13]. Nanoemulsions stability against sedimentation (or creaming) is achieved because the Brownian motion of the small droplet size and consequently the diffusion rate are higher than the sedimentation level induced by the gravity force[14]. Nanoemulsions are receiving increasing attention because they offer several advantages for the delivery of drugs; indeed, most of them that have been studied and developed for almost all routes of delivery (parenteral, oral, ocular, pulmonary and dermal deliveries) and are currently in clinical trials[15,16]. For example, Neoral® is an oral formulation developed by Novartis

that immediately forms a microemulsion in an aqueous medium. It improves cyclosporine bioavailability and reduces its pharmacokinetics/pharmacodynamics inter and intra patient variability, offering more predictable and more extensive drug absorption than the standard Sandimmune® (Novartis, AG Basel, Switzerland) formulation[17].

Polymeric nanoparticles are maybe some of the most studied carriers for drug delivery. They are composed of synthetic or natural biodegradable polymers whose properties, such as molecular weight, biodegradability and hydrophobicity can be modulated in a controllable way in order to obtain customized functionalization and controlled drug release[7,18]. Nanospheres are matrix-like systems in which the drug is dispersed within the polymer chains; instead nanocapsules are considered as a "reservoir" vesicular system constituted by a drug-containing liquid core (hydrophilic or lipophilic) surrounded by a single polymeric membrane[19]. In both cases, drugs are encapsulated in different ways like nanoprecipitation, electrospray, and emulsification[20]; without any chemical modification, differently from polymer-drugs conjugates. The most common polymers used are polylactic acid PLA, poly (glycolic acid) PGA, poly (lactic-co-glycolic acid) PLGA, polycaprolactone PCL and polyethylene glycol PEG.

Polymeric micelles are nanosized colloidal particle that can be formed by self-assembly of amphiphilic di- or tri- block copolymers in aqueous solution. The hydrophobic part of copolymers constitutes the core region of micelles that act as drug reservoir, while the hydrophilic segment forms the shell that stabilize the core. Micelles are characterized by a narrow stability range of concentrations, called critical micelle concentration (CMC), outside of which they disassemble[21].

Inorganic nanoparticles are another class of drug delivery system characterized by excellent physic-chemical properties. The most commonly used, include mesoporous silica nanoparticles (MSN), noble metals and carbon-based nanostructures. The honeycomb-like porous structure of MSN allows high loading capacity and a plethora of internal (pores) and external surface modifications[22]. Gold (Au) nanostructures possess photothermal properties, due to surface plasmon resonance phenomenon (SPR), that are significant for cancer therapy without the use of anticancer drugs[23]. Carbon nanotubes (CNTs) are tube of fullerene, a class of carbon allotropes, with diameters measured in nanometres range. Carbon nanotubes often refers to single-wall or multi-walled carbon nanotubes (SWCNTs or MWCNTs). CNTs exhibit remarkable electrical conductivity, exceptional tensile strength and thermal conductivity because of their nanostructure and strength of the bonds between carbon atoms. They have been used to deliver different kind of therapeutic agents[24] and targeting moieties including protein, peptides and RNA[25]. The intrinsic near-IR (NIR) light absorption property of CNTs has been used to destruct cancer cells, while NIR photoluminescence enables cell imaging and probing[26].

Layer-by-layer O/W NEs as drug delivery system

Polymeric materials formed via layer-by-layer (LbL) assembly have attracted interest for their use as drug delivery vehicles. These multilayered materials, both as capsules and thin films, can encapsulate a high payload of toxic or sensitive drugs, and can be readily engineered and functionalized with specific properties. In the early 1990s, Decher and his group were the first to develop LbL deposition of multilayer ultrathin organic films, with controlled thickness and composition, on a charged solid subrate[27]. This technique is based on the

electrostatic attraction between polyelectrolytes of opposite charge, whose main advantage is the precision, at nanometres level, of the final layer deposited[28]. In 1998, Donath and co-workers transferred LbL technique from planar films to spherical colloidal particles, paving the way to engineer new materials with unique and tuneable properties in terms of size, composition, colloidal stability, porosity and surface functionalization[29]. The strategy to produce LbL capsules consisted of sequential adsorption of oppositely charged polyelectrolytes around spherical templates followed by dissolution of the sacrificial template and production of hollow multilayer containers. The fact that the total number of charges on the adsorbed polyelectrolyte molecules is greater than that required to neutralize the opposite charges on the surface, means that charge reversal occurs. This overcompensation means that the adsorbing polyelectrolytes tend to form monolayers because once the surface has been saturated with polyelectrolytes there is an electrostatic repulsion between it and the non-adsorbed polyelectrolytes that prevents further adsorption. The application of LbL technique to O/W NEs paves the way to develop a nanocarrier that overcomes the problems of inner template removing and drug delivery. Nanoemulsions offer several advantages for drug delivery and are thus receiving increasing attention as carriers for improving the delivery of active pharmaceutical agents. However, emulsions do not typically have a sufficiently long shelf life because of destabilization mechanisms such as creaming, sedimentation and flocculation phenomenon occurred. Ostwald ripening or molecular diffusion, which arises from emulsion polydispersity and the difference in solubility between small and large droplets, is the main mechanism for nano-emulsion destabilization[14]. Several strategies of LbL implementation to emulsions have been proposed. For example McClements and his group in 2006 developed a secondary emulsions obtained with a polyelectrolyte thin layer, adsorbed on the surface of oil

droplets thanks to the interaction with an ionic emulsifier of opposite charge, that partially solved the stability issue[30]. An upgrade in his work occurred in 2011, when they proposed to use a high-pressure homogenizer (microfluidizer) for homogenised nanoemulsions, improving their stability[31].
Because of their ability to dissolve large quantities of hydrophobic drugs in the lipophilic oil phase, NEs are an ideal vehicle for drug delivery. Indeed, a lot of drugs, mainly anti-cancer ones, are hydrophobic molecules that difficulty can be delivered in human body, which it's principally composed by water. In addition, O/W NEs are able to protect drugs from hydrolysis and enzymatic degradation under physiological conditions. On this matter, our research group has made many efforts in developing nanoemulsions using only biodegradable and FDA approved materials. In 2014 we developed a novel multi re-dispersion process at high-pressure that allowed us to improve secondary emulsion homogeneity, monodispersion and stability, over time from a few weeks to several months, thanks to a tuneable polymer coating level[32]. They are applicable for almost all routes of delivery and therefore can be used in different fields from cosmetics, food and agriculture[33] to therapeutics and biotechnology.

Cancer targeting by nanoparticles

Conventional therapeutics are rapidly eliminated from the human body and suffer from widespread distribution into non-targeted organs and tissues, whereas targeted therapeutic NPs have gained promising attention through offering a new strategy to overcomes the challenges associated to drug delivery. In addition to circulation kinetics, drug release, and tumour clearance rates, the tumour exposure to NPs and its payload is ruled by access into the tumour, distribution across, and retention within the tumour.

Effective design of an ideal delivery system is the key foundation to overcome these barriers. Because of the complexity and the heterogeneity of malignant cells and tumours there are no generally applicable methods for targeting tumours and tumor cells (or their organelles)[34]. Unlike small molecules, nanoparticles cannot go through the tight junctions between endothelial cells on normal vascular linings, owing to their relatively large sizes[7]. The most important approach is based on the fact that many tumours and especially vascularized solid tumours as well as some vascularized metastatic tumor nodules, exhibit an enhanced permeability and retention (EPR) effect which is the basis for so-called "*passive targeting*". In 1986, Maeda and co-worker in studying the inflammation induced by microbial infections introduced the EPR effect for the first time, providing experimental evidence to support it[35]. This phenomenon occurs because many solid tumours have a leaky vasculature and absent or lessened lymphatic drainage, which permit the accumulation of high molecular weight molecules as well as small particles of diameter ~20–500 nm within the tumor tissue, thanks the increasing of permeability of vasculature; while tight junctions in normal vasculature prevent particles larger than 2 nm from crossing between endothelial cells, as reported in Figure 2. So, passive targeting is based on the combination of small size of drug carriers and the permeable vasculature of the tumours[36].

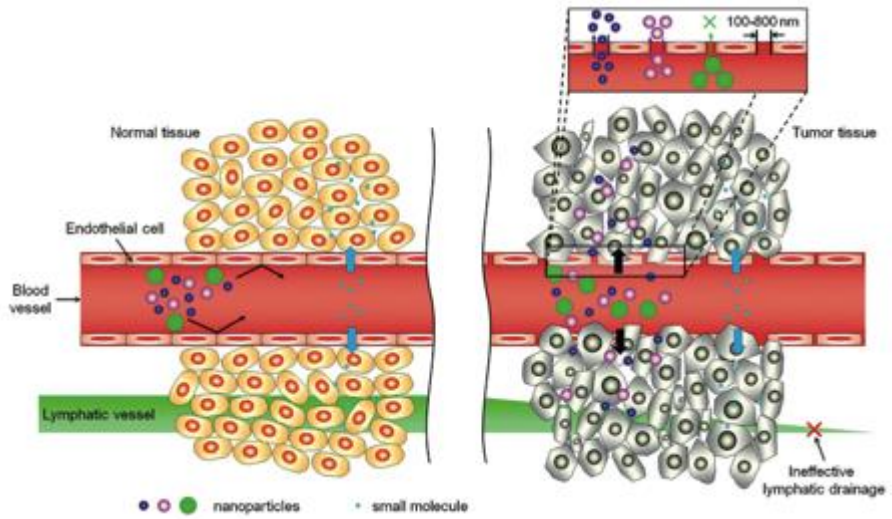

Figure 2: *Representation of EPR effect: transport of nanoparticles with different sizes and small molecules through normal (left) and tumoral (right) tissues.*

The main advantage gained by exploiting the EPR effect for drug delivery to solid tumours is its universality, which enables the DDS to be used in the treatment of diverse types of tumours. In order to achieve effective EPR mediated targeting, NPs must have long circulating half-lives for the passage of NPs from the systemic circulation into the more permeable regions of tumour vasculature. The reticuloendothelial system (RES) consists in a group of organs and circulating macrophages, whose main function is to eliminate foreign objects such as bacteria, toxins and so on from human body. Firstly, a kind of proteins available in the circulation called opsonins creates a protein-layer around foreign substances in a process called opsonisation, where a variety of interaction such as ionic, electrostatics, hydrophobic, hydrophilic and van de Waals forces are involved. Then, the macrophages recognize protein layer and proceed to engulf the foreign organism from bloodstream by sending them to lysosome for complete degradations[37]. The longer blood circulation time is the first requirement to be considered when designing NPs for drug delivery, because they should not be cleared from the body before its

interaction with tumor tissue. A well-established strategy used for escaping RES and improve the shelf-life in the blood steam of DDSs was their coating with poly(ethylene glycol) (PEG) chains[38]. PEG is a coiled polymer of repeating hydrophilic ethylene glycol units of neutral charge with dynamic conformations. Its chains reduce the typical charge-based contact with proteins and small-molecules eluding the rate of clearance from the blood circulation[39]. Numerous *in vivo* studies concerning PEG surface modified NPs are found[40,41,42]. Indeed, PEG has been currently listed as "Generally Recognized as Safe" (GRAS) by the FDA, making it particularly attractive to translational researchers[43].

Active targeting

Macromolecules, NPs and drug delivery systems captured in tumours due to the EPR effect do not act in a hugely selective way because there is not a specific receptor-ligand binding. Consequently, the term "targeting" should strictly be used in reference to a more complex mechanism called "*active targeting*". It is based on specific molecular recognitions between a membrane-bounding receptor, overexpressed at the surface of particular cells (e.g., cancer cells, brain endothelial cells *etc*.) and a complementary ligand that is exposed on the external side of the DDS, allowing the nanoparticle to selectively and strongly bind to the surface of a specific type of cells[7]. In this strategy, active targeting systems with ligands moieties exposed outside need to be accumulated first in tumor tissues by EPR effect and then active targeting could be achieved (Figure 3).

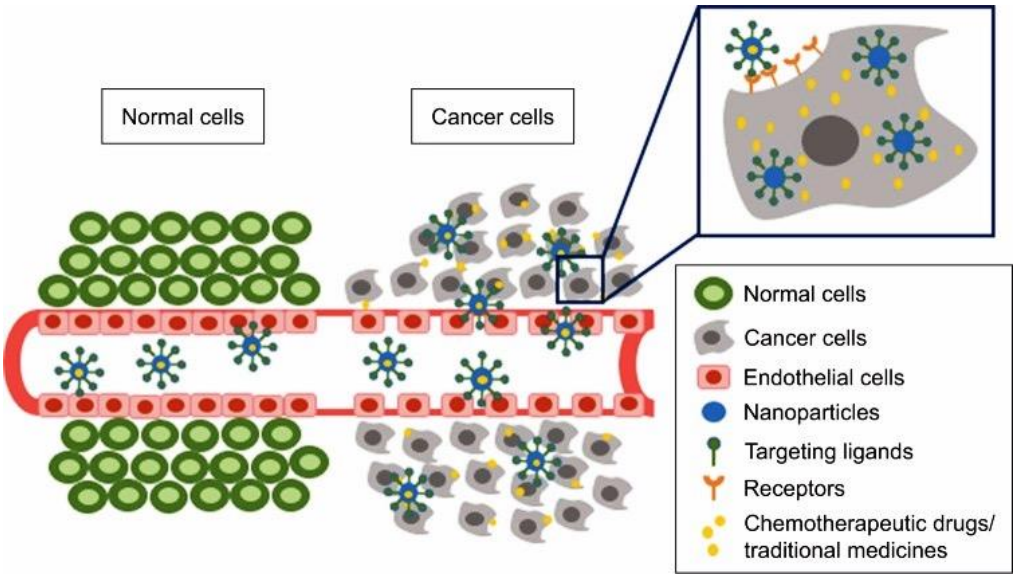

Figure 3: *Passive and active targeting mechanisms of nanoparticles[44].*

There are several ligands that are used to modify NPs like antibodies, engineered antibody fragments, proteins, peptides, small molecules and aptamers. Many techniques and tools are currently available for the functionalization of nanoparticles for the active targeting of cancer cells. The choice of a targeted ligand focuses on numerous considerations, including availability, ease of production, affinity, conjugation protocols and immunogenicity. All these parameters should be carefully evaluated when designing nanoparticles with good targeting capacity while minimizing the costs. Traditionally, monoclonal antibodies (mAb) have been used to target epitopes on the cell surface, but the extensive screening of peptide and aptamer libraries has greatly expanded the range of ligands available for active targeting. In addition to a large number of targeting ligands, there are also different modes for targeting. For example, epidermal growth factor receptor (EGFR) and human epidermal growth factor receptor 2 (HER2) are involved in cell proliferation and survival, and their over-expression in many tumors is associated with poor possibility of survival in many human cancers.

Cetuximab is an EGFR-specific mAb approved for several cancers, which acts by blocking the binding of activating ligand; in a different way, trastuzumab is a mAb that acts in a ligand-independent manner by blocking the association of HER2 with other EGFR family members[45,46].

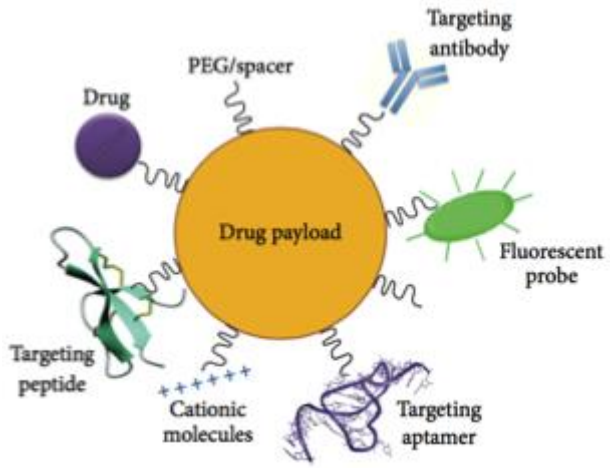

Figure 4: *Several kind of targeting moieties.*

The ligands currently used, as represented in Figure 4, include antibodies, fragments of antibodies, proteins, peptides, aptamers, oligosaccharides and even small molecules, provided that they recognize and specifically bind to an over-expressed target on the cells surface.

Different types of targeting moieties are largely used in engineered NPs:

Monoclonal antibodies (mAbs) are macromolecules widely used as ligands due to their high affinity and specificity for certain molecular targets. These ligands usually have a molecular weight of about 150 kDa and have high binding affinities to the corresponding antigens, with dissociation constants in nanomolar range ($k_d \sim 0.1$ nM) even with a low density at the surface of nanocarriers. The first reports of NPs functionalized with mAbs date back to

1980's and involved the surface modification of liposomes with mAbs that recognized antigens on the human target cells[47]. They are most widely employed in the active targeting strategy; in fact, 30 of them have been approved for clinical trials[48]. To date, mAbs have essentially been conjugated to many types of nanoparticles, such as SPION (Super Paramagnetic Iron Oxide Nanoparticles), quantum dots (QDs), liposomes, and gold-based nanocages, to give them specific site-targeting capabilities. However, the bulky dimensions and the redundant constant regions can cause some problems in the use of mAbs as a target of ligands due to their immunogenicity and increase in the overall size of the nanoparticles[49].

Transferrin (Tf) protein consists of a single polypeptide chain of 78-kDa molecular weight, organized into two domains of approximately equal size. It belongs to iron-binding class of glycoproteins that control iron (Fe) levels in biological fluids. It transports iron into the cells thanks to the formation of a complex with transferrin receptor (TfR). TfR is a membrane glycoprotein, consisting of two 90-kD subunits linked by disulfide bonds. The interaction between Tf and its receptor is reversible and pH-dependent. At physiological pH the Tf affinity for Fe is so high that the interaction is practically irreversible, but as the pH is lowered below 6.5, iron is released[50]. Transferrin is widely used as a ligand for active targeting. In fact, following the binding to the transferrin-receptor on the cell surface, it initiates endocytosis and it is internalized into the acidic compartments of cytoplasm where the iron dissociates. The transferrin receptor plays a vital role in regulating cell growth and is overexpressed in numerous types of malignant cells, up to 10 times higher than those in normal cells[51].

Aptamers are short oligomers of synthetic single-stranded nucleic acids, DNA or RNA, which can form complex three-dimensional structures and involve in

cell-surface ligand binding with high affinity and specificity. For example, NPs conjugated with aptamers have been developed for the delivery of cisplatin, a platinum-based chemotherapeutic drug, to prostate cancer cells. Compared to free cisplatin, the aptamer-NPs were 80 times more effectives[52] .

Endogenous ligands, such as folic acid and epidermal growth factor receptor (EGFR), are interesting for tumor targeting because they can bind to their respective receptors with low immunogenicity and high affinity. Several protocols have been published to combine these molecules to various types of nanoparticles[1].

Functionalization of the NPs surface with targeting moieties not only improves its accumulation on tumor site, but concurrently increases drug efficacy with a reduction of the dose needed providing a novel method to optimize drug pharmacokinetics[53]. Because the peptides were chosen as targeting moieties for this PhD project, it will be discussed more in detail in the next paragraph.

Peptides as ligand for active targeting

Peptides represent a viable targeting moiety because they provide several advantageous characteristics, including low molecular weight (ca. 1 kDa), tissue accumulation capability, lack of immunogenicity, ease of production with cost rather low, and relative flexibility in chemical conjugation processes. In addition, their small size is not likely to change the physicochemical properties of the resulting decorated nanocarriers. Various peptides have been used as homing devices in the fields of cancer targeting. Kessler *et al.* developed a cyclic peptide c-RGD whose specificity of binding to $\alpha_V\beta_3$ integrin receptor, highly expressed in tumor proliferating neovascular endothelial cells while minimally expressed in normal quiescent endothelial cells[54], was 170

times more active than the linear form[55]. An example of RGD-conjugated nanocarriers was reported by Hu and coworkers, which exhibited a significant anticancer activity *in vivo* without showing the systemic toxicity associated to conventional chemotherapies. Indeed, functionalized micelles of poly(lactic acid)–poly(ethylene oxide) PLA-b-PEO-RGD demonstrated a tumor regression in 62.5% of animals at the end of the treatment and in a better survival than other treatments[56]. K237 peptide functionalization of paclitaxel (PTX) loaded poly(ethylene glycol)–poly(lactide) PLA-b-PEG-NPs enabled the specific targeting to the vascular endothelial growth factor receptor (VEGFR) of tumor neovessels[57]. Because of the lack of specific markers in the tumor lymphatics, limited data are reported; with the sole exception of the peptide LyP-1 that has showed great targeting efficiency to cancer cells *in vitro.* Additionaly, when it is conjugated to PEG–PLGA nanoparticles it has showed promising results *in vivo* as carrier for target-specific drug delivery to lymphatic metastatic tumors [58,59].

Peptide shuttle for Blood brain barrier BBB

Brain delivery is one of the major challenges in the field of development of efficient drug delivery system because of the need to overcome the blood–brain barrier (BBB) to allow drugs to reach their targets in therapeutically relevant amounts[60]. The BBB is a physical, metabolic and transport barrier, mainly constituted by capillary made of endothelial cells that form tight junctions to hinder paracellular passage and tightly control the transfer of substances from blood to neural tissues and viceversa[61]. Many strategies have been proposed to bypass the BBB, including engineered NPs, to promote the accumulation of chemotherapeutic molecules in tumor tissue via receptor-mediated transcytosis (RMT), a well-known mechanism for trafficking macromolecules across the BBB[62]. One of these, consist in using peptides

functionalized vectors, also knows as peptide shuttle. Although some peptides had long been shown to cross the BBB, Stephen Dowdy and co-workers pioneered the field of peptide shuttles in 1999. The authors demonstrated the capacity of a peptide fragment derived from the human immunodeficiency virus (HIV) TAT protein to deliver β-galactosidase into the brain and other organs[63]. This paves the way to the discovery of a new class of peptides, named cell-penetrating peptides (CPPs), that owing to their amphipatic nature, full of cationic residue, can penetrate in the cell by interacting with negative charged plasmatic membrane[64,65]. The main limitation of this class of peptides is due to their failure to deliver functionalized NPs to a specific cellular site and recognize it, being able only to cross their membrane. Therefore, to bypass this issue it is important to also promote an active targeting towards the BBB. In particular, receptors with high expression on the BBB for which transcytosis have been largely evaluated include: transferrin (TfR)[66], low-density lipoproteins (LDLRs)[67] and insulin[68]. Among peptides targeting the family of LDLRs, the most promising is Angiopep-2. Several studies of Angiopep-2 conjugate for brain tumours diagnosis or treatments are reported, many of which are in clinical trials[69–72]. Many peptides able to target TfR have been discovered through phage display technology. Due to the overexpression of the TfR both in solid tumors and on the endothelial cells of the BBB, transferrin was used to target cancer cells and to achieve brain delivery[73]. One of these is B6 peptide that was the first one identified by Xia *et al.* in 2000 and successively conjugated to PEG-PLA NPs. It has been showed higher brain accumulation as compared to plain NPs (without peptide modification)[74,75]. In a more recent study, a 9-mer peptide targeting TfR named CRT peptide (CRTIGPSVC) was developed. It was accumulated in the brain after i.v. administration to mice, and it was reported that CRT peptide facilitated brain transport in a glioblastoma mouse model,

resulting in a significant decrease in tumor size[76]. Remarkably, in the last years over 30 BBB shuttle peptides with increasing efficiency and versatility have been reported[77].

CD44 receptor as bio-marker in cancer therapies

CD44 receptor belong to a family of non-kinase single span transmembrane glycoproteins, involved in multiple signalling pathways, cell–cell interactions, cell adhesion and migration. It is expressed on embryonic stem cells and in various levels on other cell types including connective tissues and bone marrow[78]. CD44 expression is also up regulated in subpopulations of cancer cells and can be expressed in its smallest standard isoform, CD44s, or as a number of alternatively spliced variant isoforms, CD44v isoforms that are overexpressed in many cancer types[79]. The main ligand for CD44 is hyaluronic acid (HA), an abundant component of the extracellular matrix (ECM) that is expressed by stromal and cancer cells. HA binds the CD44 ligand-binding domain inducing conformational changes that allow binding of adaptor proteins or cytoskeletal elements to intracellular domains that in turn activate various signalling pathways leading to cell proliferation, adhesion, migration, and invasion[80]. The multifunctional role of CD44 in maintaining stemness, in the cross talk with the tumor microenvironment and in the regulation of cancer, suggests that CD44 may also be an important prognostic marker. Therapeutic strategies that target CD44 or reduce CD44 expression are in various stages of clinical development. Currently, a number of new humanized anti-CD44 or anti-CD44v antibodies are under preclinical investigation for anti- cancer stem cells (CSC) therapy[78]. Only a few peptides able to specifically bind to CD44 receptor are reported. Among these, RP-1 peptide (WHPWSYLWTQQA) exhibited affinity and specificity to CD44 on gastric cancer cells and tissues[81]. A6 is an eight L-amino acid peptide (Ac-KPSSPPEE-

NH2) derived from human urokinase plasminogen activator (uPA), that act in an independent way, without interfering with uPA binding to its correspondent receptor (uPAR)[82]. A6 binds to CD44 resulting in the inhibition of migration, invasion, and metastasis of tumor cells, and the modulation of CD44-mediated cell signalling. A6 has demonstrated efficient results for several treatments and an excellent safety profile in phases of clinical trials. Indeed, it is now examined in a trial phase II study for its efficacy in the treatment of human ovarian cancer[83,84]. The most promising is the laminin α5 chain-derived peptide A5G27 (in the next chapters named CD44 binding peptide, CD44BP), which bound specifically to the glycosaminoglycan (GAG) side chains of CD44v3 and CD44v6 and attenuate tumor cell migration and invasion, but also block the binding of tumor-supporting growth factors to membrane CD44, preventing their involvement in the malignant cascade[85–88].

Peptide based active targeting in nanoemulsions

To the best of my knowledge only few studies of NEs with targeting ligands have been reported so far. Mulder *et al.* developed a glucocorticoid prednisolone acetate valerate (PAV) loaded O/W NEs, which also carried iron oxide nanocrystals for MRI and the fluorescent dye Cy7 for NIRF imaging, for "theranostic" purpose. Indeed, when nanoemulsions were functionalized with RGD peptides, angiogenesis-targeted nanoemulsions have shown significant accumulation in the tumors, while tumor growth profiles revealed a potent inhibitory effect[89]. Mansoor Amiji *et al.* provided another example of peptide functionalization of O/W NEs. The peptide CREKA, which shows selective targeting of fibrin clots that are observed in atherosclerotic lesions, was integrated on a novel ω-3- fatty acid-rich, 17-β-estradiol (17-βE)-loaded nanoemulsions. The system has demonstrated potential therapeutic activity

against atherosclerosis by reducing the size of lesions and the gene expression of inflammatory markers associated with the disease[90,91].

Application of nanotechnologies in nutraceutical field

A further important point that we have investigated was the encapsulation of nutraceutical natural substances in the O/W nanoemulsions. The term "nutraceutical" was coined in 1989 by Stephen De Felice, founder of the American Foundation for Innovation in Medicine. He defined a nutraceutical as a "food, or parts of a food, that provide medical or health benefits, including the prevention and treatment of disease"[92]. In other word, a functional food is any food or food component providing health benefits beyond basic nutrition. Accumulating evidence has suggested that dietary consumption of nutraceuticals is associated with decreased risks of multiple chronic diseases. In addition, most of the nutraceuticals, being natural substance, exhibit relatively less toxicity and secondary side effects than conventional synthetic drugs used in similar pathological states. However, due to their lipophilic nature, many nutraceuticals have poor bioavailability in human body, which significantly lowers their efficacy as disease-preventing agents[93]. Indeed, the oral bioavailability of a nutraceutical agent is defined as its fraction that actually reaches the systemic (blood) circulation in an active form. An effective way to overcome these limitations is to utilize nanotechnology to encapsulate nutraceuticals in engineered nanoparticles based delivery systems. In the case of oral delivery, the first barrier that a nutraceutical need to get through is the gastrointestinal tract (GI), where it suffered of physiochemical transformations in the composition and structure that could affect its activity[94]. Thus it could be very innovative to combine nutraceuticals with engineered oral delivery systems to protect nutraceuticals from adverse GI

conditions and improve the bioavailability of phytochemicals changing their pharmacokinetics and biodistribution. A wide variety of nutraceuticals, are known to possess several anti-inflammatory, antioxidant and anticancer properties summarized in the Table 1.

Table 1: *Common nutraceuticals that exhibit beneficial properties*[95].

Nutraceutical	Major activities
Apigenin	Antioxidative, vasoprotective, antiinflammatory, hypocholesterolemic
Naringin	Vasoprotective, antiinflammatory, hypocholesterolemic
Ursolic acid	Antioxidative, antimicrobial, antiinflammatory
Hesperidin	Vasoprotective, antiinflammatory
Piperine	Antiinflammatory, respiratory diseases, digestive, absorptive
Eucalyptol	Gastroprotective, antiinflammatory, antioxidative, hepatoprotective
Curcumin	Antioxidative, antiinflammatory, anticarcinogenic
Eugenol	Antioxidative, antiinflammatory
Diosgenin	Antioxidative, antiinflammatory, anticarcinogenic
Diallyl sulfide	Antioxidative, antiinflammatory, anticarcinogenic
Gingerol	Antioxidative, antiinflammatory, cardioprotective, antimicrobial
Thymoquinone	Antiinflammatory, anticancer
Garcinol	Antioxidative, antiinflammatory, anticarcinogenic
Capsaicin	Antioxidative, antiinflammatory
Rosmarinic acid	Antiinflammatory, respiratory diseases
Gossypin	Antioxidant, antinociceptive, antiinflammatory, anticarcinogenic

Extensive research within the last two decades has revealed that curcumin exhibits anti-oxidative, anti-inflammatory, anti-apoptotic, anti-proliferative, anti-invasive, and anti-angiogenic activity[96]. However, as mentioned above, the curcumin used for both oral and intravenous administration is limited by its low bioavailability because of its lipophilic nature and its poor stability in aqueous solutions. Several delivery systems have been studied to increase the bioavailability of curcumin, including nanoparticles, liposomes, and micelles[97]. In 2016, our group designed a new nanometric formulation of O/W NEs loaded with curcumin combined with the alkaloid piperine, stabilized by a layer of chitosan. This formulation was resistance to the GI and displayed adhesive properties towards the intestinal lumen, was developed and

biologically tested (*in vitro* and *in vivo*). In this study an enhanced anti-inflammatory action of curcumin for oral delivery was demonstrated, which was 64 times higher than unformulated one, the highest level ever reached[98]. In the last years, much interest has also been addressed to health benefits of tomato that contain about 80% of dietary amount of its major antioxidant component that is lycopene[99]. Strong antioxidative and other *in vitro* and *in vivo* beneficial effects of lycopene are associated with its ability to act as free radical scavengers because it can delocalize the highly reactive free electron along the conjugated 13 double bonds[100]. Indeed, free radicals are highly reactive, short-lived molecules that can damage essential structural proteins, enzymes, and DNA. Such damage has the potential to cause cancer, atherosclerosis, cardiovascular, and other diseases. More recently, we have investigated the cardio-protective effects of nanoemulsions loaded with lycopene extract[101]. In this study we demonstrated that lycopene loaded nanoemulsions protect against cardiotoxicity induced by chemotherapeutic treatments, by reducing inflammation and lipid oxidative stress. In recent years, another nutritional supplement that has attracted much attention for its properties was the Coenzyme Q_{10} (CoQ_{10} ubiquinone-10). CoQ_{10} plays the essential role of electron carrier and proton translocation during cellular respiration and ATP production and protects numerous cellular membranes and plasma lipoproteins against free radical-induced damage. It is the only endogenously synthesized antioxidant existing in all cell membranes of our body[102]. As well as curcumin and many of nutraceuticals, also CoQ_{10} is affected by delivery problems due to their low bioavailability. Kazuhito Kajiwara *et al.* emulsified CoQ_{10} with different fats and emulsifiers commonly used in the food industry, and compared their oral bioavailability with that of a standard commercial product. The oral bioavailability of emulsified CoQ_{10} of micrometric dimensions, was slightly greater than that of a commercial

product[103]. The stability of the emulsions depended on the types of fat, emulsifier, and aqueous system but it is limited overtime. In this scenario, last part of my PhD project was focused on cardioprotection and hepatoprotection properties of CoQ_{10} encapsulated in our multilayer polymeric coated O/W NEs to prevent or support oncological patients during the clinical treatment. In addition, the curcumin was used as anticancer natural substance to perform biological test of peptide functionalized LbL O/W bilayer.

Aim of PhD thesis

The following PhD project regards the field of the drug delivery systems. In particular, the aim of this project was the development of a versatile multi-functional emulsion based nanocapsules for active targeting. The main purpose is the use of safe nanocarriers, made of completely biodegradable and biocompatible materials, to improve the therapy efficacy and the bioavailability of the drugs, which is correlated to its ability to selectively target, with specific moieties, diseased tissue without affecting healthy sites, reducing the side effects for the patient. O/W NEs are an ideal carrier for drug delivery thanks to their ability to dissolve hydrophobic drugs and natural substances like curcumin, lycopene and coenzyme Q_{10}, and protect their cargo from hydrolysis and enzymatic degradation under physiological conditions. The stabilization of O/W NEs by means of a natural polymer coating, obtained through the layer by layer (LbL) methodology, is extremely important to obtain a product stable enough to build up dimensionally controllable multilayer nanocapsules of interest for nanomedicine.

In **chapter 2** the development of an innovative tool based on an O/W core-LbL bilayer shell made of completely biodegradable materials is reported. It was functionalized with biotin moieties on the external layer constituted by

hyaluronic acid, in order to exploit streptavidin-biotin affinity, and therefore expose any kind of ligands outside the nanocapsules. A complete thermodynamic characterization of streptavidin interaction with biotinylated tool was performed by isothermal titration calorimetric (ITC) analysis.

The **chapter 3** and **chapter 4** were focused on the use of such O/W NEs engineered with peptides for active targeting via the biotin-streptavidin strategy. In other words, it consists in the attachment of peptides to the outer surface of O/W NEs that become able to specifically bind to target receptors present on cell surface. Two receptors have been considered: CD44, highly over-expressed in many cancer cells; and transferrin receptor (TfR) over-expressed on the blood brain barrier (BBB). In both cases, two peptide sequences, able to recognize them, were identified. Thanks to high binding affinity with biotin, streptavidin was used as linker to conjugate the synthetized peptide to the entire systems, using a decoration strategy, while keeping nano-carrier stability. Biological tests demonstrated that peptide functionalized O/W NEs are able to accumulate and internalize in specific cells, when specific peptides are exposed, thanks to ligand-receptor binding.

Finally, in the **chapter 5** the use of O/W NEs to support oncological patients during the clinical treatment was investigated. In this scenario, it was demonstrated the cardioprotective and hepatoprotective effects of Coenzyme Q_{10} loaded O/W NEs against Doxorubicin and Trastuzumab toxicities. O/W NEs showed high stability and loading ability, increasing cell viability both in hepatocytes and cardiomyocytes during anticancer treatments. The future upgrade in this case will be to use the abovementioned coating strategy with peptides able to selectively target liver and/or cardiovascular tissues. For example, a targeting peptide (CREKA) that it is reported to specifically bind to fibrin in microthrombus and stroma of tumors[104,105], highly expressed in the infarcted mouse myocardium has been already identified. Indeed, it is

reported that CRKEA functionalized NPs favoured Tβ4 (43-amino-acid-sequestering peptide that increased cardiac function by promoting the survival of cardiomyocytes) accumulation and retention in the infarcted region, leading to augmented functional benefits[106].

In summary, during this PhD project, we propose a modular system, which may add complexity by exploiting its capability to further deposit layers and provide multi-functionality.

References

1. Kanapathipillai, M., Brock, A. & Ingber, D. E. Nanoparticle targeting of anti-cancer drugs that alter intracellular signaling or influence the tumor microenvironment. *Adv. Drug Deliv. Rev.* **79–80**, 107–118 (2014).

2. Shi, J., Kantoff, P. W., Wooster, R. & Farokhzad, O. C. Cancer nanomedicine : progress , challenges and opportunities. *Nat. Publ. Gr.* **17**, 20–37 (2016).

3. Soares, S., Sousa, J., Pais, A. & Vitorino, C. Nanomedicine: Principles, Properties, and Regulatory Issues. *Front. Chem.* **6**, (2018).

4. Rizvi, S. A. A. & Saleh, A. M. Applications of nanoparticle systems in drug delivery technology. *Saudi Pharm. J.* **26**, 64–70 (2018).

5. Chen, G., Roy, I., Yang, C. & Prasad, P. N. Nanochemistry and Nanomedicine for Nanoparticle-based Diagnostics and Therapy. (2016).

6. Steichen, S. D., Caldorera-Moore, M. & Peppas, N. A. A review of current nanoparticle and targeting moieties for the delivery of cancer therapeutics. *Eur. J. Pharm. Sci.* **48**, 416–427 (2013).

7. Sun, T. *et al.* Engineered nanoparticles for drug delivery in cancer therapy. *Angew. Chemie - Int. Ed.* **53**, 12320–12364 (2014).

8. Akbarzadeh, A. *et al.* Liposome: classification, preparation, and applications. *Nanoscale Res. Lett.* **8**, 102 (2013).

9. Barenholz, Y. (Chezy). Doxil® — The first FDA-approved nano-drug: Lessons learned. *J. Control. Release* **160**, 117–134 (2012).

10. Couvreur, P., Kante, B., Grislain, L., Roland, M. & Speiser, P. Toxicity of Polyalkylcyanoacrylate Nanoparticles II: Doxorubicin-Loaded Nanoparticles. *J. Pharm. Sci.* **71**, 790–792 (1982).

11. Daraee, H., Etemadi, A., Kouhi, M., Alimirzalu, S. & Akbarzadeh, A. Application of liposomes in medicine and drug delivery. *Artificial Cells, Nanomedicine and Biotechnology* **44**, 381–391 (2016).

12. Lovelyn, C. & Attama, A. A. Current State of Nanoemulsions in Drug Delivery. *J. Biomater. Nanobiotechnol.* **02**, 626–639 (2011).

13. Ganta, S., Talekar, M., Singh, A., Coleman, T. P. & Amiji, M. M. Nanoemulsions in Translational Research—Opportunities and Challenges in Targeted Cancer Therapy. *AAPS PharmSciTech* **15**, 694–

708 (2014).

14. Solans, C., Izquierdo, P., Nolla, J., Azemar, N. & Garcia-Celma, M. J. Nano-emulsions. *Current Opinion in Colloid and Interface Science* **10**, 102–110 (2005).

15. Lovelyn, C. & Attama, A. A. Current State of Nanoemulsions in Drug Delivery. *J. Biomater. Nanobiotechnol.* **2**, 626–639 (2011).

16. Hörmann, K. & Zimmer, A. Drug delivery and drug targeting with parenteral lipid nanoemulsions - A review. *Journal of Controlled Release* **223**, 85–98 (2016).

17. Hafner, A., Lovrić, J., Perina Lakoš, G. & Pepić, I. Nanotherapeutics in the eU: an overview on current state and future directions. *Int. J. Nanomedicine Dovepress* **9**, 1005–1023 (2014).

18. Din, F. U. *et al.* Effective use of nanocarriers as drug delivery systems for the treatment of selected tumors. *Int. J. Nanomedicine* **12**, 7291–7309 (2017).

19. Letchford, K. & Burt, H. A review of the formation and classification of amphiphilic block copolymer nanoparticulate structures: micelles, nanospheres, nanocapsules and polymersomes. *European Journal of Pharmaceutics and Biopharmaceutics* **65**, 259–269 (2007).

20. Tran, S., DeGiovanni, P.-J., Piel, B. & Rai, P. Cancer nanomedicine: a review of recent success in drug delivery. *Clin. Transl. Med.* **6**, 44 (2017).

21. Nicolas, J., Mura, S., Brambilla, D., Mackiewicz, N. & Couvreur, P. Design, functionalization strategies and biomedical applications of targeted biodegradable/biocompatible polymer-based nanocarriers for drug delivery. *Chem. Soc. Rev.* **42**, 1147–1235 (2013).

22. Watermann, A. & Brieger, J. Mesoporous Silica Nanoparticles as Drug Delivery Vehicles in Cancer. *Nanomater. (Basel, Switzerland)* **7**, (2017).

23. Noguez*, C. Surface Plasmons on Metal Nanoparticles: The Influence of Shape and Physical Environment. (2007).

24. Feazell, R. P., Nakayama-Ratchford, N., Dai, H. & Lippard, S. J. Soluble Single-Walled Carbon Nanotubes as Longboat Delivery Systems for Platinum(IV) Anticancer Drug Design. *J. Am. Chem. Soc.* **129**, 8438–8439 (2007).

25. Bianco, A., Kostarelos, K. & Prato, M. Applications of carbon nanotubes

in drug delivery. *Curr. Opin. Chem. Biol.* **9**, 674–679 (2005).

26. Shi Kam, N. W., O'Connell, M., Wisdom, J. A. & Dai, H. Carbon nanotubes as multifunctional biological transporters and near-infrared agents for selective cancer cell destruction. *Proc. Natl. Acad. Sci.* **102**, 11600–11605 (2005).

27. Decher, G. & Hong, J. D. Buildup of Ultrathin Multilayer Films by a Self-Assembly Process: II. Consecutive Adsorption of Anionic and Cationic Bipolar Amphiphiles and Polyelectrolytes on Charged Surfaces. *Berichte der Bunsengesellschaft für Phys. Chemie* **95**, 1430–1434 (1991).

28. Del Mercato, L. L. *et al.* Biological applications of LbL multilayer capsules: From drug delivery to sensing. *Advances in Colloid and Interface Science* **207**, 139–154 (2014).

29. Donath, E., Sukhorukov, G. B., Caruso, F., Davis, S. A. & Möhwald, H. Novel Hollow Polymer Shells by Colloid-Templated Assembly of Polyelectrolytes. *Angew. Chemie Int. Ed.* **37**, 2201–2205 (1998).

30. Guzey, D. & McClements, D. J. Formation, stability and properties of multilayer emulsions for application in the food industry. *Advances in Colloid and Interface Science* **128–130**, 227–248 (2006).

31. Qian, C. & McClements, D. J. Formation of nanoemulsions stabilized by model food-grade emulsifiers using high-pressure homogenization: Factors affecting particle size. *Food Hydrocoll.* **25**, 1000–1008 (2011).

32. Vecchione, R. *et al.* Tunable stability of monodisperse secondary O/W nano-emulsions. *Nanoscale* **6**, 9300–9307 (2014).

33. Yukuyama, M. N., Ghisleni, D. D. M., Pinto, T. J. A. & Bou-Chacra, N. A. Nanoemulsion: process selection and application in cosmetics - a review. *Int. J. Cosmet. Sci.* **38**, 13–24 (2016).

34. Ulbrich, K., Vladimir, S. & Bakandritsos, A. Targeted Drug Delivery with Polymers and Magnetic Nanoparticles : Covalent and Noncovalent Approaches , Release Control , and Clinical Studies. (2016). doi:10.1021/acs.chemrev.5b00589

35. MATSUMOTO, K., YAMAMOTO, T., KAMATA, R. & MAEDA, H. Pathogenesis of Serratial Infection: Activation of the Hageman Factor-Prekallikrein Cascade by Serratial Protease. *J. Biochem.* **96**, 739–749 (1984).

36. Xu, X., Ho, W., Zhang, X., Bertrand, N. & Farokhzad, O. Cancer

nanomedicine : from targeted delivery to combination therapy. *Trends Mol. Med.* **21**, 223–232 (2015).

37. Owens, D. E. & Peppas, N. A. Opsonization, biodistribution, and pharmacokinetics of polymeric nanoparticles. *Int. J. Pharm.* **307**, 93–102 (2006).

38. Mori, A., Klibanov, A. L., Torchilin, V. P. & Huang, L. Influence of the steric barrier activity of amphipathic poly(ethyleneglycol) and ganglioside GM1 on the circulation time of liposomes and on the target binding of immunoliposomes in vivo. *FEBS Lett.* **284**, 263–266 (1991).

39. Jokerst, J. V, Lobovkina, T., Zare, R. N. & Gambhir, S. S. Nanoparticle PEGylation for imaging and therapy. *Nanomedicine (Lond)* **6**, 715–728 (2011).

40. Chithrani, D. B. Polyethylene Glycol Density and Length Affects Nanoparticle Uptake by Cancer Cells Optimizing 2D tissue models View project Optimization of interface between nanotechnology and cancer therapy View project. (2014).

41. Ding, Y. *et al.* The performance of thiol-terminated PEG-paclitaxel-conjugated gold nanoparticles. *Biomaterials* **34**, 10217–10227 (2013).

42. Liong, M. *et al.* Multifunctional inorganic nanoparticles for imaging, targeting, and drug delivery. *ACS Nano* **2**, 889–896 (2008).

43. Kamaly, N., Xiao, Z., Valencia, P. M., Radovic-Moreno, A. F. & Farokhzad, O. C. Targeted polymeric therapeutic nanoparticles: Design, development and clinical translation. *Chemical Society Reviews* **41**, 2971–3010 (2012).

44. Muhamad, N., Plengsuriyakarn, T. & Na-Bangchang, K. Application of active targeting nanoparticle delivery system for chemotherapeutic drugs and traditional/herbal medicines in cancer therapy: A systematic review. *International Journal of Nanomedicine* **13**, 3921–3935 (2018).

45. Kintzing, J. R., Filsinger Interrante, M. V. & Cochran, J. R. Emerging Strategies for Developing Next-Generation Protein Therapeutics for Cancer Treatment. *Trends in Pharmacological Sciences* **37**, 993–1008 (2016).

46. Kim, J. W. & Cochran, J. R. Targeting ligand–receptor interactions for development of cancer therapeutics. *Current Opinion in Chemical Biology* **38**, 62–69 (2017).

47. Leserman, L. D., Barbet, J., Kourilsky, F. & Weinstein, J. N. Targeting to cells of fluorescent liposomes covalently coupled with monoclonal antibody or protein A. *Nature* **288**, 602–604 (1980).

48. ClinicalTrials.gov. Available at: https://www.clinicaltrials.gov/. (Accessed: 6th September 2019)

49. Zhong, Y., Meng, F., Deng, C. & Zhong, Z. Ligand-Directed Active Tumor-Targeting Polymeric Nanoparticles for Cancer Chemotherapy. *Biomacromolecules* **15**, 1955–1969 (2014).

50. Moos, T. & Morgan, E. H. Transferrin and Transferrin Receptor Function in Brain Barrier Systems. *Cell. Mol. Neurobiol.* **20**, 77–95 (2000).

51. Sahoo, S. K., Ma, W. & Labhasetwar, V. Efficacy of transferrin-conjugated paclitaxel-loaded nanoparticles in a murine model of prostate cancer. *Int. J. Cancer* **112**, 335–340 (2004).

52. Dhar, S., Gu, F. X., Langer, R., Farokhzad, O. C. & Lippard, S. J. Targeted delivery of cisplatin to prostate cancer cells by aptamer functionalized Pt(IV) prodrug-PLGA–PEG nanoparticles. *Proc. Natl. Acad. Sci.* **105**, 17356–17361 (2008).

53. Chow, E. K.-H. & Ho, D. Cancer Nanomedicine: From Drug Delivery to Imaging. *Sci. Transl. Med.* **5**, 216rv4-216rv4 (2013).

54. Brooks, P. C., Clark, R. A. F. & Cheresh, D. A. Requirement of vascular integrin αvβ3for angiogenesis. *Science (80-.).* **264**, 569–571 (1994).

55. Haubner, R. *et al.* Cyclic RGD Peptides Containing β-Turn Mimetics. *J. Am. Chem. Soc.* **118**, 7881–7891 (1996).

56. Hu, Z. *et al.* Arg-Gly-Asp (RGD) peptide conjugated poly(lactic acid)-poly(ethylene oxide) micelle for targeted drug delivery. *J. Biomed. Mater. Res. Part A* **85A**, 797–807 (2008).

57. Yu, D. H., Lu, Q., Xie, J., Fang, C. & Chen, H. Z. Peptide-conjugated biodegradable nanoparticles as a carrier to target paclitaxel to tumor neovasculature. *Biomaterials* **31**, 2278–2292 (2010).

58. Laakkonen, P., Porkka, K., Hoffman, J. A. & Ruoslahti, E. A tumor-homing peptide with a targeting specificity related to lymphatic vessels. *Nat. Med.* **8**, 751–755 (2002).

59. Luo, G. *et al.* LyP-1-conjugated nanoparticles for targeting drug delivery to lymphatic metastatic tumors. *Int. J. Pharm.* **385**, 150–156 (2010).

60. Pardridge, W. M. Drug Transport across the Blood–Brain Barrier. *J. Cereb. Blood Flow Metab.* **32**, 1959–1972 (2012).

61. Abbott, N. J., Patabendige, A. A. K., Dolman, D. E. M., Yusof, S. R. & Begley, D. J. Structure and function of the blood-brain barrier. *Neurobiology of Disease* **37**, 13–25 (2010).

62. Kang, T. *et al.* Enhancing Glioblastoma-Specific Penetration by Functionalization of Nanoparticles with an Iron-Mimic Peptide Targeting Transferrin/Transferrin Receptor Complex. *Mol. Pharm.* **12**, 2947–2961 (2015).

63. Schwarze, S. R., Ho, A., Vocero-Akbani, A. & Dowdy, S. F. In vivo protein transduction: Delivery of a biologically active protein into the mouse. *Science (80-.).* **285**, 1569–1572 (1999).

64. Heitz, F., Morris, M. C. & Divita, G. Twenty years of cell-penetrating peptides: from molecular mechanisms to therapeutics. *Br. J. Pharmacol.* **157**, 195–206 (2009).

65. Milletti, F. Cell-penetrating peptides: Classes, origin, and current landscape. *Drug Discovery Today* **17**, 850–860 (2012).

66. Ming Qian, Z. & Sun, H. *Targeted Drug Delivery via the Transferrin Receptor-Mediated Endocytosis Pathway*. (2002).

67. Dehouck, B. *et al.* A new function for the LDL receptor: Transcytosis of LDL across the blood-brain barrier. *J. Cell Biol.* **138**, 877–889 (1997).

68. Duffy, K. R. & Pardridge, W. M. Blood-brain barrier transcytosis of insulin in developing rabbits. *Brain Res.* **420**, 32–38 (1987).

69. Ren, J. *et al.* The targeted delivery of anticancer drugs to brain glioma by PEGylated oxidized multi-walled carbon nanotubes modified with angiopep-2. *Biomaterials* **33**, 3324–3333 (2012).

70. Gao, H. *et al.* Angiopep-2 and Activatable Cell-Penetrating Peptide Dual-Functionalized Nanoparticles for Systemic Glioma-Targeting Delivery. *Mol. Pharm.* **11**, 2755–2763 (2014).

71. Bertrand, Y. *et al.* Influence of glioma tumour microenvironment on the transport of ANG1005 via low-density lipoprotein receptor-related protein 1. *Br. J. Cancer* **105**, 1697–1707 (2011).

72. Ruan, S. *et al.* Tumor microenvironment sensitive doxorubicin delivery and release to glioma using angiopep-2 decorated gold nanoparticles.

Biomaterials **37**, 425–435 (2015).

73. Nicolas, J., Mura, S., Brambilla, D., MacKiewicz, N. & Couvreur, P. Design, functionalization strategies and biomedical applications of targeted biodegradable/biocompatible polymer-based nanocarriers for drug delivery. *Chemical Society Reviews* **42**, 1147–1235 (2013).

74. Xia, H., Anderson, B., Mao, Q. & Davidson, B. L. Recombinant Human Adenovirus: Targeting to the Human Transferrin Receptor Improves Gene Transfer to Brain Microcapillary Endothelium. *J. Virol.* **74**, 11359–11366 (2000).

75. Liu, Z. *et al.* B6 Peptide-Modified PEG-PLA Nanoparticles for Enhanced Brain Delivery of Neuroprotective Peptide. *Bioconjug. Chem.* **24**, 997–1007 (2013).

76. Staquicini, F. I. *et al.* Systemic combinatorial peptide selection yields a non-canonical iron-mimicry mechanism for targeting tumors in a mouse model of human glioblastoma. *J. Clin. Invest.* **121**, 161–173 (2011).

77. Oller-Salvia, B., Sánchez-Navarro, M., Giralt, E. & Teixidó, M. Blood-brain barrier shuttle peptides: An emerging paradigm for brain delivery. *Chemical Society Reviews* **45**, 4690–4707 (2016).

78. Yan, Y., Zuo, X. & Wei, D. Concise Review: Emerging Role of CD44 in Cancer Stem Cells: A Promising Biomarker and Therapeutic Target. *Stem Cells Transl. Med.* **4**, 1033–1043 (2015).

79. Jothy, S. CD44 and its partners in metastasis. *Clinical and Experimental Metastasis* **20**, 195–201 (2003).

80. Chen, C., Zhao, S., Karnad, A. & Freeman, J. W. The biology and role of CD44 in cancer progression: Therapeutic implications. *J. Hematol. Oncol.* **11**, 1–23 (2018).

81. Zhang, D. *et al.* A CD44 specific peptide developed by phage display for targeting gastric cancer. *Biotechnol. Lett.* **37**, 2311–2320 (2015).

82. Orian-Rousseau, V. & Ponta, · H. Perspectives of CD44 targeting therapies. *Arch Toxicol* **3**, 3–14 (2015).

83. Ghamande, S. A. *et al.* A phase 2, randomized, double-blind, placebo-controlled trial of clinical activity and safety of subcutaneous Å6 in women with asymptomatic CA125 progression after first-line chemotherapy of epithelial ovarian cancer. *Gynecol. Oncol.* **111**, 89–94 (2008).

84. Gold, M. A. *et al.* A phase II study of a urokinase-derived peptide (A6) in the treatment of persistent or recurrent epithelial ovarian, fallopian tube, or primary peritoneal carcinoma: A Gynecologic Oncology Group study. in *Gynecologic Oncology* **125**, 635–639 (2012).

85. Hibino, S. *et al.* Identification of an active site on the laminin α5 chain globular domain that binds to CD44 and inhibits malignancy. *Cancer Res.* **64**, 4810–4816 (2004).

86. Hibino, S. *et al.* Laminin α5 chain metastasis- and angiogenesis-inhibiting peptide blocks fibroblast growth factor 2 activity by binding to the heparan sulfate chains of CD44. *Cancer Res.* **65**, 10494–10501 (2005).

87. Kusuma, N., Anderson, R. L. & Pouliot, N. Laminin α5-derived peptides modulate the properties of metastatic breast tumour cells. *Clin. Exp. Metastasis* **28**, 909–921 (2011).

88. Makino, M. *et al.* Identification of cell binding sites in the laminin α5-chain G domain. *Exp. Cell Res.* **277**, 95–106 (2002).

89. Gianella, A. *et al.* Multifunctional Nanoemulsion Platform for Imaging Guided Therapy Evaluated in Experimental Cancer. *ACS Nano* **5**, 4422–4433 (2011).

90. Deshpande, D., Kethireddy, S., Janero, D. R. & Amiji, M. M. Therapeutic Efficacy of an ω-3-Fatty Acid-Containing 17-β Estradiol Nano-Delivery System against Experimental Atherosclerosis. *PLoS One* **11**, e0147337 (2016).

91. Deshpande, D., Kethireddy, S., Gattacceca, F. & Amiji, M. Comparative pharmacokinetics and tissue distribution analysis of systemically administered 17-β-estradiol and its metabolites in vivo delivered using a cationic nanoemulsion or a peptide-modified nanoemulsion system for targeting atherosclerosis. *J. Control. Release* **180**, 117–124 (2014).

92. Pandey, M., Verma, R. K. & Saraf, S. A. Nutraceuticals: new era of medicine and health. *Artic. Asian J. Pharm. Clin. Res.* (2010).

93. Yao, M., McClements, D. J. & Xiao, H. Improving oral bioavailability of nutraceuticals by engineered nanoparticle-based delivery systems. *Current Opinion in Food Science* **2**, 14–19 (2015).

94. Ting, Y., Jiang, Y., Ho, C. T. & Huang, Q. Common delivery systems for enhancing in vivo bioavailability and biological efficacy of nutraceuticals. *Journal of Functional Foods* **7**, 112–128 (2014).

95. Nair, H. B. *et al.* Delivery of antiinflammatory nutraceuticals by nanoparticles for the prevention and treatment of cancer. *Biochemical Pharmacology* **80**, 1833–1843 (2010).

96. Sagar, S. M., Yance, D. & Wong, R. K. Natural health products that inhibit angiogenesis: A potential source for investigational new agents to treat cancer - Part 2. *Curr. Oncol.* **13**, 14–26 (2006).

97. Anand, P., Kunnumakkara, A. B., Newman, R. A. & Aggarwal, B. B. Bioavailability of Curcumin: Problems and Promises. *Mol. Pharm.* **4**, 807–818 (2007).

98. Vecchione, R. *et al.* Curcumin bioavailability from oil in water nano-emulsions: In vitro and in vivo study on the dimensional, compositional and interactional dependence. *J. Control. Release* **233**, 88–100 (2016).

99. Friedman, M. Anticarcinogenic, cardioprotective, and other health benefits of tomato compounds lycopene, α-tomatine, and tomatidine in pure form and in fresh and processed tomatoes. *Journal of Agricultural and Food Chemistry* **61**, 9534–9550 (2013).

100. Zhang, J. *et al.* Assessment of free radicals scavenging activity of seven natural pigments and protective effects in AAPH-challenged chicken erythrocytes. *Food Chem.* **145**, 57–65 (2014).

101. Quagliariello, V. *et al.* Cardioprotective Effects of Nanoemulsions Loaded with Anti-Inflammatory Nutraceuticals against Doxorubicin-Induced Cardiotoxicity. *Nutrients* **10**, 1304 (2018).

102. Lee, B. J., Huang, Y. C., Chen, S. J. & Lin, P. T. Coenzyme Q10 supplementation reduces oxidative stress and increases antioxidant enzyme activity in patients with coronary artery disease. *Nutrition* **28**, 250–255 (2012).

103. Thanatuksorn, P., Kawai, K., Hayakawa, M., Hayashi, M. & Kajiwara, K. Improvement of the oral bioavailability of coenzyme Q10 by emulsification with fats and emulsifiers used in the food industry. *LWT - Food Sci. Technol.* **42**, 385–390 (2009).

104. Zhang, B. *et al.* Fibrin-targeting peptide CREKA-conjugated multi-walled carbon nanotubes for self-amplified photothermal therapy of tumor. *Biomaterials* **79**, 46–55 (2016).

105. Chung, E. J. *et al.* Fibrin-binding, peptide amphiphile micelles for targeting glioblastoma. *Biomaterials* **35**, 1249–1256 (2014).

106. Huang, Z. *et al.* Targeted delivery of thymosin beta 4 to the injured myocardium using creKa-conjugated nanoparticles. *Int. J. Nanomedicine* 12–3023 (2017).

CHAPTER 2: Development of a novel drug delivery system based on Layer by Layer Oil-in-Water Nanoemulsions

Introduction

In the last years, nanotechnologies have been widely diffused in many fields, such as, engineering, chemistry, physics, biology, and medicine. In particular it is important to underline that especially in the field of medicine, nanotechnology can provide a new horizon for the development of innovative solutions for diagnostic and therapeutic applications[1,2]. To this aim, many kinds of engineered nanoparticles have been developed such as polymeric NPs, liposomes, silica NPs and gold nanoparticles. Much effort has been made for the development of novel drug delivery systems aimed to the treatment of a variety of diseases and disorders[3]. One of the main hurdles to be overcome is the entrapment of pharmaceutical agents. Indeed, due to their high hydrophobicity, almost 50% of powerful active substances approved for use, have a very low aqueous solubility, that restricts their appropriate absorption and bioavailability[4]. A wide variety of drug carriers have been developed as a mean of improving the therapeutic efficacy of encapsulated drugs. The possibility to confine the hydrophobic drugs within a nanocapsule not only improves their solubility in the blood and thus the bioavailability, but also the effectiveness because of the possibility to localize the nano-encapsulated drug with following reduction of the required dose and therefore of the side effects[5]. Another factor, which largely influences NPs biodistribution in the human body, is the dimension that should be in the nanometer range,

particularly below 200 nm. In this prospect, oil in water nanoemulsions (O/W NEs) fulfil many requirements to be an excellent candidate as drug delivery system such as good biocompatibility, biodegradability, and ease of large-scale production. O/W NEs can incorporate hydrophobic and amphipathic drugs at high concentrations, because of their heterogeneous composition of two immiscible liquids whose droplets were stabilized by an emulsifier[6]. However, emulsions do not present a long-term stability, because they are susceptible to destabilization phenomena such as flocculation, sedimentation, coalescence, and Ostwald ripening[7]. In order to improve the shelf life of O/W NEs for their biomedical applications as liquid templates for multilayer depositions, it is crucial to finely control both their size and polydispersity. To this aim, in 2014, our research group, managed to optimize the liquid–liquid interfaces in O/W NEs exploiting the advantages of the classical layer by layer (LbL) technique[8,9]. It consists in the progressive deposition of polyelectrolytes with opposite charge held together by electrostatic interactions and/or hydrogen bonding above the oil template, keeping on controlling precisely the thickness of polymer layers at nanometer level. Through LbL strategy, highly controllable polymer nanocapsules, with appropriate dimensions and monodispersity, stable over time have been developed so far. In cancer therapy, biodegradable polymer nanocapsules are interesting tool largely used for a series of advantages such as high payload, protection of drugs, long circulation in the blood and possibility to be easily functionalized for active targeting and improve their selectivity towards the tumour site. In addition, it is reported that LbL nanocapsules made of hydrophilic polymers like polysaccharides, can delay RES clearance and facilitate the enhanced permeation and retention (EPR)-based passive diffusion of nanocarriers in interstitial tumours[10]. The starting point for the design of a nanocarrier able to distinguish pathological

tissues without damaging healthy ones was the integration of targeting moieties on their external surface. It was reported that a large number of nanoemulsions are marketed as drug delivery systems able to actively target cells or tissues[11].

For this purpose, in 2017, our group developed a nanocarrier based on an O/W NEs coated with a layer of biotinylated polylysine and functionalized with a membranotropic peptide (gH625), in order to enhance cytosolic localization. The decoration strategy used to build up this carrier was based on the streptavidin–biotin affinities[12]. Specific applications of the streptavidin–biotin interaction based on detection, immobilization, and drug delivery are largely reported[13,14]. This project thesis aims at combining the advantages deriving from LbL technique to reach multilayer polymer nanocapsules with not only the desired sizes (below to 150 nm), but also the right value of PdI (<0.1), stable over time and the implementation of biotin-streptavidin strategy to upgrade the developed system for several applications in the medical field. In this work, we developed an innovative tool based on an O/W core-LbL bilayer shell, which is functionalized with biotin moieties, in order to exploit streptavidin-biotin technology. Firstly a chitosan (CT) layer was deposited on oil core and stabilized by a homogenization process as described in a previous article[15]. Then, a biotin tag was conjugated to the second polymer layer constituted by hyaluronic acid (HA), which was deposited alternately to form a bilayer multi-shell. HA is a high molecular weight bio-polysaccharide, discovered in 1934, by Karl Meyer in the vitreous of bovine eyes[16]. It has received great attention in medical and cosmetic applications because it possesses superior inert property as compared to other polysaccharides and exhibited high antifouling stability (i.e. against fibronectin adsorption)[17]. Subsequently, a complete thermodynamic

characterization of streptavidin interaction with biotinylated tool was performed by isothermal titration calorimetric (ITC) analysis. Finally, to study the dimensional properties and validate the possibility to attach any ligand to streptavidin-coated nanocapsules, we chose a biotinylated-PEG linker as model molecule.

Results and discussion

Synthesis and characterization of biotinylated hyaluronic acid

Hyaluronic acid (250 kDa) was functionalized with biotin hydrazide in order to produce a biotinylated nanocapsules (NCs) coating. Biotin-HA was prepared in an aqueous phase via carbodiimide chemistry. This approach uses a water-soluble carbodiimide (EDC) that catalyzes the formation of amide bonds between carboxylic acids of HA and amines of biotin hydrazide, by activating the carboxylate to form an O-acylisourea intermediate, stabilized by addition of N-hydroxysuccinimide (NHS) in coupling protocols, to avoid fast hydrolysis[18]. A schematic representation of the coupling reaction is shown in Figure 1. Because the HA degradation in acidic (pH < 1.6) and basic (pH > 12.6) medium is widely reported in literature, the reaction was conducted at mild conditions of pH ~ 6. This choice was also dictated by the gel-like behavior of HA shown at pH 2.5 due to the cooperative formation of hydrogen-bond network when the net charge of the polymer decreases[19,20]. The reaction product and the functionalization degree were detected by nuclear magnetic resonance (NMR).

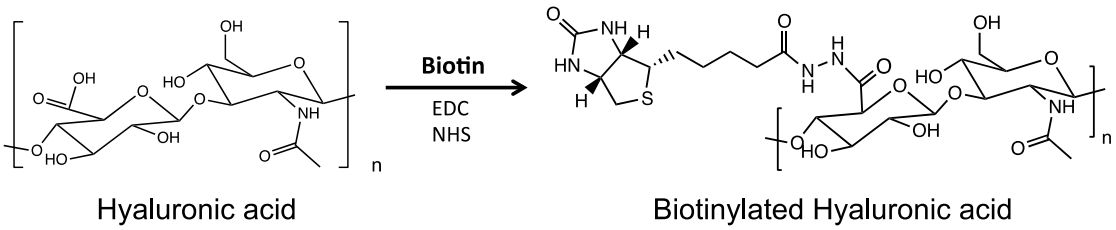

Figure 1: *Schematic representation of Hyaluronic acid functionalization with biotin.*

Firstly, we acquired the ^{1}H NMR spectra of biotin hydrazide to define the chemical shift of its protons. In Figure 2, the experimental NMR analysis of biotin hydrazide is reported. A summary of chemical shift δ assignments, integrals and coupling constant J of biotin hydrazide spectra is reported in the Table 1.

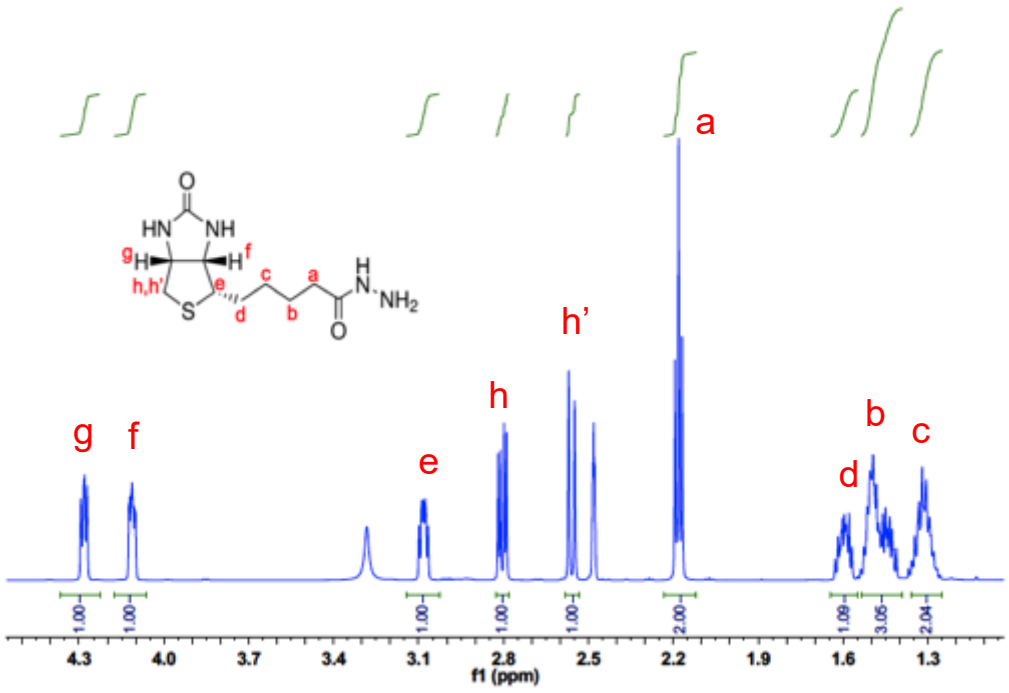

Figure 2: *1H1D NMR spectra analysis of biotin hydrazide in 90/10 H_2O/D_2O. Green lines represent the peak integration.*

Table 1: *^1H Chemical shift δ, integral and coupling constant J of biotin hydrazide in 90/10 H_2O/D_2O.*

Name	δ	H's	Integral	Class	J's
H c	1.30	2	2.04	m	
H b	1.47	3	3.05	m	
H d	1.59	1	1.09	m	
H a	2.18	2	2.00	t	7.4, 7.4
H h'	2.56	1	1.00	d	12.4
H h	2.80	1	1.00	dd	5.1, 12.4
H e	3.08	1	1.00	m	
H f	4.11	1	1.00	m	
H g	4.28	1	1.00	m	

This analysis was considered as reference point for next interpretation of biotinylated-HA NMR spectra. As previously mentioned, hyaluronic acid was conjugated with the biotin hydrazide and characterized by NMR analysis. In Figure 3, the experimental NMR analysis of biotinylated hyaluronic acid is depicted.

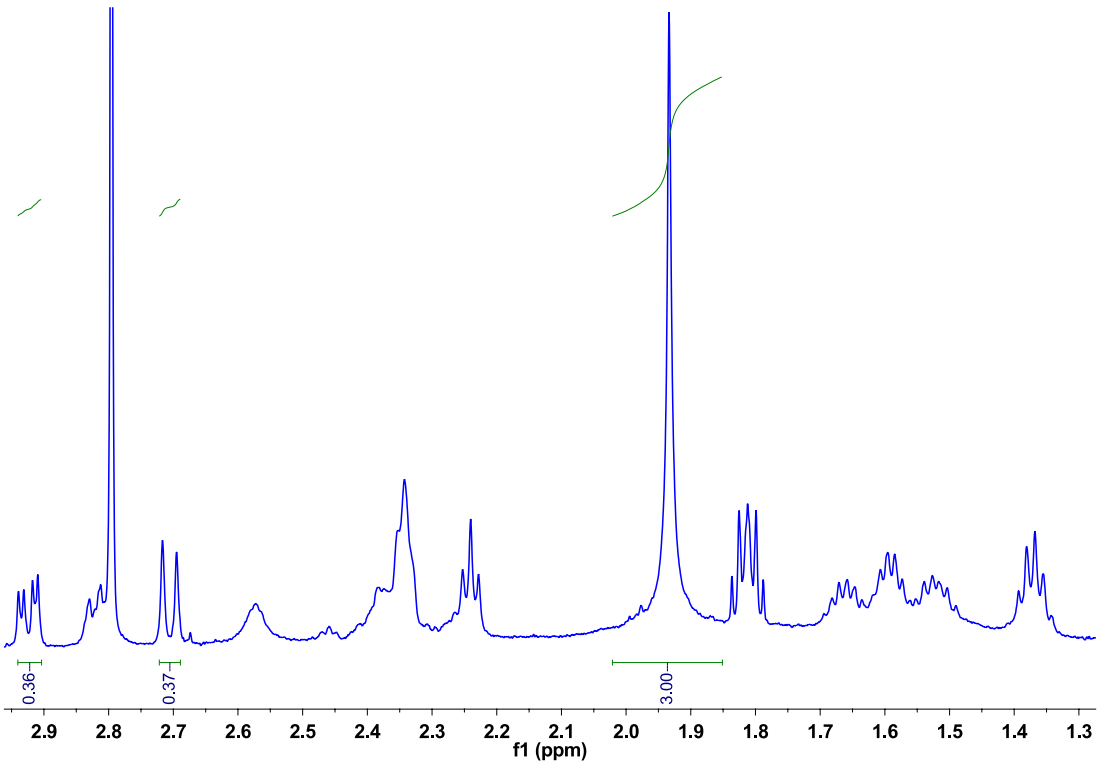

Figure 3: *1H1D NMR spectra analysis of biotinylated hyaluronic acid in 90/10 H_2O/D_2O. Green lines represent the peak integration.*

The peak at chemical shift δ 1.91 ppm was assigned to the acetyl group of HA whereas the doublet at 2.68 ppm and the doublet of doublet at 2.90 ppm was assigned to the protons H *h* and H *h'* of biotin, respectively. The hydrogen H *h* is coupled with the other H *h'* atom and appear as a doublet, while H *h'*, in addition to being coupled to H *h* (confirmed by the same coupling constant J=13), it is also coupled with the proton *g* appearing as doublet of doublet. The peaks integration shown in figure 3 was normalized respect to the number of protons of acetyl group, which was assigned to a value of three. So, thanks to the relative integration of the peaks assigned to biotin protons, we calculated the percentage of biotin bound to HA in the biotinylated sample, showing a

yield of functionalization of 37%, in accordance with Prestwich *et al.,* that obtained a degree of substitution of 0.33 mole of biotin for mole of HA[19]. All details of NMR analysis are summarized in the Table 2.

Table 2: *^{1}H Chemical shift δ, integral and coupling constant J of biotinylated HA in 90/10 H_2O/D_2O.*

Name	δ	H's	Integral	Class	J's
Acetyl group of HA	1.91	8	7.56	s	
H *h* of Biotin	2.68	1	0.98	d	13.00
H *h'* of Biotin	2.90	1	1.00	dd	4.93, 13.08

Multilayer deposition of polymers onto O/W NEs

In our research group, an innovative protocol to deposit a layer of chitosan around the oil template, preserving long-term stability thanks to the implementation of a multi re-dispersion high-pressure process, was developed so far. Furthermore, a novel approach to tune the O/W NEs dimensions based on the amount of surfactant (lecithin) concentration was also previously developed. A reproducible size control was attained for different formulations, from around 160 nm, with the lowest concentration of lecithin (1.9 g, named L_1), to around 90 nm with the highest one (5.8 g, named L_4)[21]. Once functionalized with biotin, hyaluronic acid was used to build up a polymer bilayer around the oil core of O/W NE. Firstly, we started using NEs with an intermediate lecithin concentration (L_2, 140 nm) to validate polymers deposition protocol. The saturation method[22] was used to study the optimal concentrations ratio between CT and biotinylated HA for the formation of consecutive polyelectrolytes layers, kept together by electrostatic forces, using layer by layer technique[21]. Figure 4 shows size; PdI and Z-potential data of

bilayers coated NEs at different percentage (wt %) of biotinylated HA deposited on the monolayer L_2 0.01 wt % CT-1 wt % O/W NEs.

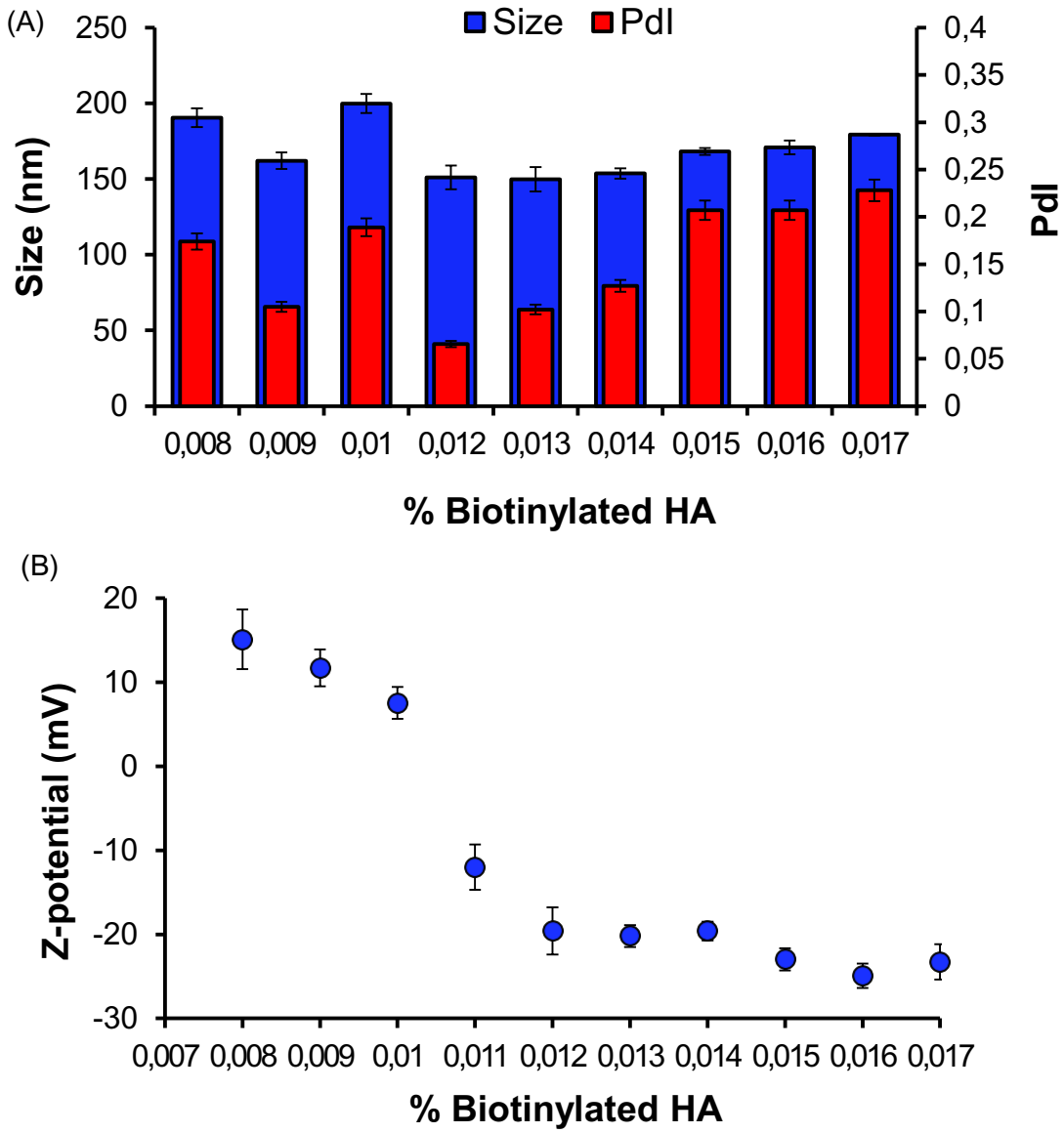

Figure 4: *DLS Size (A) and Z-Potential (B) data of biotinylated HA at different percentage deposited on monolayer L_2 0.01 wt % CT-1 wt % O/W NEs. Data are reported as mean (n=3) ± SD.*

The charge switches from a positive value (+ 15.1 mV) to a negative one, until a plateau is observed, as consequence of the complete biotinylated HA coating above the positive chitosan layer. Dimensional analysis shows that when the monolayer is not completely covered by hyaluronic acid, or there is an excess of polymer deposition, a destabilization of the system is observed (size around 200 nm and a PdI value that largely exceed the 0.1 value). So the optimum ratio between HA and CT concentrations (wt %), in term of size (< 160 nm), PdI (< 0.1) and Z-potential (~ -30 mV), is 2.4. A comparison between biotinylated and no-biotinylated multilayer system is shown in Figure 5. The size of biotinylated and non-biotinylated HA bilayer systems were comparable.

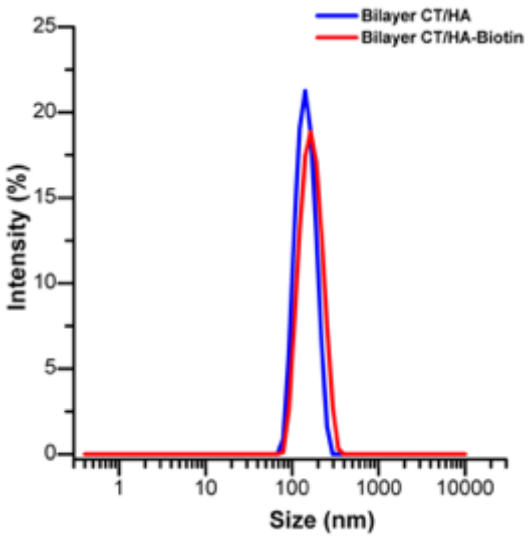

	Size (nm)	PdI	Z-potential (mV)
Bilayer CT-HA	141.2 ± 3.4	0.046 ± 0.004	-21.7 ± 4.5
Bilayer CT-HA-biotin	151 ± 7.9	0.065 ± 0.013	-22.9 ± 1.3

Figure 5: *Comparison of DLS size and Z-Potential data between bilayer 0.012 wt% HA-biotin-0.005 wt% CT-0.5% O/W NEs and bilayer 0.012 wt% HA-0.005 wt% CT-0.5% O/W NEs. Data are reported as mean (n=3) ± SD.*

Once dentifying the optimum conditions, in terms of size stability and Z-potential, to reach the deposition of two polymer layers, we aimed to reduce the dimensions of multi-layers coated O/W NEs. Therefore, we investigated their dimensional behaviour as a result of biotinylated HA depositions above the chitosan coated O/W NEs formulations made with the smallest nanoemulsion size (L_4). In Figure 6, size and Z-potential of the bilayer with biotinylated HA deposition, at different polymer concentrations, on L_4 0.01 wt % CT-1 wt % O/W NEs are shown. We observe a similar trend, which confirms that, also in this case, the optimum ratio between HA and CT concentrations remains 2.4. Therefore, the size-scalability of our tool and its narrow distribution was verified. It was demonstrated on two different nanoemulsions template (L_2 and L_4), but we would expect the same trend in a wider range of nanoemulsions dimensions.

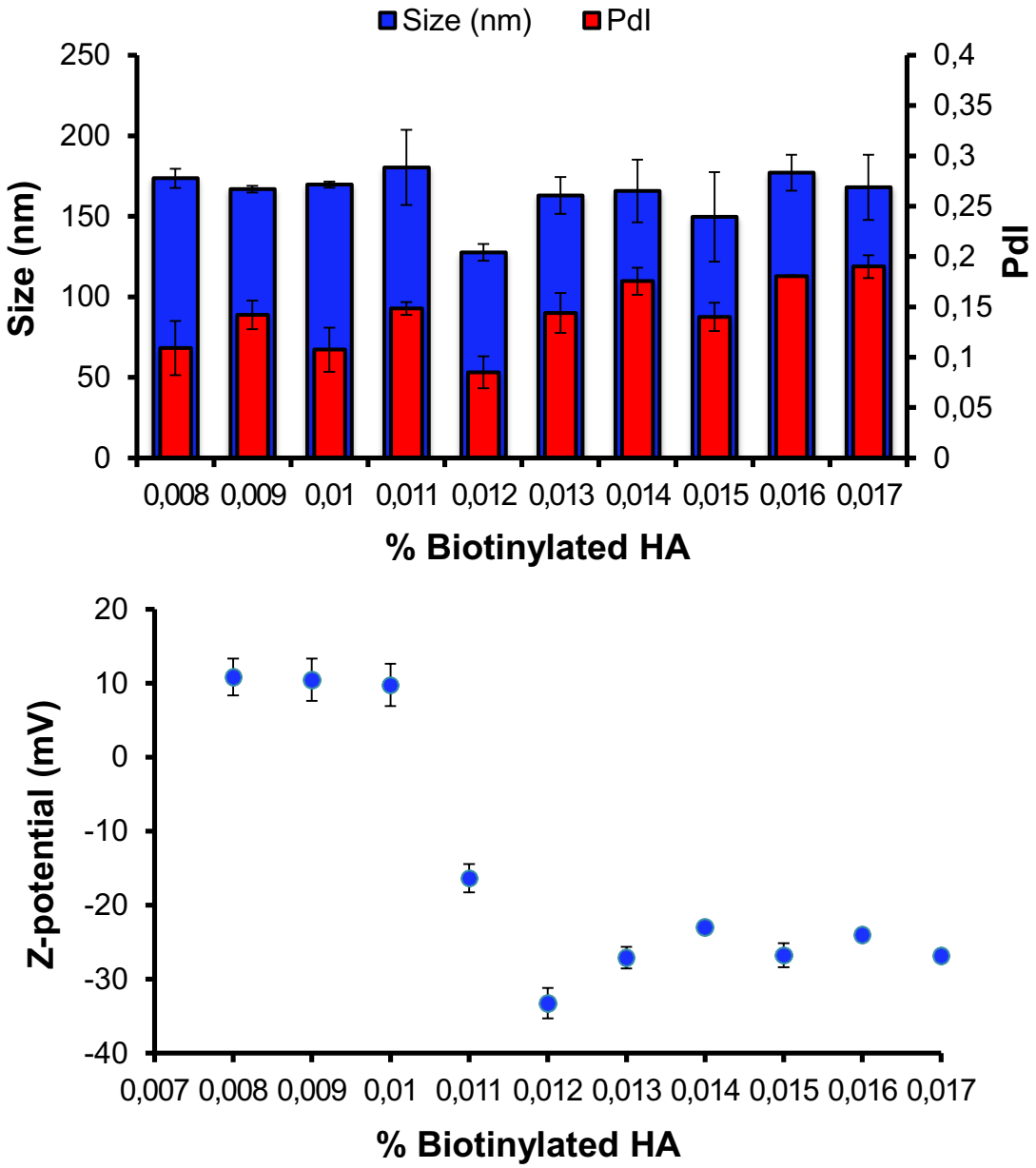

Figure 6: *DLS Size (A) and Z-Potential (B) data of biotinylated HA at different percentage deposited on monolayer L_4 of 1 wt % oil-chitosan 0.01 wt %. Data are reported as mean (n=3) ± SD.*

DLS measurements were done periodically in order to evaluate the dimensional changes, relative to the freshly prepared one. Figure 7 shows that 0.012 wt % HA-biotin-0.005 wt%-CT-0.5% O/W NEs continued to be stable for 45 days, keeping its hydrodynamic diameter below 200 nm. Also the PdI values remained within <0.2 for 40 days, which indicated no relevant aggregation phenomenon or destabilization occurred.

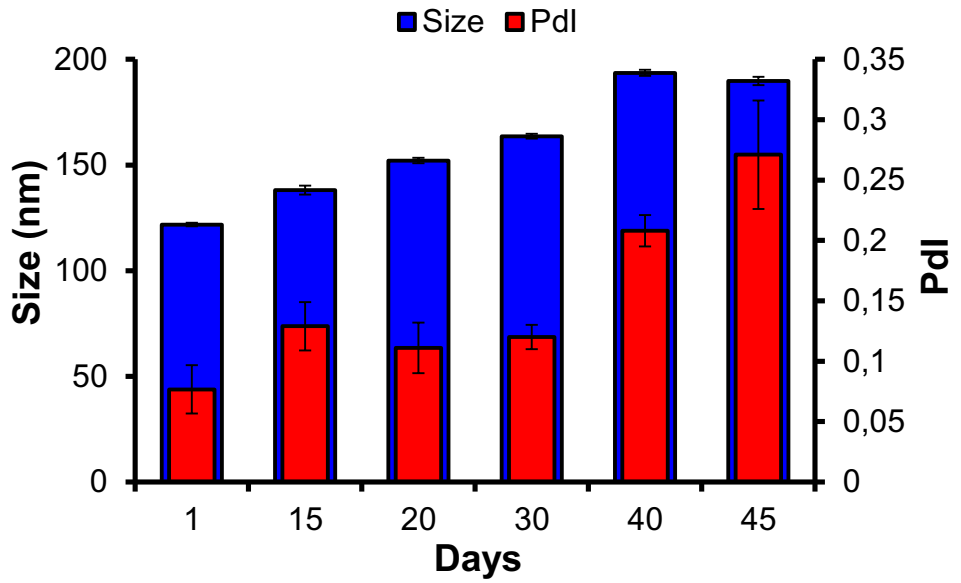

Figure 7: *Dimensional behaviour over time of 0.012 wt% HA-biotin-0.005 wt% CT-0.5% O/W NEs.*

Evaluation of biotin molecules exposed outside NCs by ITC analysis

Biotin–streptavidin interaction represents one of the strongest non-covalent affinities known so far. Streptavidin is a tetramer and each subunit can theoretically bind four molecules of biotin with equal affinity[23]. From the structure of the bounded complex, it is known that the binding energy derives from several types of interactions, mainly hydrophobic and van der Waals ones, between the protein and biotin; but the largest contributions arise from

tryptophan contacts to biotin[24,25].

One of the aims of this PhD project was the development of a multifunctional nanocarrier for drug delivery. The designed strategy consists in the exploitation of the molecular binding affinity between streptavidin and biotin, which has been widely utilized in the development of drug delivery systems. In literature there are many example of streptavidin used as linker between biotinylated nanoparticles and targeting moieties[26,27,28]. Due to in-situ and non-destructive nature, ITC is an excellent technique for the interaction studies between nanoparticles and biomolecules. In order to establish the exact amount of streptavidin able to saturate the biotin groups exposed on the surface of NCs, isothermal titration calorimetric experiments were carried out. A schematic representation of the experiment design is illustrated in Figure 8.

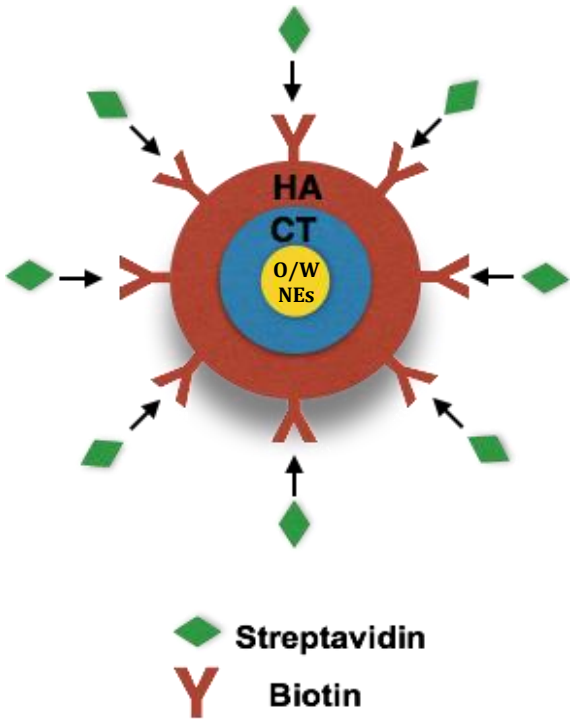

Figure 8: *Schematic representation of ITC experiment*

The technique, which provides a complete thermodynamic characterization of protein-ligand interactions, is based on the measurement of the heat, absorbed or released, when a solution of a molecule, generally referred as macromolecule, inside a cell, is titrated by injections of an interacting molecule (the ligand)[29].

Firstly, a complete thermodynamic analysis of biotin hydrazide-streptavidin binding was performed. A solution of streptavidin 6 μM in PBS 10 mM was titrated by stepwise injections of biotin hydrazide solution 100 μM in PBS 10 mM. Data were analysed with an independent site model, which consists in the simplest cases of binding equilibrium, where the macromolecule has *n* independent and equivalent binding sites for a ligand[30]. In Figure 9 experimental dates obtained subtracting the heat of ligand dilution into the buffer are shown.

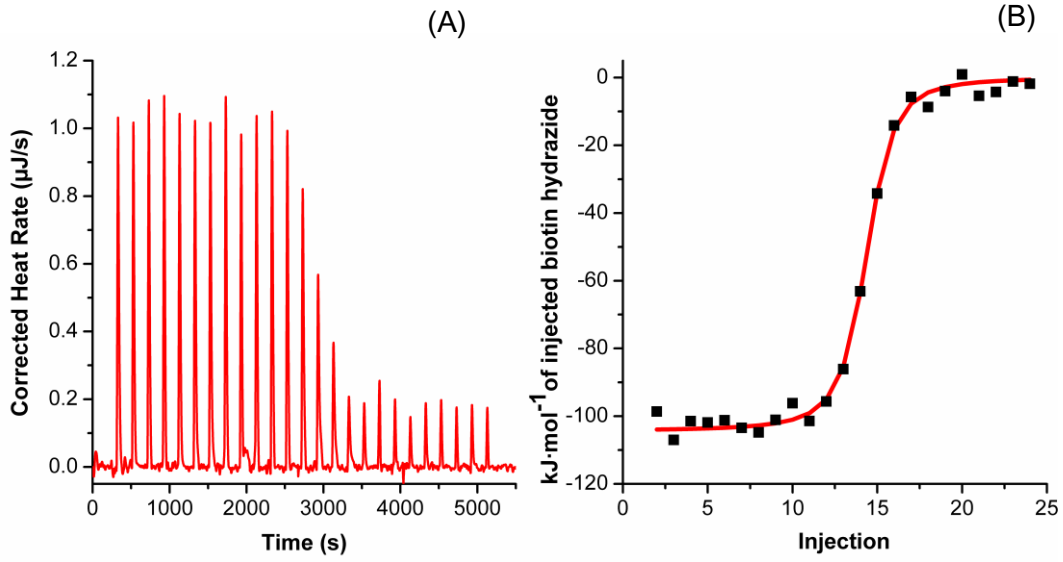

Figure 9: *ITC data for titration by stepwise injection of biotin hydrazide 100 μM in PBS 10 mM, in a solution of streptavidin 6 μM in PBS 10 mM at 25 °C. The solid circles are the experimental data obtained by integrating the raw data and subtracting the heat of ligand dilution into the buffer. The lines represent the best fit obtained with the independent-sites model.*

Table 3: *Thermodynamic parameters of the interactions between biotin hydrazide and streptavidin. The values represent the average deviation of different ITC measurements.*

Model	Variable	Value
Indipendent	K_d (M)	$7.23 \cdot 10^{-8} \pm 8.4 \cdot 10^{-8}$
	n	2.80 ± 0.51
	ΔH (kJ/mol)	−126.60 ± 27.86
	TΔS (kJ/mol)	−84.44 ± 31.96
	ΔG (kJ/mol)	−42.16 ± 4.10
	K_a (M)	$4.27 \cdot 10^{7} \pm 4.96 \cdot 10^{7}$

Thermodynamic parameters are reported in Table 3. The interaction was enthalpy driven (ΔH=−126.60 kJ/mol) with a substantial entropy cost (ΔS=−84.44 kJ/mol) to achieve the net negative free energy change (ΔG=−42.16 kJ/mol). Notwithstanding we used the biotin hydrazide, the affinity with the streptavidin is very high; in fact K_d ($K_d=1/K_a$) values are in the order of nM, in accordance with literature data[25]. These results are also in accordance with the thermodynamic characterization of biotin-streptavidin by ITC analysis reported by Wen-Yih Chen *et al.* (ΔG= −68.6 kJ/mol; ΔH= −133.8 kJ/mol; TΔS= −65.3 kJ/mol; n= 2.5)[31].

Little discrepancies can be probably ascribed to the terminal amine of biotin hydrazide molecules, used in our case, which could affect the binding with the streptavidin. This analysis has been used as reference point to next ones.

To establish the optimum range of concentrations to observe a saturation of biotin by streptavidin injections, we started from the titration of a polymer solution of biotinylated hyaluronic acid, into the cell, with streptavidin in the syringe. The ITC experiment must be done under conditions where the heat change is both measurable for each injection and where the heat change varies for subsequent injections producing a curved thermogram (plot of heat

change *vs* injection number, or molar ratio of ligand/macromolecule)[32]. To achieve that purpose, we investigated a wide range of concentrations obtaining the best curve by titrating biotinylated hyaluronic acid 0.05 wt% with streptavidin 16 μM. The experimental data are shown in Figure 10.

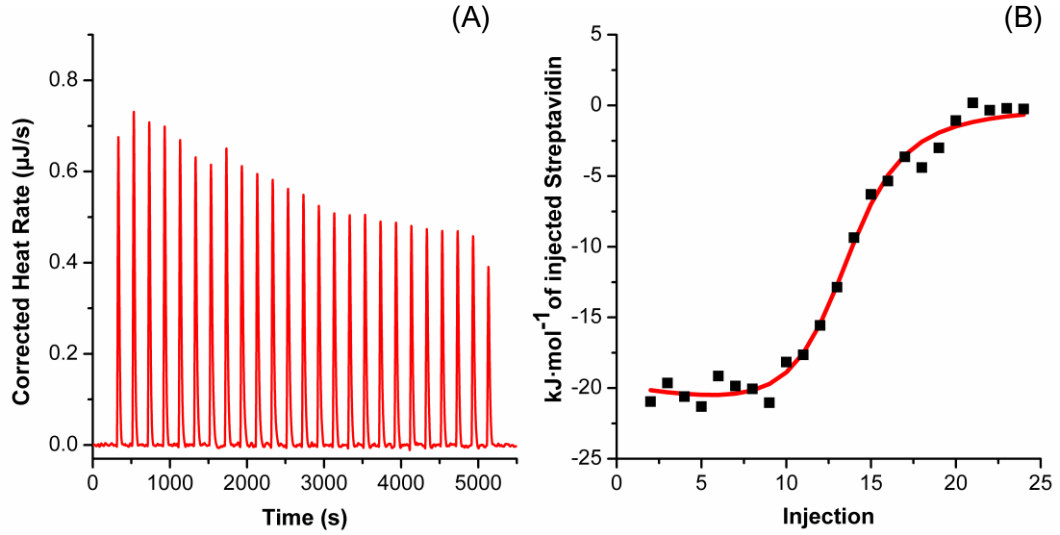

Figure 10: *ITC data for titration by stepwise injection of streptavidin in a solution of HA-biotin 0.05 wt% at 25 °C. The solid circles are the experimental data obtained by integrating the raw data and subtracting the heat of ligand dilution into the buffer. The lines represent the best fit obtained with the independent-sites model.*

Table 4: *Thermodynamic parameters of the interactions between biotinylated hyaluronic acid and streptavidin. The values represent the average deviation of different ITC measurements.*

Model	Variable	Value
Indipendent	K_d (M)	$1.81 \cdot 10^{-7} \pm 1.8 \cdot 10^{-7}$
	*n**	1.78 ± 0.15
	ΔH (kJ/mol)	−231.4 ± 84.15
	TΔS (kJ/mol)	−192.08 ± 87.22
	ΔG (kJ/mol)	−39.32 ± 3.08
	K_a (M)	$1.10 \cdot 10^{7} \pm 1.09 \cdot 10^{7}$

** n value represents the molar ratio between streptavidin and biotinylated HA*

The fitting parameters together with the calculated Gibbs free energy and the entropy gain are given in Table 4. Although the binding process is exothermic (ΔH < 0), there is a considerable unfavourable entropic contribution probably due to the rearrangement of water molecules that play an important role in glycosaminoglycans (i.e HA)[33]. Respect to previous experiment, in this case the high affinity between the biotinylated polymer and streptavidin was kept but the K_a value was slightly decreased ($K_a = 1.10 \cdot 10^7$ M). Because the biotin molecules were covalently linked to the polymer chain, a reduction of their degrees of freedom could be observed.

To confirm that the obtained binding curve was only due to the specific interactions between biotin and the streptavidin, the experiment without biotin was carried out.

In particular, a solution of 0.05 wt% HA dissolved in water was titrated with streptavidin 16 μM (identical previous experimental condition). Raw data in Figure 11 shows only small peaks of dilution, demonstrating that there is no any kind of binding between the streptavidin and the polymer.

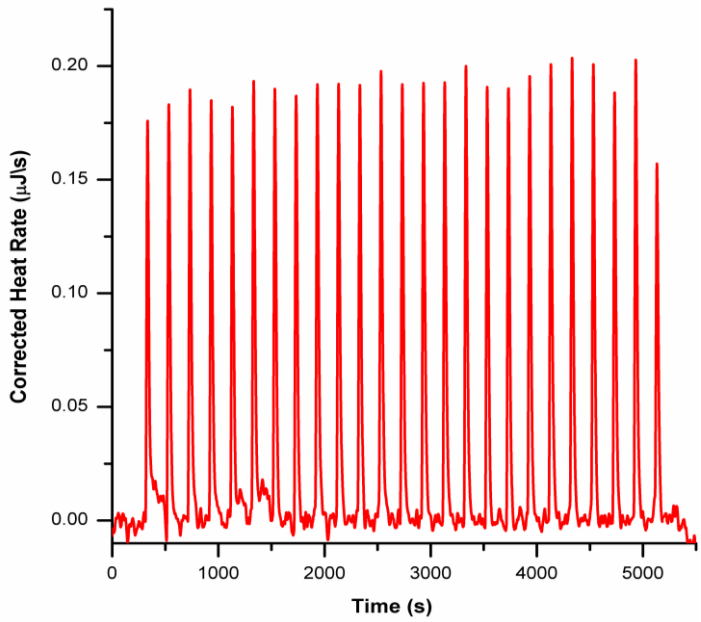

Figure 11: *ITC data for titration by stepwise injection of streptavidin into 0.05 wt% HA at 25 °C.*

On the basis of the previous results, the same experiment design was performed to establish the exact amount of biotin exposed outside the carrier, when the biotinylated polymer was deposited above the chitosan coated O/W NE. A bilayer system at the same concentration of hyaluronic acid of the preceding experiment was assembled. So, in this case, 0.05 wt% HA-biotin-0.02 wt% CT-2.08 wt% O/W NEs was titrated with a solution of streptavidin 16 µM. The ITC binding curve obtained from the integration of the heat data has a good sigmoidal behaviour and it was fitted with an independent and equivalent-sites model (Figure 12).

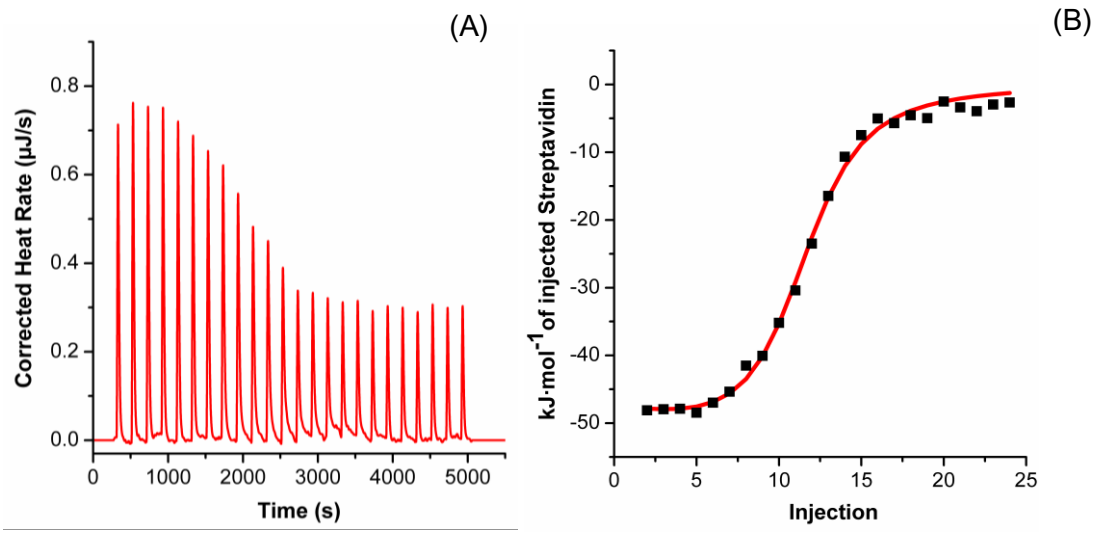

Figure 12: *ITC data for titration by stepwise injection of Streptavidin in 0.05 wt% HA-biotin-0.02 wt% CT-2.08 wt% O/W NEs at 25 °C (A). Normalized heat of interaction between biotinylated O/W NEs and streptavidin. The solid circles are the experimental data obtained by integrating the raw data and subtracting the heat of ligand dilution into the buffer. The lines represent the best fit obtained with the independent-sites model (B).*

Table 5: *Thermodynamic parameters of the interaction between streptavidin and 0.05 wt% HA-biotin-0.02 wt% CT-2.08 wt% O/W NEs at 25 °C.*

Model	Variable	Value
Indipendent	K_d (M)	$8.35 \cdot 10^{-8} \pm 1.53 \cdot 10^{-8}$
	*n**	1.79 ± 0.54
	ΔH (kJ/mol)	−436.85 ± 30.62
	TΔS (kJ/mol)	−396.24 ± 31.20
	ΔG (kJ/mol)	−40.61 ± 0.58
	K_a (M)	$1.22 \cdot 10^{7} \pm 2.21 \cdot 10^{6}$

** n value represents the molar ratio between streptavidin and biotinylated HA*

The thermodynamic signature shows that the process is enthalpically driven counterbalanced by an unfavourable entropic contribution to Gibbs energy,

due to the formation of new interactions between biotin and streptavidin upon binding. The unfavourable entropic contribution can be a consequence of the loss of conformational degrees of freedom for both the interacting molecules. By comparing the two experiments, the value of ΔG is essentially the same, but the enthalpic contribution is significant higher in absolute value (Table 5). This can be ascribable to a reduction of mobility of biotin groups to bind the streptavidin when they are exposed outside the carrier.

According to the NMR data, biotinylated HA has a yield of 37% of biotin covalently linked to carboxylic group on the total amount of HA monomers. This means that for 1 mole of biotinylated HA corresponds ~244 biotin molecules bounded.

Conversely, ITC data shows that the molar ratio (*n* value) between streptavidin and biotinylated HA, both when the polymers was dissolved in the bulk solution and when it was deposited above the chitosan coated O/W NEs, is ~2. This means that two mole of streptavidin interact with each mole of polymer. As result of ITC experiments, the amount of biotin molecules (conjugated to HA) available to bind the streptavidin was 0.7%. A possible explanation derives from the large repertoire of conformations that HA could take. Therefore, many biotin molecules could be hidden inside the network of the polymer chains[34].

Nanocapsules decoration

A decoration strategy was at the basis of the development of NCs within this Phd thesis. ITC results were of fundamental importance to perform NCs assembly and avoid nonspecific interactions due to the addition of a larger amount of the biomolecules than the available sites. A qualitative study of specific interaction of streptavidin to biotinylated NCs was performed by confocal analysis. In accordance with ITC results, streptavidin, labeled with Atto 655, was added under sonication at a ratio 1:1 with the biotin to biotinylated and non-biotinylated O/W NEs. As shown in Figure 13, the fluorescence intensity of the Atto-655-streptavidin was about 86.1% higher for biotinylated system when compared to non-biotinylated one, as consequence of the specific interaction with biotin-HA. No specific fluorescence signals were observed for the samples without biotin moieties. Analyses were performed on at least 3 images for each system.

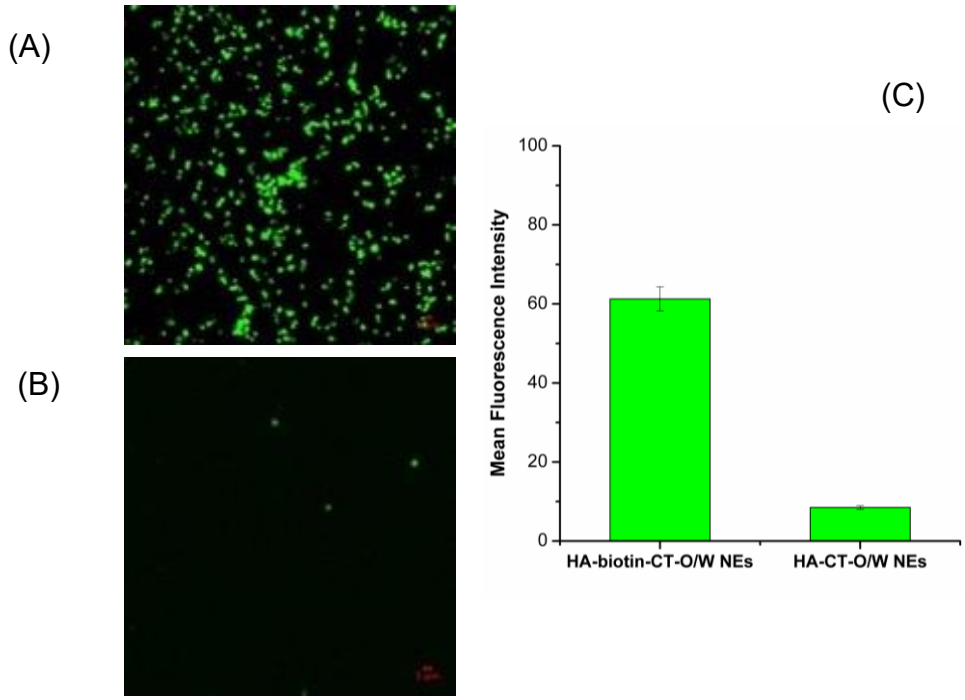

Figure 13: *Confocal images of Atto 655-streptavidin interaction with HA-biotin-CT-O/W NEs (A) and HA-CT-O/W NEs (B) (scale bar is 1 μm). Plot of mean fluorescence intensity of Atto-655 labelled streptavidin(C). Data are reported as mean (n=3) ± SD.*

Streptavidin labeling is also useful as a probe for NCs detection in the cellular environment. To complete the coating of the NCs a layer of PEG was used to improve the shelf life of the NCs from one side and to use it as model for future functionalization from the other side. Firstly, the streptavidin was added to the HA-biotin-CT-O/W NEs as described before. Then a biotin functionalized PEG_{2k} linker (biotin-PEG_{2k}-COOH) was added to the streptavidin-HA-biotin-CT-O/W NEs under sonication, at a ratio 2:1 with the streptavidin. Then, functionalized NCs were characterized by DLS, whose measurements are reported in Table 6. As illustrated, a little increment of size occurred by the addition of each single layer remaining below 150 nm. The proven stability of these systems was confirmed by good dimensional behaviour and a PdI value kept below 0.2, during every step of multi-component construction. The Z-

potential values were either highly negative (< -30) or positive (> +30), as such they will tend to repel each other by large force and there will be low probability for the formation of aggregates.

Table 6: *Size, PdI and Z-potential measurement of each NCs component during the several steps of assembly. Data are reported as mean (n=3) ± SD.*

	Size (nm)	PdI	Z-potential (mV)
O/W NEs	97.13 ± 4.30	0.092 ± 0.003	-31.1 ± 1.6
CT-O/W NEs	107.47 ± 11.40	0.060 ± 0.045	+25.4 ± 1.7
HA-biotin-CT-O/W NEs	121.83 ± 3.50	0.099 ± 0.008	-34.2 ± 2.2
Streptavidin-HA-biotin-CT-O/W NEs	126.80 ± 0.28	0.147 ± 0.024	-34.0 ± 1.8
PEG_{647}-Streptavidin-HA-biotin-CT-O/W NEs	127.75 ± 1.20	0.148 ± 0.019	-28.9 ± 1.1

In order to achieve a qualitative visualization of the NCs just developed by confocal microscopy, the carboxyl terminal end of biotin-PEG_{2k} –COOH was conjugated with Atto 647N amine thanks to amide bond formation between them. Figure 14 shows confocal image of PEG_{647}-streptavidin-HA-biotin-CT-O/W NEs.

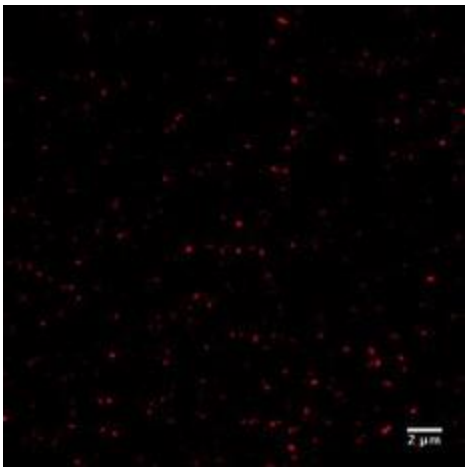

Figure 14: *Confocal image of Atto647-PEG-streptavidin-HA-biotin-CT-O/W NEs. Scale bar is 2 µm.*

Conclusions

In this work, we showed the preparation of a novel drug delivery system based on layer-by-layer polymers deposition above O/W NEs made of completely biocompatible and biodegradable materials. Firstly, we introduced biotin moieties on the polymers (HA), opportunely characterized, which constitute the external layer of O/W NEs. The size scalability of of these systems was demonstrated. A complete thermodynamic characterization of streptavidin-NCs interaction was performed by ITC analysis to evaluate the right amount of each component to be added following a step by step procedure. The strong affinity between streptavidin and biotin allowed us to expose any kind of ligands outside the NCs for several applications in the field of cancer diagnostics and therapy. As example, we functionalized our systems with a PEG linker as model for any molecules, antibody or peptides that could be attached for future prospective.

Materials and methods

Materials

Soybean oil and surfactant Lipoid E80 (egg lecithin powder 80-85% enriched with phosphatidylcholine and 7–9.5% content in phosphatidylethanolamine) were purchased from Lipoid GmbH and used without further purification. For preparation of all nanoemulsions and solutions, Millipore Milli-Q water was used. Chitosan (CT, LMW 90-150 kDa, DDA 84% determined via 1H-NMR). 1-Ethyl-3-(3-dimethylaminopropyl)carbodiimide (EDC), N-Hydroxysuccinimide (NHS), biotin hydrazide, dimethyl sulfoxide (DMSO), deuterium oxide (D_2O), Atto 655-streptavidin and Midi Pur-A-Lyzer tubes (1 kDa) were purchased from Sigma Aldrich. Hyaluronic acid 250 kDa and biotin-PEG_{2k}-COOH were purchased from Creative PEGWorks. Atto 647N wasp purchased from ATTO-TEC GmbH. PBS tablets (1x) was purchased from MP Biomedicals. Dialysis membranes were purchased from Spectrum Laboratories Inc.

Preparation of biotinylated hyaluronic acid

The biotin-hyaluronic acid (HA-Biotin) conjugate was prepared as follows: 0.52 mmol of NHS and 0.52 mmol of EDC were added to a 1% (w/v) solution of HA (10 mL solution, 0.26 mmol HA monomer) in water, pH 6.0, under stirring at room temperature for 60 min to facilitate a homogeneous dispersion of reagents in the reaction solution. Then an amount of 0.052 mmol of biotin hydrazide, dissolved in DMSO, was added to the reaction mixture, overnight. The resulting polymer was dialyzed against Milli-Q water using a 12-14 kDa dialysis membrane. The water was changed twice a day for 3 days, and then the polymer was lyophilized[18].

Nuclear magnetic resonance spectroscopy (NMR)

HA-Biotin was characterized by Nuclear Magnetic Resonance (NMR). NMR spectra were recorded using an Agilent 600 MHz (14 T) spectrometer equipped with a DD2 console and a One NMR HX probe. HA-biotin (1 mg) was dissolved in 600 μL of 90/10 H_2O/D_2O solution.

1H 1D spectra were recorded at 300 K using 1024 scans to obtain a good signal-to-noise ratio. Water signal was reduced using a PRESAT pulse sequence. Spectra were transformed and analyzed using VNMRJ 4.0 software.

Oil in water nanoemulsion

Firstly, a 20-wt % oil in water pre-emulsion was prepared. 5.8 g of Lipoid E 80 (egg lecithin powder 80-85% enriched with phosphatidyl choline and 7-9.5% content in phosphatidyl ethanolamine) were dissolved in 24 mL of soybean oil (density at 20 °C of 0.922 $g \cdot mL^{-1}$) at 60 °C using the immersion sonicator (Ultrasonic Processor VCX500 Sonic and Materials), performing runs of 10 seconds for 1 minute at 10% of sonication amplitude (microtip screwed). Then, the oil phase was added to the aqueous phase (Milli-Q water), and mixed using the immersion sonicator with runs of 10 seconds for 8 minutes at 70% of amplitude (a pulse-on and a pulse-off respectively of 10 seconds). The pre-emulsion was finally homogenized for 3 single cycles and 200 steps at a pressure of 2000 bar by a high-pressure homogenizer (110P series microfluidizer) to obtain the final nanoemulsion.

Polymers deposition above oil in water nanoemulsion

Firstly, it was deposited a layer of chitosan around the oil template with a final concentrations of oil and chitosan of 10 wt% and 0.1 wt%, respectively. 0.1 M acetic acid solution of chitosan (0.125 wt%) was prepared with a final pH=4. Nanoemulsion 20 wt% oil was added quickly to the chitosan solution under

vigorous stirring and kept under stirring for 15 minutes to allow uniform chitosan deposition. The nanoemulsion with the first positive layer of chitosan was passed through a high-pressure valve homogenizer at 700 bars for 100 continuous steps. The next hyaluronic acid layer was prepared by aid of two syringe pumps (HARVARD APPARATUS 11 PLUS) and an ultrasonic bath (FALC INSTRUMENTS). Starting from the secondary nanoemulsion 10 wt% oil - 0.1 wt% CT, a negative charged polymer layer was deposited by mixing 1:1 (v:v) of a 0.24 wt% aqueous solution of biotinylated hyaluronic acid , with the secondary nanoemulsion suspension. The two liquid phases were injected at the same flow rate (0.4 mL min^{-1}) through two polymicro flexible fused silica micrometric capillaries (inner diameter of 200 μm) interfaced at their extremities (Molex). Each drop was then collected inside a glass tube immersed in the ultrasonic bath at room temperature, 59 kHz and 100% power for 15 minutes.

Nanocarrier assembly

The streptavidin solution was prepared by dissolving 1 mg in 1 ml of Milli-Q water (16,6 μM). The streptavidin solution was added to the HA-Biotin 0.12 wt%-CT 0.05 wt%-O/W NEs 5 wt% oil, under sonication for 15 minutes and T= 20 °C, at a final concentration of 5.69 μM. In the same way the biotin-PEG_{2k}-COOH was added under sonication for 15 minutes and T= 20 °C to the streptavidin-HA-Biotin-CT-O/W NEs at a molar ratio 2:1 between biotin-PEG_{2k}-COOH and the streptavidin. The final concentrations were 3.2 μM and 6.4 μM for streptavidin and biotin-PEG_{2k}-COOH respectively, while the final oil weight percentage was 2.78 wt%. The NCs were characterized at each step of preparation measuring the size and Z-potential by dynamic light scattering as described previously.

Coupling of Atto 647N to biotin-PEG2k-COOH

The biotin-PEG_{2k}-Atto 647N conjugate was prepared as follows 2 equivalents (eq.) of NHS and EDC were added to biotin-PEG_{2k}-COOH in water under stirring at room temperature for 20 min to facilitate a homogeneous dispersion of reagents in the reaction solution. Then 50 eq. of Atto 647N dissolved in the minimum volume of DMSO, was added dropwise to the reaction mixture, for five hours. The resulting product was dialyzed against Milli-Q water using Midi Pur-A-Lyzer tube 1 kDa. The water was changed twice a day for 3 days, and then the polymer was lyophilized.

Particle size and Z-potential measurements

All nanoemulsion and their successive functionalization were characterized at each step of preparation by measuring size and polydispersity index (PdI), using Zetasizer Nano ZS device (Malvern Instruments) with a 4 mW He-Ne ion laser at the wavelength of 633 nm and a photodiode detector at an angle of 173°. All the samples were diluted to a droplet concentration of 0.025 wt% by using acetic acid 20 mM at pH 4 for monolayer, and Milli-Q water for emulsions and bilayer suspensions. The calculation of the particle size distribution was performed using a default refractive index ratio (1.59) and 5 runs for each measurement (1 run lasting 100 s), at least 3 times for each sample. A particle electrophoresis instrument (Zetasizer zs nano series ZEN 3600, Malvern Instruments Ltd., Malvern, U.K.) was used for the Z-potential determinations. Samples were diluted as for the particle size analysis. Setting 50 runs for each measurement carried out the Z-potential analysis. Samples were collected into polystyrene cuvettes and measured three times and the results presented are the averages of these measurements. Experiments were carried out at 25 °C. Zetasizer software (Malvern Instruments) was used to

obtain the data. Cumulant analysis was used to give the Z-average value, hydrodynamic diameter, polydispersity index and the intensity size distribution graphs.

Isothermal titration calorimetry analysis

Isothermal titration calorimetry (ITC) experiments were performed using a Nano ITC Low Volume from TA Instruments (USA) with a cell volume of 170 µl. Titration experiments were carried out at 25 °C. In the case of biotin hydrazide-streptavidin titration, the sample cell was filled with a solution of streptavidin 6 µM in PBS 10 mM, and the reference cell was filled with Milli-Q water for all the experiments. 25 injections of 2 µl each of biotin hydrazide 100 µM in PBS 10 mM were added to streptavidin solution every 200 seconds at a continuous stirring rate of 200 rpm. The interaction heat for each injection was calculated after correction for the heat coming from biotin hydrazide dilution that acts as blank. In the case of streptavidin-HA-biotin titration, the sample cell was filled with a solution of 0.05 wt% HA-biotin. It was titrated by 25 injections of 2 µL each of a solution of streptavidin 16 µM. For streptavidin-(HA-biotin-CT-O/W NEs) titration, the sample cell was filled with the 0.05wt%-HA-biotin-0.02wt%-CT-2.08wt%-O/W NEs solution, and the reference cell was filled with Milli-Q water. 25 injections of 2 µl each of a solution of streptavidin 16 µM were added to the sample cell, every 200 seconds at a continuous stirring rate of 200 rpm. Control experiments were performed between the solution of streptavidin 16 µM and the HA 0.05 wt% solution. The interaction heat for each injection was calculated after correction for the heat coming from streptavidin dilution that acts as blank. The binding constant (Ka), enthalpy change (ΔH°), and stoichiometry (n=binding sites) of the interaction process were obtained by fitting the

binding isotherm to the equivalent and independent binding sites model, by using the NanoAnalyze software, version 2.4.1 (TA Instruments). The remaining thermodynamic parameters of the interaction were calculated using the relationships:

$$\Delta G° = - RT \ln K_a$$

$$\Delta G° = \Delta H° - T\Delta S°$$

Confocal microscopy analysis

The study of specific interaction of streptavidin to biotinylated NCs was performed by confocal analysis. Atto 655-Streptavidin was added to biotinylated and non-biotinylated O/W NEs in molar ratio 1:1 respect to biotin. The sample was arranged as described before. It was diluted 1:10 in water Milli-Q and then added (15 µL) to agarose gel at 40° (low gelling temperature agarose A9414 Sigma-Aldrich; 2.5 % w/v, 30 µL) at a volume ratio 1/2 v/v. The sample was placed on a microscope cover glass for 5 minutes to allow the gelation of the agarose. Images of the sample were captured with a ZEISS LSM 700 Laser Confocal Scanning microscope. Images were acquired with a field of view 33.9 x 33.9 µm, 512 x 512 pixel frame format, for a pixel size of 76 x 76 nm. Images were visualized and analysed by Image-J software.

Cryo-TEM characterization

For the preparation of the frozen-hydrated sample the plunge freezing method was performed. Briefly a drop of 3 µL of the samples were put on a previously glow-discharged 200 mesh holey carbon grids (Ted Pella, USA) after that the grid was inserted in the chamber of a FEI Vitrobot Mark IV (FEI company, the Netherlands) at 4°C and 90% of humidity. The droplet of sample was blotted

with filter paper for 1 s, (blot force 1, drain time 0,5 s) and then the grid was plunged into the liquid propane. The grid was then stored in liquid nitrogen in a grid box until it was finally transferred to a cryo-specimen 626 holder (Gatan, Inc., USA) and loaded into the cryo-transmission electron microscope for imaging. To obtain the image of the nanoparticles we used a Tecnai G2 20, a cryo-tomo transmission electron microscope (FEI company, the Netherland) equipped with LaB6 emitter (acceleration voltage of 200 kV) and recorded at with a 2 k × 2 k CCD-Eagle 2HS camera. The Frozen-hydrated sample is radiation-sensitive material so to avoid damaging; the observation was carried out in Low Dose Mode.

References

1. Steichen, S. D., Caldorera-Moore, M. & Peppas, N. A. A review of current nanoparticle and targeting moieties for the delivery of cancer therapeutics. *Eur. J. Pharm. Sci.* **48**, 416–427 (2013).

2. Markman, J. L., Rekechenetskiy, A., Holler, E. & Ljubimova, J. Y. Nanomedicine therapeutic approaches to overcome cancer drug resistance. *Adv. Drug Deliv. Rev.* **65**, 1866–1879 (2013).

3. Shi, J., Kantoff, P. W., Wooster, R. & Farokhzad, O. C. Cancer nanomedicine : progress , challenges and opportunities. *Nat. Publ. Gr.* **17**, 20–37 (2016).

4. Petkar, K. C., Chavhan, S. S., Agatonovik-Kustrin, S. & Sawant, K. K. Nanostructured Materials in Drug and Gene Delivery: A Review of the State of the Art. *Crit. Rev. Ther. Drug Carr. Syst.* **28**, 101–164 (2011).

5. Koo, O. M., Rubinstein, I. & Onyuksel, H. Role of nanotechnology in targeted drug delivery and imaging: a concise review. *Nanomedicine: Nanotechnology, Biology, and Medicine* **1**, 193–212 (2005).

6. Ganta, S., Talekar, M., Singh, A., Coleman, T. P. & Amiji, M. M. Nanoemulsions in Translational Research—Opportunities and Challenges in Targeted Cancer Therapy. *AAPS PharmSciTech* **15**, 694–708 (2014).

7. Capek, I. Degradation of kinetically-stable o/w emulsions. *Adv. Colloid Interface Sci.* **107**, 125–155 (2004).

8. Johnston, A. P. R., Cortez, C., Angelatos, A. S. & Caruso, F. Layer-by-layer engineered capsules and their applications. *Current Opinion in Colloid and Interface Science* **11**, 203–209 (2006).

9. Vecchione, R. *et al.* Ultrastable Liquid–Liquid Interface as Viable Route for Controlled Deposition of Biodegradable Polymer Nanocapsules. *Small* **12**, 3005–3013 (2016).

10. Kabary, D. M., Helmy, M. W., Elkhodairy, K. A., Fang, J. Y. & Elzoghby, A. O. Hyaluronate/lactoferrin layer-by-layer-coated lipid nanocarriers for targeted co-delivery of rapamycin and berberine to lung carcinoma. *Colloids Surfaces B Biointerfaces* **169**, 183–194 (2018).

11. Hörmann, K. & Zimmer, A. Drug delivery and drug targeting with parenteral lipid nanoemulsions - A review. *Journal of Controlled Release* **223**, 85–98 (2016).

12. Fotticchia, T. *et al.* Enhanced Drug Delivery into Cell Cytosol via Glycoprotein H-Derived Peptide Conjugated Nanoemulsions. *ACS Nano* **11**, 9802–9813 (2017).

13. Sakahara, H. & Saga, T. Avidin-biotin system for delivery of diagnostic agents. *Advanced Drug Delivery Reviews* **37**, 89–101 (1999).

14. Skerra, A. & Schmidt, T. G. M. Use of the Strep-tag and streptavidin for detection and purification of recombinant proteins. *Methods Enzymol.* **326**, 271–304 (2000).

15. Vecchione, R. *et al.* Tunable stability of monodisperse secondary O/W nano-emulsions. *Nanoscale* **6**, 9300–9307 (2014).

16. Necas, J., Bartosikova, L., Brauner, P. & Kolar, J. *Hyaluronic acid (hyaluronan): a review*. *Veterinarni Medicina* **53**, (2008).

17. Liu, X. *et al.* Grafting hyaluronic acid onto gold surface to achieve low protein fouling in surface plasmon resonance biosensors. *ACS Appl. Mater. Interfaces* **6**, 13034–13042 (2014).

18. Polyak, B., Geresh, S. & Marks, R. S. Synthesis and characterization of a biotin-alginate conjugate and its application in a biosensor construction. *Biomacromolecules* **5**, 389–396 (2004).

19. Pouyani, T. & Prestwich, G. D. Biotinylated Hyaluronic Acid: A New Tool for Probing Hyaluronate-Receptor Interactions. *Bioconjug. Chem.* **5**, 370–372 (1994).

20. Gatej, I., Popa, M. & Rinaudo, M. Role of the pH on Hyaluronan Behavior in Aqueous Solution. (2005).

21. Vecchione, R. *et al.* Tunable stability of monodisperse secondary O/W nano-emulsions. *Nanoscale* **6**, 9300 (2014).

22. Mun, S., Decker, E. A. & McClements, D. J. Effect of molecular weight and degree of deacetylation of chitosan on the formation of oil-in-water emulsions stabilized by surfactant-chitosan membranes. *J. Colloid Interface Sci.* **296**, 581–590 (2006).

23. Chaiet, L. & Wolf, F. J. The properties of streptavidin, a biotin-binding protein produced by Streptomycetes. *Arch. Biochem. Biophys.* **106**, 1–5 (1964).

24. and, J. D. & Houk*, K. N. The Origins of Femtomolar Protein–Ligand Binding: Hydrogen-Bond Cooperativity and Desolvation Energetics in the Biotin–(Strept)Avidin Binding Site. (2007).

25. Hyre, D. E. *et al.* Cooperative hydrogen bond interactions in the streptavidin-biotin system. *Protein Sci.* **15**, 459–467 (2006).

26. Dundas, C. M., Demonte, D. & Park, S. Streptavidin–biotin technology: improvements and innovations in chemical and biological applications. *Appl. Microbiol. Biotechnol.* **97**, 9343–9353 (2013).

27. Shibu, E. S. *et al.* Singlet-Oxygen-Sensitizing Near-Infrared-Fluorescent Multimodal Nanoparticles. *Angew. Chemie Int. Ed.* **52**, 10559–10563 (2013).

28. Chai, Z. *et al.* A facile approach to functionalizing cell membrane-coated nanoparticles with neurotoxin-derived peptide for brain-targeted drug delivery. *J. Control. Release* **264**, 102–111 (2017).

29. Martinez, J. C. *et al.* Isothermal Titration Calorimetry: Thermodynamic Analysis of the Binding Thermograms of Molecular Recognition Events by Using Equilibrium Models. (2013).

30. C., J. *et al.* Isothermal Titration Calorimetry: Thermodynamic Analysis of the Binding Thermograms of Molecular Recognition Events by Using Equilibrium Models. in *Applications of Calorimetry in a Wide Context - Differential Scanning Calorimetry, Isothermal Titration Calorimetry and Microcalorimetry* (InTech, 2013).

31. Kuo, T.-C., Tsai, C.-W., Lee, P.-C. & Chen, W.-Y. Revisiting the streptavidin-biotin binding by using an aptamer and displacement isothermal calorimetry titration. *J. Mol. Recognit.* **28**, 125–128 (2015).

32. Freyer, M. W. & Lewis, E. A. Isothermal Titration Calorimetry: Experimental Design, Data Analysis, and Probing Macromolecule/Ligand Binding and Kinetic Interactions. *Methods Cell Biol.* **84**, 79–113 (2008).

33. Santos, H. A., Manzanares, J. A., Murtomäki, L. & Kontturi, K. Thermodynamic analysis of binding between drugs and glycosaminoglycans by isothermal titration calorimetry and

fluorescence spectroscopy. *Eur. J. Pharm. Sci.* **32**, 105–114 (2007).

34. Fotticchia, I. *et al.* Energetics of ligand-receptor binding affinity on endothelial cells: An in vitro model. *Colloids Surfaces B Biointerfaces* **144**, 250–256 (2016).

35. Kuehl, C. *et al.* Hyaluronic Acid Molecular Weight Determines Lung Clearance and Biodistribution after Instillation HHS Public Access Graphical Abstract. *Mol Pharm* **13**, 1904–1914 (2016).

36. Takahashi, R., Kubota, K., Kawada, M. & Okamoto, A. Effect of molecular weight distribution on the solution properties of sodium hyaluronate in 0.2M NaCl solution. *Biopolymers* **50**, 87–98 (1999).

37. Perrault, S. D. & Chan, W. C. W. In vivo assembly of nanoparticle components to improve targeted cancer imaging.

CHAPTER 3: Peptide functionalization of emulsion-based nanocarrier towards cancer cells overexpressing CD44 receptor

Introduction

During the last decades, the introduction of tumour-targeted therapies has significantly changed the medical treatments of several types of cancer, improving their therapeutic index[1,2]. A significant obstacle that needs to be overcome is the lack of site-specific accumulation of anticancer drugs in tumor sites, which results in severe side effects due to an increased exposure of normal tissues to the drugs[3,4]. It is well known that cancer cells and more in general the tumor microenvironment express different molecular targets (antigens and/or receptors) respect to normal cells and tissues. By their targeting, a possible strategy largely used to enhance the accumulation of drug delivery system (DDS) to cancer cells was their decoration with ligands specific for receptors. In the last years, increasing efforts have been made on the functionalization of DDS with a variety of tumor-targeting ligands, such as antibody fragments, protein, endogenous molecules, peptides and so on, due to their powerful advantage in targeting drugs to the tumor sites *via* active mechanisms. The National Cancer Institute defines the molecular targets that we are dealing, also known as biomarkers, as a biological molecules found in the blood, body fluids or tissues representing an indication of a normal or abnormal process, or of a condition or disease[5]. One of the well-established tumour biomarkers is the cluster of differentiation 44 (CD44). It is a cell

membrane glycoprotein involved in several cell–cell interactions, cell adhesion, and cell migration. CD44 receptor binds to many extra-cellular matrix (ECM) ligands, but the principal one is the hyaluronic acid (HA)[6,7]. It is expressed in many types of cell, while its isoforms CD44v3 and CD44v6 are upregulated in many invasive cancer cells (including breast, colon, prostate, and lung cancer) and cancer stem cells and promotes metastasis by enhancing cell migration and invasion [8,9]. As result of several synthetic peptides screening, encompassing the laminin α5 chain (G-domain), it was found a particular sequence (CD44 binding peptide, CD44BP) that binds specifically to the glycosaminoglycan (GAG) side chains of CD44v3 and CD44v6 and inhibits tumor cell migration, invasion and angiogenesis *via* blocking fibroblast growth factor 2 (FGF2) binding to the GAG side chains of CD44 [10,11,12]. It was reported that, *in vivo*, CD44BP inhibited primary B16-F10 tumor growth (melanoma), angiogenesis, lung colonization, and tumor progression[11], while, when encapsulated in a gel culture system with cancer cells, it abolished breast cancer tumorsphere formation *in vitro* and *in vivo*[13]. Ayelet David and his group have recently designed a new copolymer, firstly conjugated only with CD44BP and then integrated with an antimitotic drug (paclitaxel, PTX), which inhibited the rate of tumor growth *in vivo* at the same extent for both cases[14]. As outcome of these studies, CD44BP has proven to be a promising candidate for tumor targeting. In order to develop a novel emulsion based nanocapsules (NCs) for active targeting, CD44BP was integrated to the multilayer polymer coated O/W NE described in the previous chapter. Firstly, we stabilized O/W NEs with a double layer of chitosan and biotinylated hyaluronic acid to protect the cargo and implement functions in terms of targeting as well as detection. Then, it was rendered smarter by its functionalization with a bioactive peptide that can promote highly specific active targeting toward different types of cancers, thanks to ligand-receptor recognition. The system was based on the

development of an easy additive decoration strategy that exploits biotin–streptavidin physical interaction. The peptide was conjugated to a biotinylated poly(ethylene glycol) (PEG) chain in order to inhibit the nanocarrier clearance by eluding the mononuclear phagocyte system (MPS) and improve the accumulation of the entire system to the tumor site by means of peptide action. A schematic representation of functionalized nanocapsules is reported in Figure 1. In order to assess the peptide specificity toward tumor cells over-expressing CD44 receptor, biological tests of peptide functionalized O/W NEs were carried out. We chose human primary glioblastoma cell line (U87) as model of tumors that over-express CD44 receptor[15] and curcumin, a natural bioactive compound isolated from the Curcuma longa plant, as anticancer agent[16].

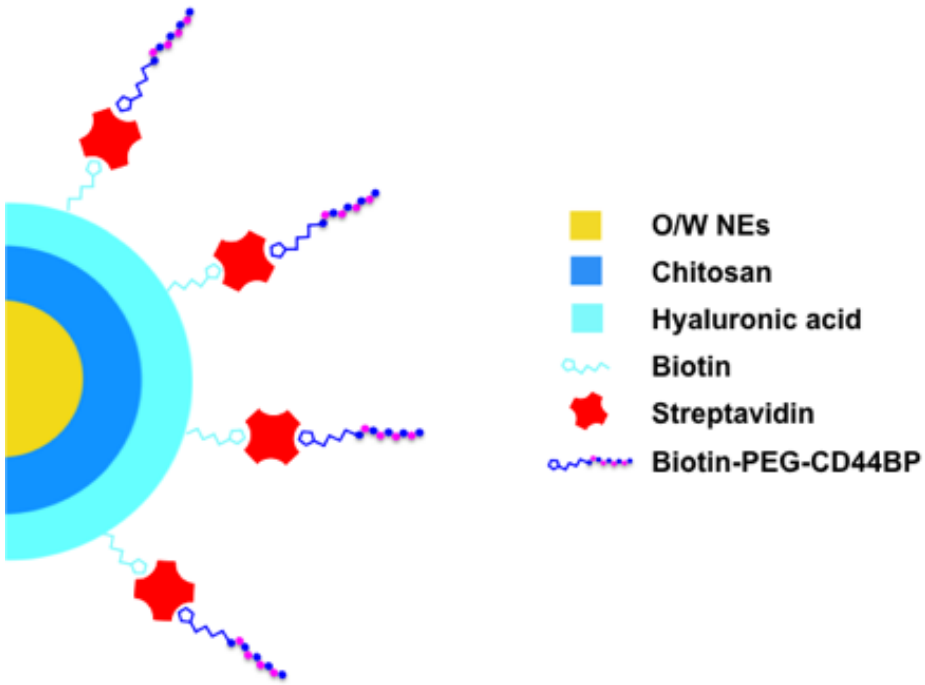

Figure 1: *Schematic representation of peptide functionalized O/W NEs.*

Results and discussion

Synthesis, purification and characterization of CD44BP

Based on literature data discussed in Chapter 1, the focus of this PhD project has been the functionalization of O/W NEs with a peptide for active targeting. In particular it was identified a 13-mer peptide that recognize CD44 receptor. The amino acid sequence was: RLVSYNGIIFFLK. A coupling with 5-carboxyfluorescein (5-FAM) was performed to label the peptide at the N-term (5-FAM-CD44BP). Another non-α-amino acid (β-alanine) was introduced at the N-tem before the coupling reaction with 5-FAM to avoid an Edman-type elimination reaction[17]. The peptide synthesis was performed exploiting the solid-phase peptide strategy (SPPS), using 9-fluorenylmethoxycarbonyl (Fmoc) chemistry and a super acid labile resin. 5-FAM-CD44BP was synthetized and the resulting peptide was deprotected and cleaved from the resin. The crude peptide purity was assessed by analytical RP-HPLC, using a C-18 column with a linear elution gradient. The HPLC chromatograms of the crude and purified peptide chain are reported in Figure 2. Unambiguous identification of the product at R_t = 27.44 min was accomplished through ESI-MS analysis whose mass spectrum is reported in Figure 3.

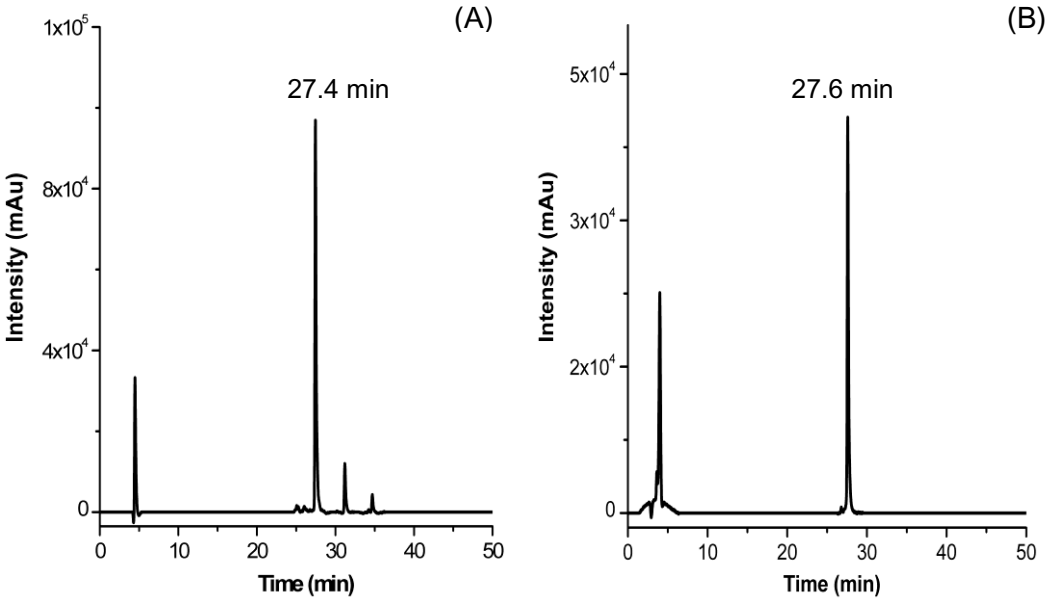

Figure 2: *Analytical RP-HPLC of 5-FAM-CD44BP crude peptide (A) and purified one (B). The chromatogram were detected at λ = 220 nm.*

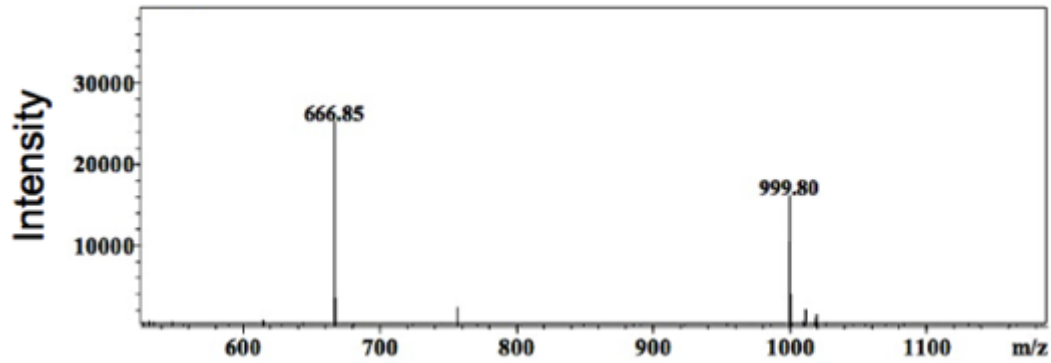

Figure 3: *ESI-MS of the peak at R_t = 27.44 min. The two masses at m/z 666.85 and 999.80 represent respectively $[M+3H]^{3+}$ and $[M+2H]^{2+}$ of theoretical expected mass 1997.01 Da.*

The HPLC peak with R_t = 27.44 min was correlated to a mass peak of *m/z* 666.85 ($[M+3H]^{3+}$) and *m/z* 999.80 ($[M+2H]^{2+}$) which were consistent with the theoretical expected mass of 1997.01 Da of the peptide (calculated mass: 1997.55 ± 0.5 Da).

Once the synthesis was completed, a small amount of product was analyzed by TANDEM mass spectrometry coupled to liquid chromatography. A single peak, corresponding to the desired peptide, was found and its product ions scan showed the expected fragmentations (Figure 4 and Table 1).

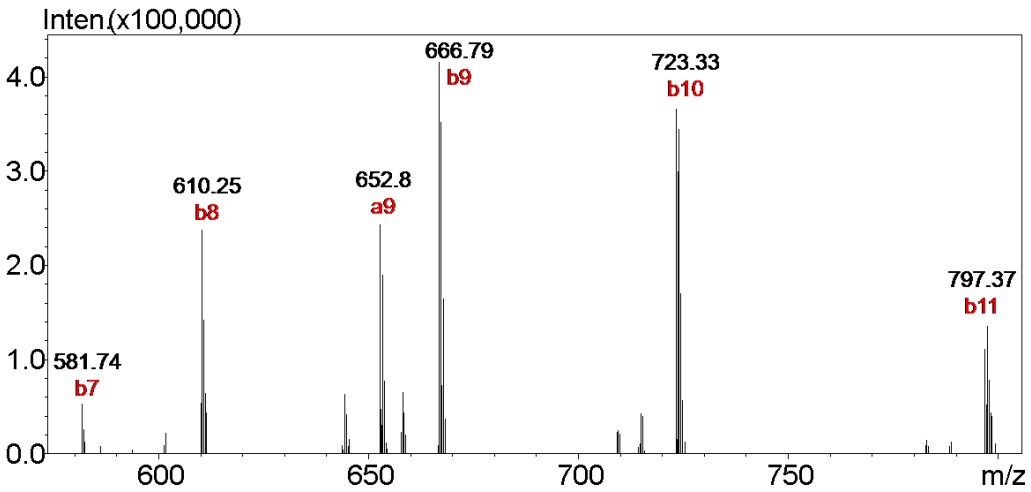

Figure 4: *ESI-MS-MS fragmentation spectra of 5-FAM-CD44BP.*

Table 1: *Mass table of 5-FAM-CD44BP fragmentations. Ciano numbers represent the theoretical fragments founded in the experimental spectrum.*

#	b	b++	b+++	c	Sequence	y	y++	y+++	#
1					5FAM-βAla	1997.01	999.01	666.34	14
2	585.19			602.21	Arg	1568.93	784.97	523.65	13
3	698.27			715.30	Leu	1412.83	706.92	471.62	12
4	797.34	399.17	266.45	814.36	Val	1299.74	650.38	433.92	11
5	884.37	442.69	295.46	901.4	Ser	1200.68	600.84	400.89	10
6	998.41	499.71	333.48	1015.44	Asn	1113.64	557.33	371.89	9
7	1161.48	581.24	387.83	1178.5	Tyr	999.60	500.30	333.87	8
8	1218.49	609.75	406.84	1235.52	Gly	836.54	418.77	279.52	7
9	1331.58	666.29	444.53	1348.61	Ile	779.52	390.26	260.51	6
10	1444.67	722.84	482.23	1461.69	Ile	666.43			5
11	1591.73	796.37	531.25	1608.76	Phe	553.35			4
12	1738.80	869.91	580.27	1755.83	Phe	406.28			3
13	1851.89	926.45	617.97	1868.91	Leu	259.21			2
14					Lys	146.13			1

Further, 5-FAM-CD44BP was purified by preparative RP-HPLC (Figure 5) to yield the pure product. Pure 5-FAM-CD44BP was obtained in ~30% yield from the crude peptide and its purity was ascertained by analytical RP-HPLC, with an excellent purity of the 98%, as shown previously (Figure 2B).

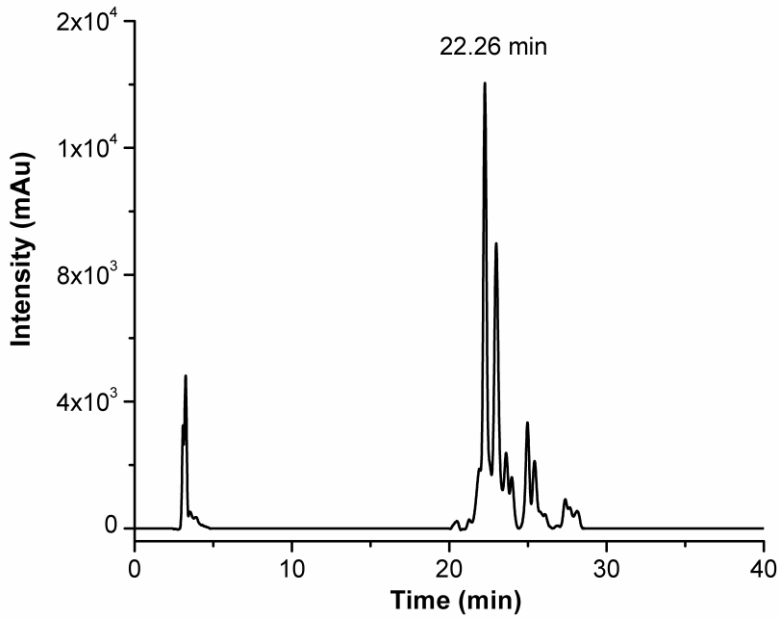

Figure 5: *Preparative RP-HPLC chromatogram of the crude 5-FAM-CD44BP peptide; the chromatogram was followed at λ = 220 nm.*

Cellular uptake of CD44BP

In order to verify the CD44BP peptide recognition by CD44 receptor, cellular uptake experiment was performed. The binding and internalization of the CD44BP into cells was evaluated by confocal microscopy. Because it's widely reported that human primary glioblastoma cell line (U-87) over-express CD44 receptor, it was chosen as positive control[15]. Instead human umbilical vein endothelial cells (HUVECs) were considered as negative control due to their low CD44-expression[18]. In Figure 6 normalized value of expression of CD44 in different cell lines provided by Human Protein Atlans[19] is reported. U-87 over-expression of CD44 was also verified by real-time PCR analysis (Figure 7).

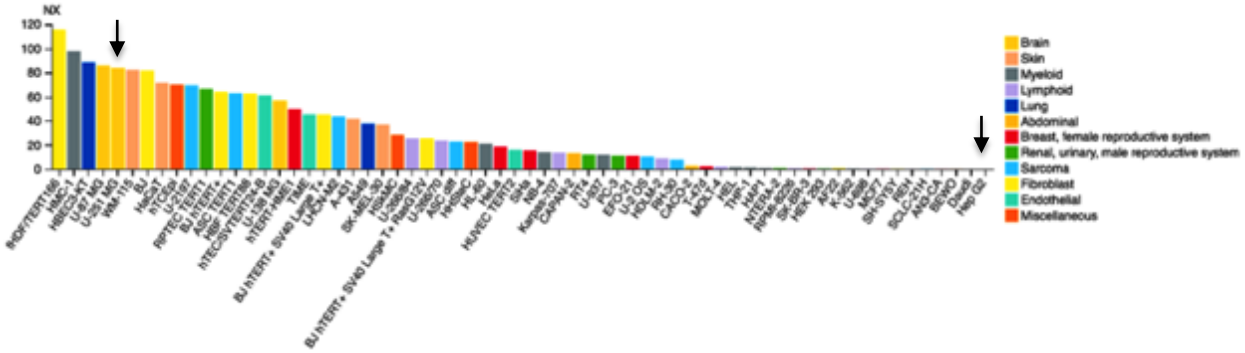

Figure 6: *Cell lines ordered by descending CD44 expression order. Black arrow indicates the position of U87 cells on the left and HepG2 on the right. Image available from www.proteinatlas.org.*

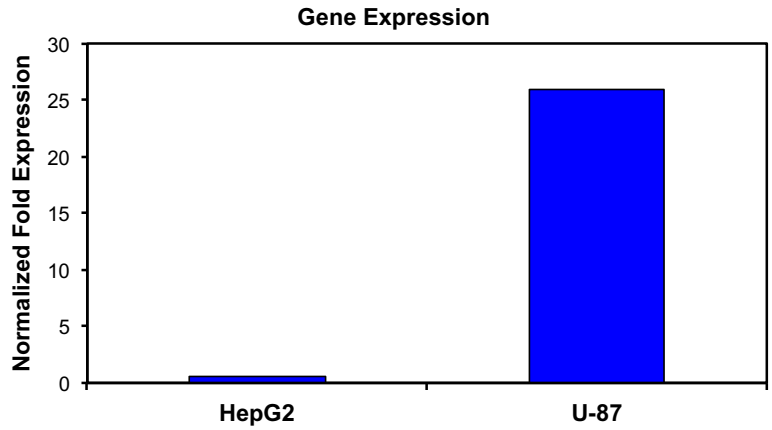

Figure 7: *Real-time PCR analysis of CD44 expression for U-87 and HepG2 cell lines.*

Figure 8 shows confocal images of a confluent monolayer of U-87 and HUVEC cells treated with CD44BP peptide (8.75 μM) at 37 °C for 1 hour under standard cell culture conditions. The peptide was completely internalized in glioblastoma cells; as it is possible to observe better internalization in the images obtained at high magnification. U-87 cells are positive to CD44BP internalization 87% more than HUVECs (Figure 9). This can be ascribed to the specific peptide recognition by CD44-receptor over expressed by tumor cells.

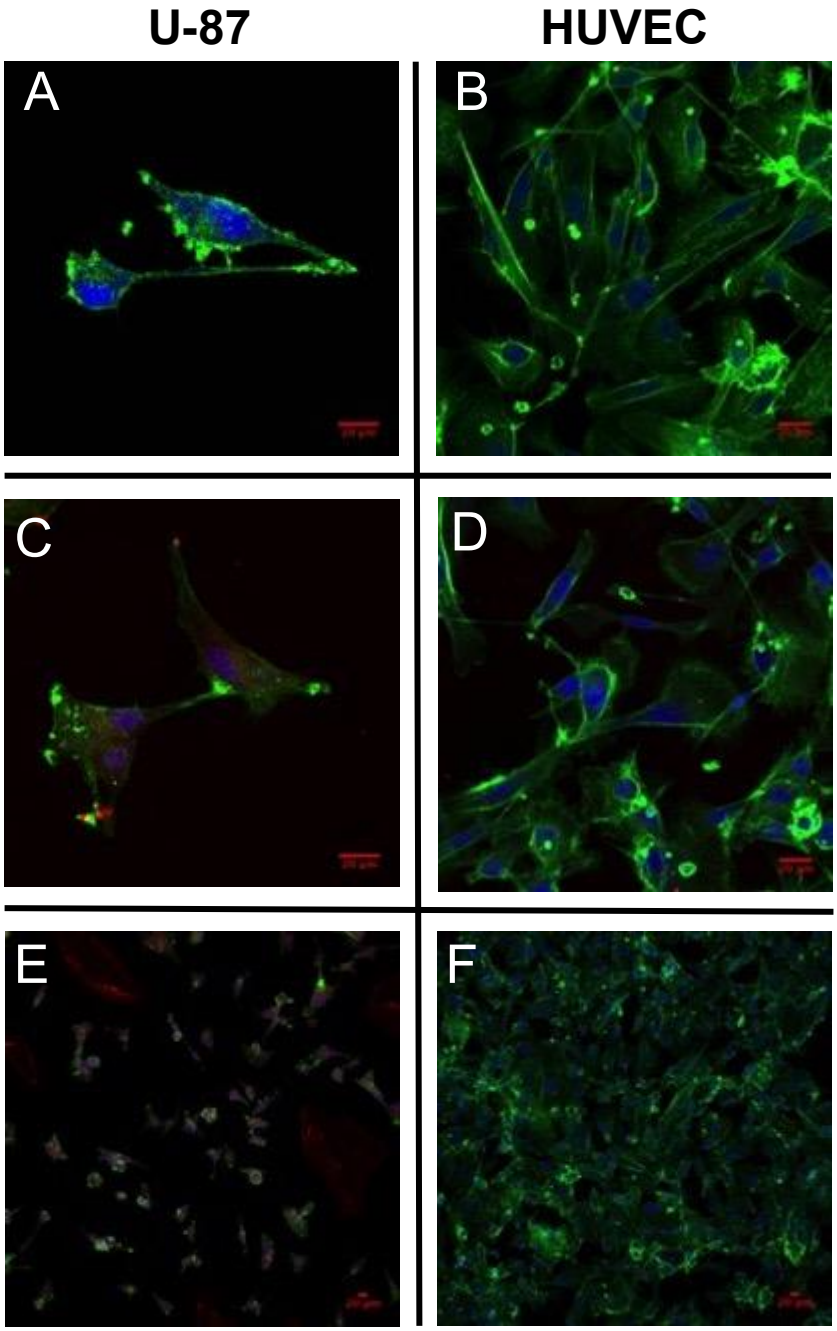

Figure 8: *Confocal images for 5-FAM-CD44BP interactions with a confluent monolayer of U-87 (C, E) and HUVEC (D, F). For each cell line it's reported the image of the cell untreated as control (A, B). Nuclei (blue) and cytosol (green) of the cells were stained with DRAQ5 and Phalloidin 555 respectively, while red color represents peptide uptake. Scale bar was 20μm.*

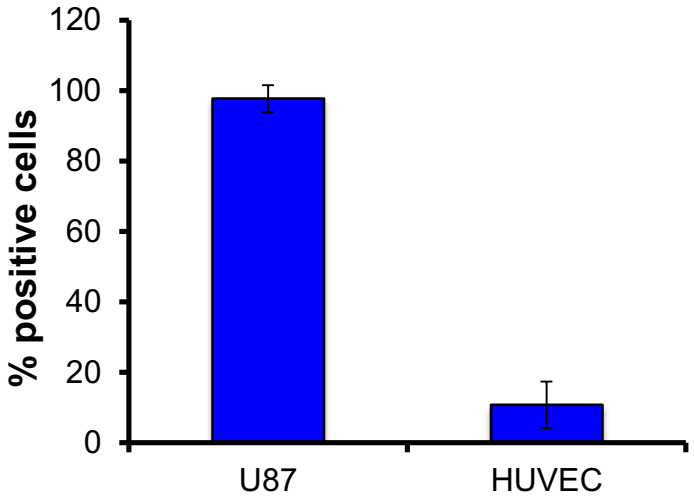

Figure 9: *CD44BP uptake in U87 and HUVEC cell lines. It's reported the number of positive cells to the peptide as mean (n=3) ± SD.*

Synthesis and purification of PEGylated peptide

In order to functionalize O/W NEs with CD44BP, the amino acid sequence was synthesized manually, in a modified version respect to that one previously mentioned, with a spacer of three glycine and a cysteine residues at the N-terminal (CGGG-RLVSYNGIIFFLK). Although the peptide itself has reactive functional groups such as $-NH_2$, the modification of a side group could change its activity. Therefore, cysteine residue was inserted in the sequence for the PEGylation in order to exploit the thiol-maleimide reaction between the lateral chain of cysteine and maleimide-PEG_{2k}-biotin linker. The three glycine had a role of spacer in order to make the peptide free to acquire its conformation when conjugated and to space out from the PEG_{2k} linked to cysteine. Also in this case, a coupling with 5-carboxyfluorescein was performed to label the peptide at the N-term as described before. The peptide synthesis was performed exploiting the orthogonality of solid-phase peptide strategy (SPPS), using 9-fluorenylmethoxycarbonyl (Fmoc) chemistry and a super acid labile resin. All synthetic phases were made directly on the resin, including the coupling of maleimide-PEG_{2k}-biotin linker to peptide (5-FAM-CD44BP-PEG_{2k}). Usually, size-exclusion chromatography (SEC) technique is used to purify PEGylated macromolecules. It separates molecules according to differences in size as they pass through a gel filtration medium packed in a column. In our case, PEGylated peptide and unreacted PEG_{2k} linker have a very small size difference (~ 2000 Da), making their separation by SEC difficult. Thanks to solid-phase approach, the purification of unreacted maleimide-PEG_{2k}-biotin from PEGylated peptide was widely simplified. Several steps of resin washing were performed after the reaction was over, to remove the unreacted reagent. A schematic representation of synthetic strategy is shown in Figure 10.

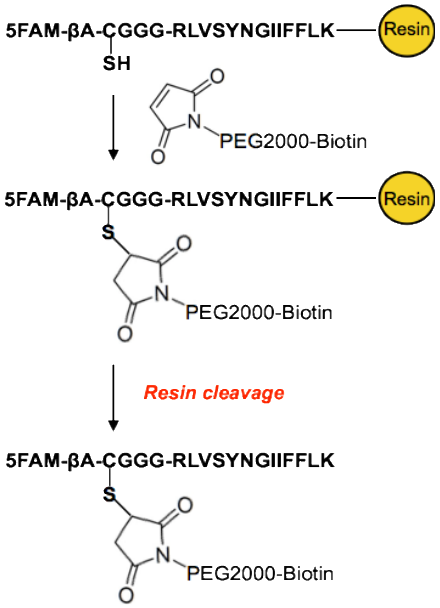

Figure 10: *Schematic representation of the solid-phase synthetic strategy of PEGylated peptide.*

Once the peptide coupling with the maleimide-PEG_{2k}-biotin linker was done, it was deprotected and cleaved from the resin. The crude peptide purity was assessed by analytical RP-HPLC, using a C-18 column with a linear elution gradient. The crude Biotin-PEG_{2k}-maleimide-peptide (5-FAM-CD44BP-PEG_{2k}) was purified by preparative flash chromatography, using a Biotage ISOLERA flash purification system. The pooled fractions, containing the desired products were analyzed by analytical RP-HPLC. In Figure 11 are reported HPLC chromatograms of the crude and purified PEGylated peptide chain.

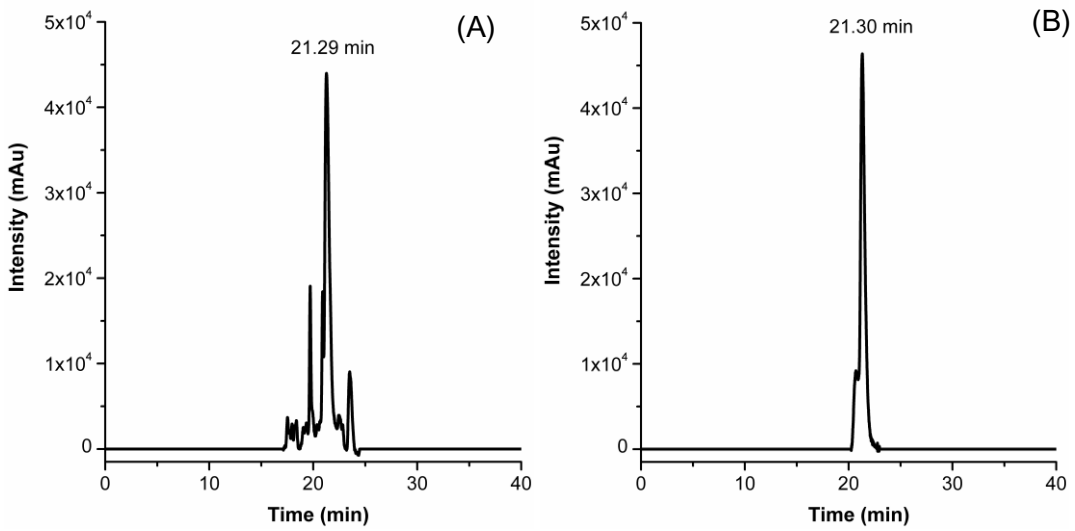

Figure 11: *Analytical RP-HPLC of 5-FAM-CD44BP-PEG$_{2k}$ crude peptide (A) and purified one (B). The chromatogram were detected at λ = 220 nm.*

The identification of the product at R_t = 21.25 min was accomplished through matrix-assisted laser desorption/ionization mass spectrometry coupled to two time of flight analyzers (MALDI-TOF-TOF). In figure 12 the centroid mass spectrum of maleimide-PEG$_{2k}$-biotin linker acquired before the peptide conjugation is reported. An intense, singly charged polydisperse Gaussian distribution was observed with the most abundant ion at 2411.59 *m/z* and the typical expected ethylene oxide repeat unit of 44 Da, proving the presence of PEG within the sample. Respect to theoretical expected mass, the reported one showed an increment of +23 *m/z* due to the sodiated species $(MNa)^+$. Because of the high affinity of PEG for both sodium and potassium, a cationization with Na^+ was often observed[20]. After peptide conjugation, a shift of polydisperse ion distribution to higher value of *m/z*, centered around 4704.71 ± 44 Da, was observed. The increment of mass value is evidence that the reaction took place. The theoretical isotopic mass of 5-FAM-CD44BP and 5-FAM-CD44BP-PEG$_{2k}$ were 2271.08 Da and 4659.67 ± 44 Da respectively, in accordance with experimental one, reported in the Figure 12.1 and Figure 12.2.

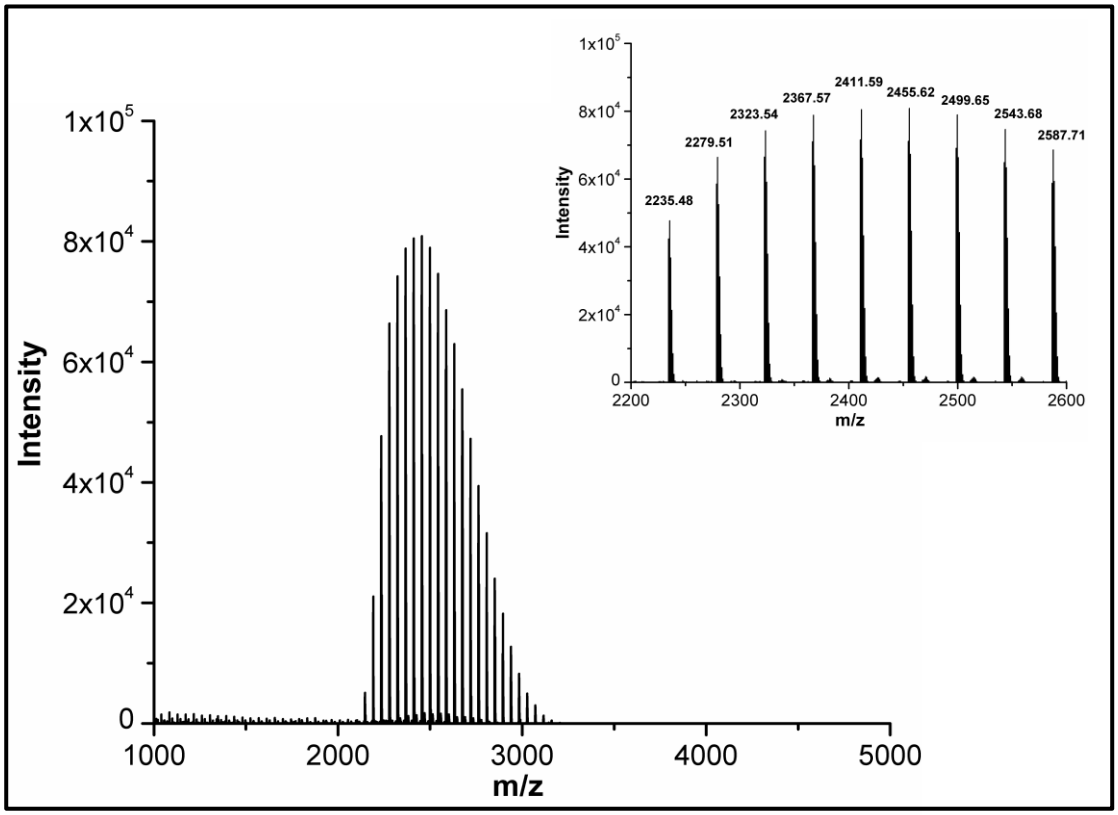

Figure 12.1: *MALDI mass spectra (centroid) of Biotin-PEG$_{2k}$-Maleimide linker.*

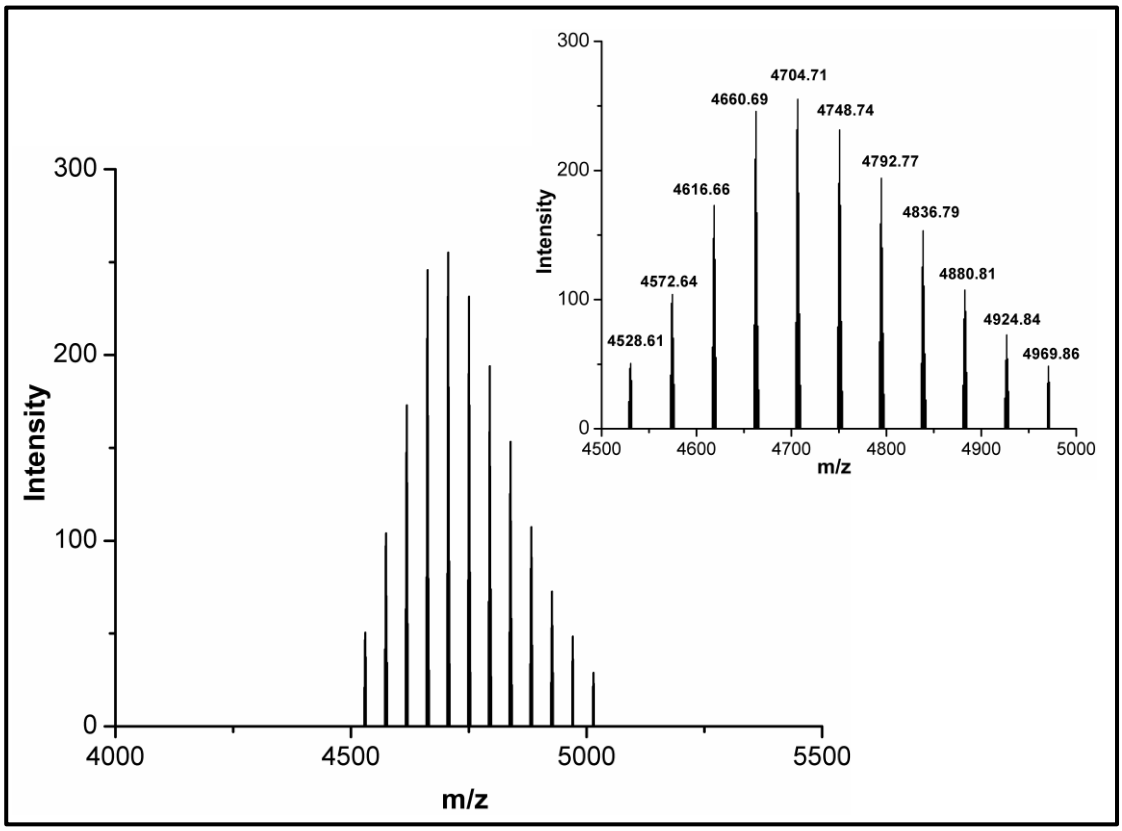

Figure 12.2: *MALDI mass spectra (centroid) of 5-FAM-CD44BP-PEG$_{2k}$ peptide.*

Nanocarrier assembly

Once a complete characterization of all components of NCs object of this PhD project was performed, a whole assembly of multi-phased system was done. Firstly, the streptavidin was added to the curcumin loaded HA-biotin-CT-O/W NEs under sonication at a ratio 1:1 with the biotin, in accordance with ITC results described in the previous chapter. Then, 5-FAM-CD44BP-PEG$_{2k}$ was added to the streptavidin-HA-biotin-CT-O/W NEs under sonication at a ratio 2:1 with the streptavidin. The complete functionalized NCs were characterized by DLS, whose measurements are reported in Figure 13 and Table 2. As illustrated, an increment of size and Z-potential inversion occurred passing

from O/W NEs to monolayer (CT) and bilayer (HA-biotin) since the polymers form firstly a positive layer around the oil core and then a negative one. The next steps of conjugation did not change significantly the nanoparticle size in agreement with both the low degree of functionalization and the small dimensions of streptavidin (~4-7 nm) respect to the NC, as reported in literature[21,22].

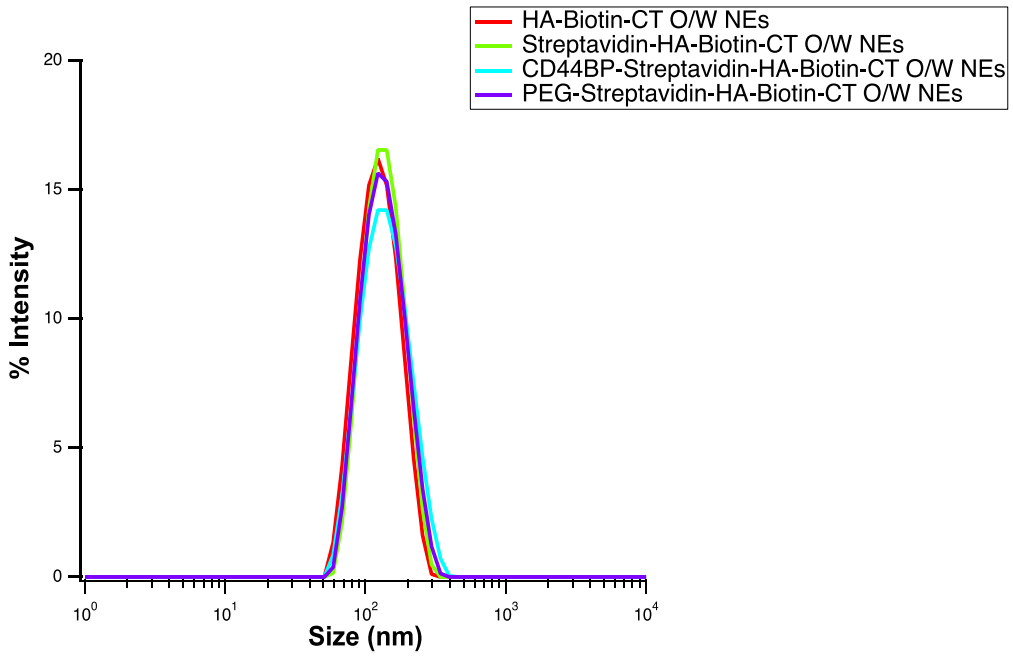

Figure 13: *Overlapping of mean hydrodynamic size of each component deposited around O/W NEs.*

Table 2: *Size, PdI and Z-potential measurements of each NCs component, loaded with curcumin, during the several steps of assembly. Data are reported as mean (n=3) ± SD.*

	Size (nm)	PdI	Z-potential (mV)
O/W NEs	97.47 ± 4.70	0.103 ± 0.009	-30.93 ± 4.40
CT-O/W NEs	111.70 ± 7.30	0.110 ± 0.050	+27.0 ± 12.00
HA-biotin-CT-O/W NEs	128.93 ± 7.30	0.098 ± 0.019	-35.16 ± 3.45
Streptavidin-HA-biotin-CT-O/W NEs	133.85 ± 11.30	0.132 ± 0.038	-29.35 ± 2.55
CD44BP-Streptavidin-HA-biotin-CT-O/W NEs	134.45 ± 10.40	0.115 ± 0.010	-28.62 ± 2.63
PEG-Streptavidin-HA-biotin-CT-O/W NEs	134.20 ± 12.10	0.134 ± 0.036	-27.43 ± 1.41

The morphological characterization of curcumin loaded multilayers polymer coated O/W NEs was performed by cryo-TEM analysis as reported in Figure 14. The sample, imaged in its frozen hydrated state, resulted to be formed by a well-defined electron-dense core, corresponding to the curcumin loaded in the oil template; which makes it difficult to observe polymer layers around the O/W NEs. The size distribution is in agreement with the results from the DLS analysis.

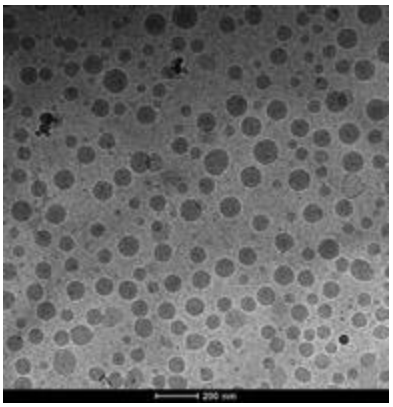

Figure 14: *Cryo-TEM projection image of curcumin loaded HA-CT-O/W NEs. Scale bar was 200 nm.*

Overall, DLS periodical measurements were carried out to evaluate the dimensional evolution over time. Figure 15 shows that CD44BP-PEG_{2k}-streptavidin-HA-biotin-CT-O/W NEs maintains its hydrodynamic diameter and the PdI values remained < 0.2 for several weeks, relative to the freshly prepared one, indicating no significant aggregation or dissociation.

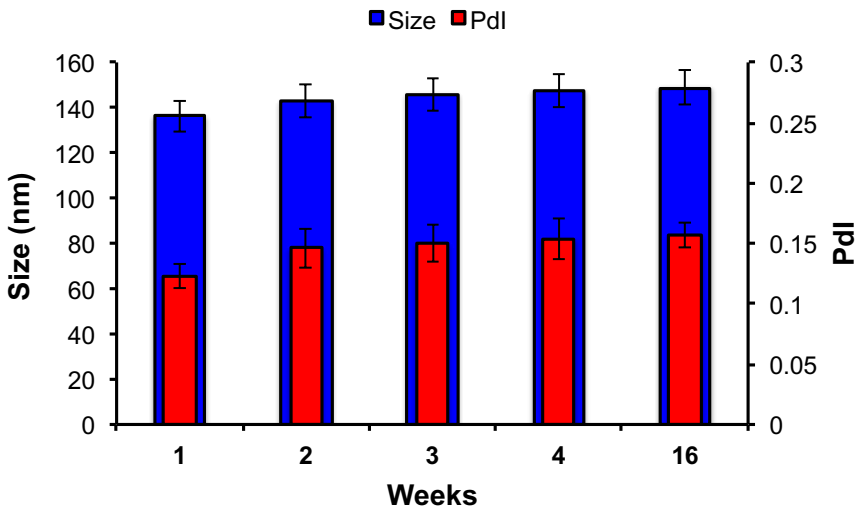

Figure 15: *Dimensional behaviour over time for curcumin loaded CD44BP-PEG_{2k}-streptavidin-HA-biotin-CT O/W NEs measured by DLS analysis.*

Streptavidin and 5-FAM-CD44BP-PEG$_{2k}$ colocalization analyses

Colocalization of streptavidin and CD44BP-PEG$_{2k}$ built around the O/W NE was evaluated by confocal microscopy to confirm the specific interaction between them. To this purpose, Atto 655 conjugated to streptavidin and 5-FAM to peptide were used as dyes. A pair of fluorophores with excitation and emission spectra far enough apart from each other to avoid any cross talk between them were chosen. A widely reported method to evaluate the extent of colocalization is a simple images overlay deriving from different channels [23]. In Figure 16 the superimposition of the red channel for the streptavidin and the green one for the peptide is shown. The resulting yellow color shows colocalization between the green and red signals. However, this method has intrinsic limits due to the high dependence of yellow areas by signal intensity collected in both channels. It may be used only when the histograms of each channel are similar. To overcome these problems and make the analysis more robust, an image intensity correlation coefficient-based (ICCB) analysis was performed by the "colocalization" LAS-AF software tool. The Pearson's coefficient was calculated to estimate the strength of co-localization between streptavidin and CD44BP-PEG$_{2k}$. Its value can range between +1 and -1, with +1 standing for complete positive correlation and -1 for a negative correlation, and with zero standing for no correlation. In our case, Pearson's coefficient resulted to be 0.491 ± 0.043; showing a good positive co-localization. This result was confirmed also by the values of the "overlap coefficient" of 0.511 ± 0.046 and of the % colocalization rate (percentage of colocalizing area respect to total area of green + red) of 37.59% ± 7.25 provided by Leica software. Parameters were calculated as mean from at least three images (n=3).

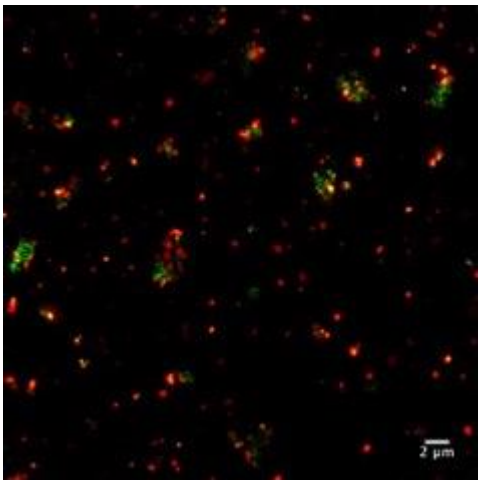

Figure 16: *Overlay of confocal images of the Atto streptavidin-655 (red) and 5-FAM-CD44BP-PEG$_{2k}$ (green) built above the O/W NEs. Scale bar is 2 µm.*

In vitro cytotoxicity analysis

To understand the behaviour of our peptide functionalized NCs, assembled as described before, toward cancer cell lines, biological analyses were carried out. The lipophilic oil core of the O/W NEs used as template for multi-component depositions was pre-loaded with curcumin, which is a hydrophobic natural agent that has already demonstrated its anticancer effects towards cancer cells, including U-87 tumor cells. Curcumin bioactivity was restricted by its poor solubility and bioavailability, reported to be 11 ng/mL in aqueous buffer, making it hard for preparation of aqueous solution of curcumin for intravenous use[24,25]. Curcumin has been shown to suppress multiple signaling pathways and inhibit cell proliferation, invasion, metastasis, and angiogenesis, controlling several gene involved in cell death pathways[26]. In order to understand the appropriate incubation time to appreciate the curcumin activity as anti-tumour agent, a confluent monolayer of U-87 cells was incubated with curcumin loaded CD44BP-PEG$_{2k}$ O/W NEs, diluted 1:5 in cells, at a final curcumin concentration of 62.8 µM for several times (30 min, 1

h, 2 h and 4 h). Moreover, cells were treated with standard cell medium alone as positive control and with free curcumin as negative control. After incubation, cells were washed and a quantitative evaluation of cell viability (normalized to positive control, which is set to 100%) was obtained by PrestoBlue assay after 24 h.

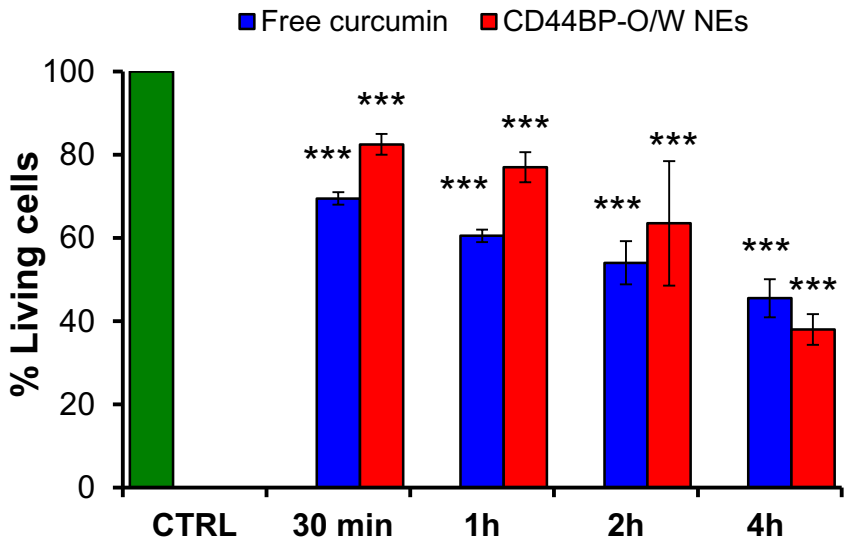

Figure 17: *Cytotoxicity assay of curcumin loaded CD44BP-PEG$_{2k}$ O/W NEs and free curcumin. U-87 cells were treated for several times of incubation and cell viability was evaluated after 24 h. Data are reported as mean of three independent experiment (n=3 ±SD) and expressed as percentage compared to control cells. The asterisk (***) indicates the statistical significance vs CTRL using Student's t test considering a p value ≤ 0.001.*

Data has shown an increase of cell mortality both for free curcumin and for CD44BP-PEG$_{2k}$ O/W NEs over time. Indeed, curcumin significantly inhibited the vitality of U-87 cells in a dose and time dependent manner as largely reported[27,28]. A reversal in the trend between two treatments was observed after 4 h of incubation, indicating the time needed for CD44BP-PEG$_{2k}$ O/W NEs respect to free curcumin to be internalized and release their cargo (Figure 17). Chao Cheng *et al.* reported that the inhibitory effects of curcumin for U-87 cell

lines were most evident when used at a concentration of 40 μM, much lower than that used by us, which is completely within the range widely reported[29]. In fact, one of the strengths of O/W NE, which is the real core of our NCs, is the possibility to carry a huge amount of hydrophobic substances, limited only by the degree of solubility, that for the curcumin loaded in our O/W NEs (20% oil) was 4.2 mg/mL. For example, our formulation has a two-fold curcumin concentration respect to the curcumin incorporated in lipid nanoemulsions developed by Hideki Ichikawa *et al.* (2.4 mg/mL)[30]. Pharmacokinetics results of an aqueous nanosospension of curcumin (CUR-NS) compared to free curcumin, after intravenous administration (i.v.) in rabbits, conducted by Guangxi Zhai *et al.*, showed that CUR-NS, at a curcumin concentration of 9.45 μg/mL, presented a mean residence time 11.2-fold longer[31]. Compared to CD44BP-PEG_{2k} O/W NEs (2.78 wt% of oil), which has a curcumin concentration of 115.83 μg/mL, we could expect an increment of curcumin bioavailability for i.v. administration. Once identified an appropriate incubation time, control experiments were carried out treating cells with the un-functionalized NCs. A confluent monolayer of U-87 cells were incubated with curcumin loaded CD44BP-PEG_{2k} O/W NEs and PEG_{2k}-O/W NEs, diluted 1:5 in cells, at a final curcumin concentration of 62.8 μM for 4 h for both of them. PEG_{2k}-O/W NEs act as negative control because it was assembled with the same streptavidin-biotin strategy described before, exhibiting on the external nanocarrier shell a layer of PEG_{2k} (the same used for peptide PEGylation), without the targeting conjugated moieties. Moreover, cells were treated with cell medium alone as positive control and with free curcumin as second negative control. After incubation, cells were washed and a quantitative evaluation of cell viability (normalized to positive control, which is set to 100%) was performed after 24 h (Figure 18). Data showed a significant cytotoxicity effect of CD44BP-PEG_{2k} O/W NEs compared to blank.

This is an evident consequence of peptide capability to accumulate the nanocarrier on the cells, thanks to ligand-receptor recognition, and allow its internalization. CD44BP-PEG_{2k} O/W NEs exhibit an increase of 40% of cell death respect to un-functionalized NCs, and a little difference in comparison with free curcumin.

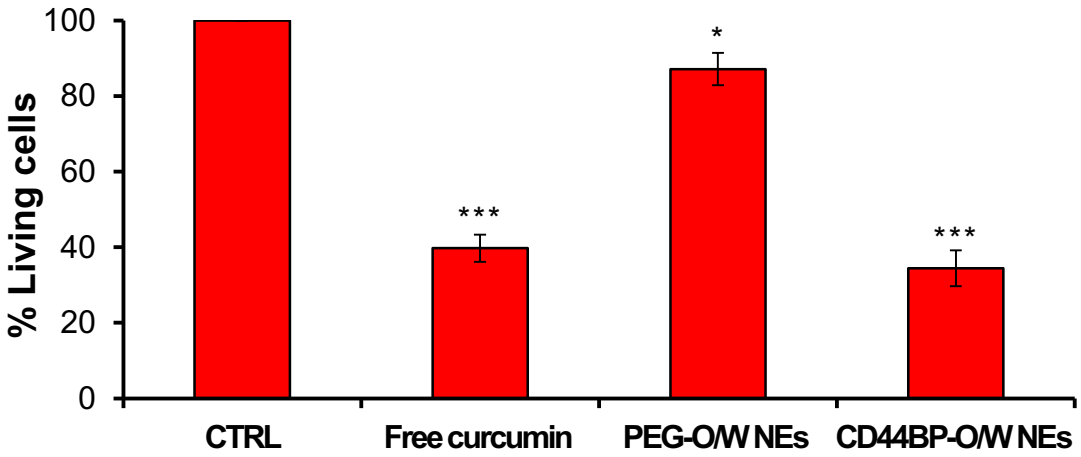

Figure 18: *Cytotoxicity assay of curcumin loaded CD44BP-PEG_{2k} O/W NEs and PEG_{2k} O/W NEs, and free curcumin. U-87 cells were treated for 4h of incubation and cell viability was evaluated after 24 h. Data are reported as mean of three independent experiments (n=3 ±SD) and expressed as percentage compared to control cells. The asterisk (*) indicates the statistical significance vs CTRL using Student's t test considering a p value <0.05; (***) p ≤ 0.001.*

In 2D cell cultures, we are obtaining similar results between free curcumin and encapsulated curcumin. The advantage of encapsulation is that once in vivo the encapsulated curcumin will be protected and could be injected at much higher concentration as compared to free curcumin. Indeed, O/W NEs has been the function to protect curcumin from hydrolysis and degradation, without affecting its anti-cancer activity[32]. In addition, CD44BP-PEG_{2k} O/W NEs were functionalized with a PEGylated peptide that has a dual function: improve the shelf life of NCs thanks to anti-fouling properties of PEG chains and accumulate it to cancer site thanks to peptide-receptor recognition.

Binding and uptake of CD44-Targeted NCs by CD44-Expressing cancer cells

A cellular uptake assay by confocal microscopy was performed to better investigate the cytotoxicity results and understand if the mortality effect observed could be attributed to curcumin action. Because curcumin has intrinsic fluorescence properties, it could be used by itself as probe for NCs detection. A confluent monolayer of U-87 cells were incubated with curcumin loaded CD44BP-PEG_{2k} O/W NEs and PEG_{2k} O/W NEs, for 4 h at the same experimental condition of cytotoxicity test described before. In addition, cells treated with cell medium alone were considered as control (CTRL).

Figure 19 shows confocal microscopic images of U-87 cell monolayers after NCs uptakes, which strongly support the previous cytotoxicity results by showing strong fluorescence difference between CD44BP-PEG_{2k} O/W NEs and PEG_{2k} O/W NEs. However, no fluorescence can be detected from the images of the control cells (Figure 19 A, B). The presence of curcumin, appearing in red, in the cells cytoplasm as well as in the nuclei was clearly more evidenced for peptide functionalized NCs (90 ± 24 % more respect to the negative control). A possible explanation is that the peptide induces much higher internalization, in accordance with CD44BP uptake in U-87 cells described before. Furthermore, a slight amount of PEG_{2k} O/W NEs was detected in the cells. A probable justification could be attributed to passive internalization exerted by NCs especially those with diameters smaller than 200 nm, as ours. In Figure 20 is shown a plot of mean fluorescence intensity of curcumin encapsulated in CD44BP-PEG_{2k} O/W NEs and PEG_{2k} O/W NEs normalized for the cells number. Data are expressed as mean of several images taken by at least three wells.

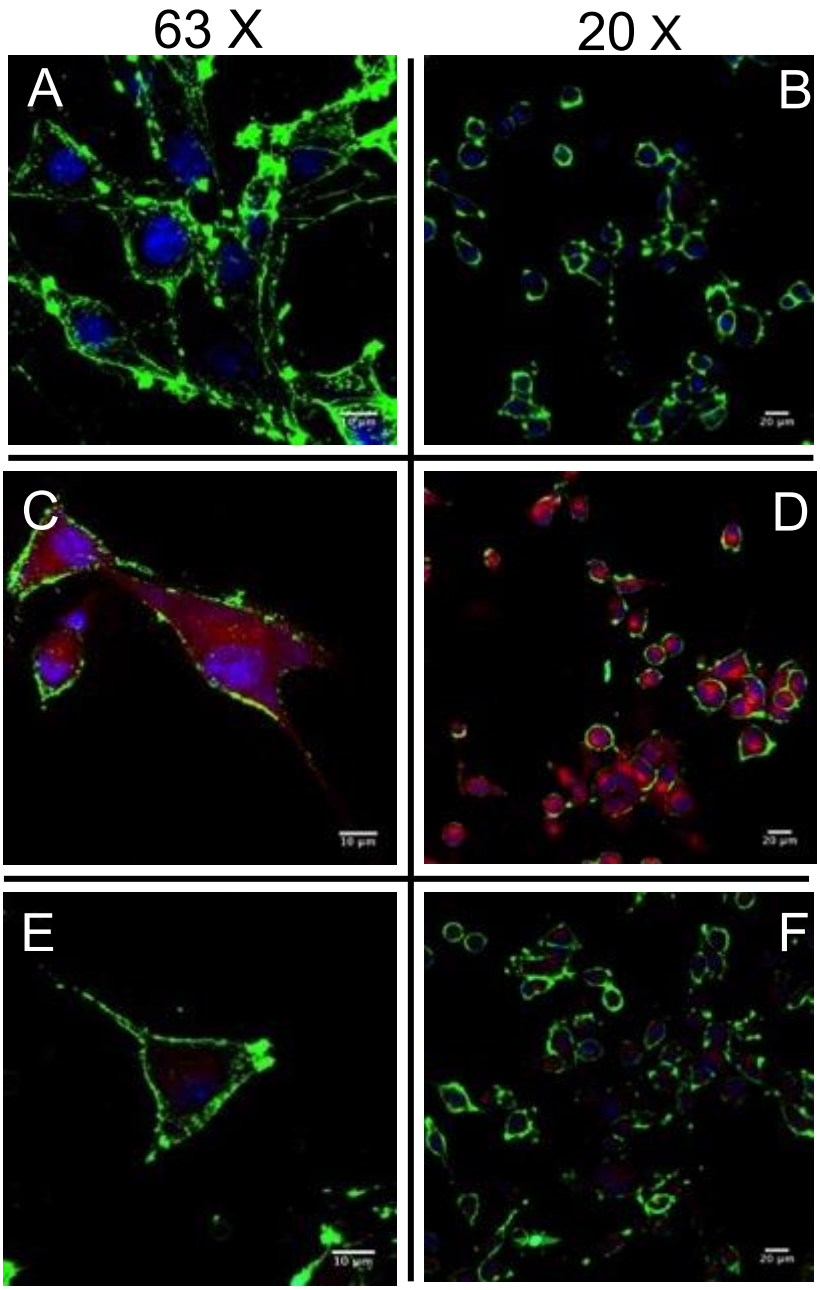

Figure 19: *Confocal images of U-87 cells. Untreated (A, B), curcumin loaded CD44BP-PEG_{2k} O/W NEs (C, D) and curcumin loaded PEG_{2k} O/W NEs (E, F) interactions with a confluent monolayer of U-87 cells. Nuclei (blue) and cellular membrane (green) of the cells were stained with DAPI and WGA 555 respectively, while red color represents curcumin uptake. 60X and 20X refer to microscope objective. Scale bar is 10 μm for 60X images and 20 μm for 20X images.*

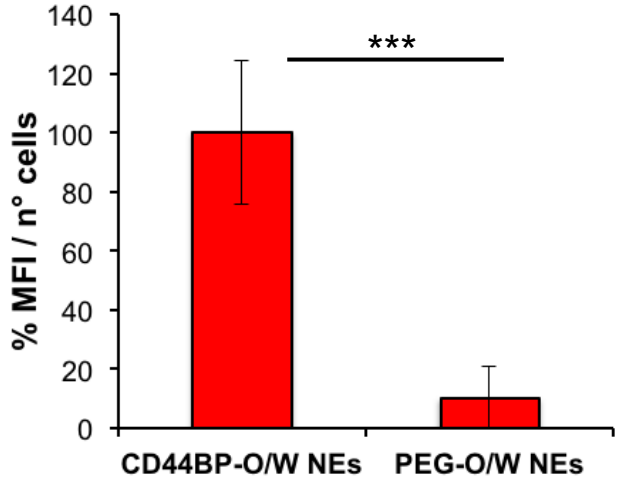

Figure 20: *Plot of mean fluorescence intensity of curcumin normalized to cells number. U-87 cells were treated with curcumin loaded in CD44BP-PEG$_{2k}$ O/W NEs and PEG$_{2k}$ O/W NEs. Data are reported as mean (n=3) ± SD.*

Active targeting comparison between CD44BP and HA outer layer O/W NEs

As described before, a bilayer of chitosan and hyaluronic acid was used to stabilize NEs. Hyaluronic acid, in addition to be the external layer of our NCs, which was subsequently functionalized with the peptide, it is also the main ligand for CD44 receptor. In order to better investigate the tumour specificity of CD44BP-functionalized NCs, a comparison with hyaluronic acid coated NCs was performed, both with CD44 over-expressing tumour cells U-87 and with healthy HUVEC cell lines. Cytotoxicity test was performed using curcumin as bioactive agent encapsulated in the oil phase. A confluent monolayer of HUVEC and U-87 cells were incubated with curcumin loaded HA-coated O/W NEs, CD44BP-PEG$_{2k}$ O/W NEs, and PEG$_{2k}$-O/W NEs, diluted 1:5 in cells, at a final curcumin concentration of 62.8 μM for 4 h for all of them. As described before, PEG$_{2k}$-O/W NEs act as negative control. Moreover, cells were treated with cell medium alone as positive control and with free curcumin as second negative control. In addition, HA-coated O/W NEs act as second positive control being

constituted of the main ligand of CD44 receptor. After incubation, cells were washed and a quantitative evaluation of cell viability (normalized to positive control, which is set to 100%) was performed after 24 h (Figure 21).

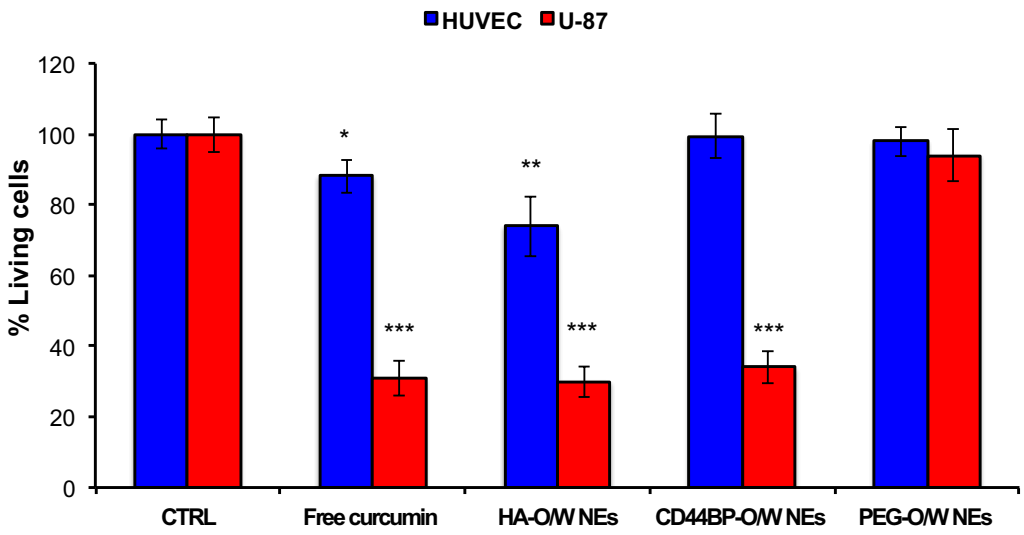

Figure 21 *Cytotoxicity assay of curcumin loaded HA-CT O/W NEs, CD44BP-PEG$_{2k}$ O/W NEs, PEG$_{2k}$ O/W NEs, and free curcumin. U-87 and HUVEC cells were treated for 4h of incubation and cell viability was evaluated after 24 h. Data are reported as mean of three independent experiments (n=3 ± SD) and expressed as percentage compared to control cells. The asterisk (*) indicates the statistical significance vs CTRL using Student's t test considering a p value <0.05 (*), p ≤ 0.01 (**), p ≤ 0.001 (***).*

Cytotoxic test for U-87 cells of curcumin loaded and empty HA-coated O/W NEs is reported in Figure 22. The carrier itself has been demonstrating to be almost completely safe.

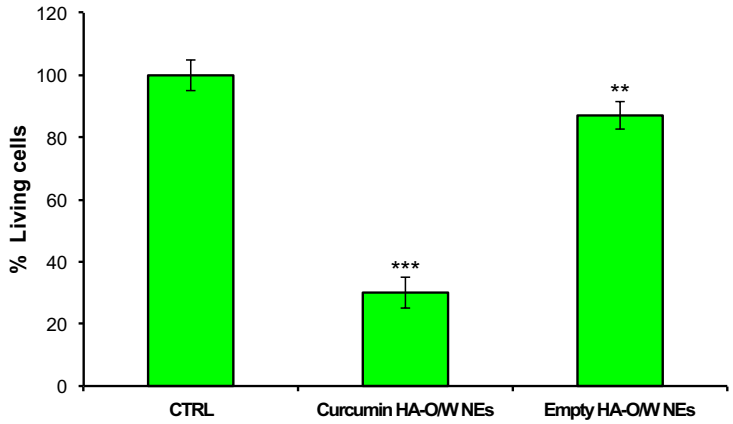

Figure 22 *Cytotoxicity assay of curcumin loaded and empty HA-CT O/W NEs. U-87 cells were treated for 4h of incubation and cell viability was evaluated after 24 h. Data are reported as mean of three independent experiments (n=3 ± SD) and expressed as percentage compared to control cells. The asterisk (*) indicates the statistical significance vs CTRL, p ≤ 0.01 (**), p ≤ 0.001 (***).*

As expected, in the case of U-87, curcumin loaded HA-coated O/W NEs induced cells death almost similar to CD44BP-PEG_{2k} O/W NEs. This is a further proof of specific ligand-receptor interaction. Conversely, no cytotoxic effect is observed for CD44BP-PEG_{2k} O/W NEs for the HUVEC cells due to the lack of CD44 over-expression. In the case of the HUVEC cells, the low toxic effect of curcumin with respect to U-87 should also be taken into account. However, as described before, the concentration of curcumin loaded in our NCs is high, so it is in the range that could induce a slight toxicity[33,34], this was also confirmed by the percentage of living cells when treated with free curcumin (88 ± 4 %). For both cell lines, PEG_{2k}-O/W NEs has demonstrated to be totally safe, evidence of the completely shielding provided by PEG chains.

To deepen these results, cellular uptake assays by confocal microscopy were performed for both cell lines. A confluent monolayer of U-87 and HUVEC cells were incubated with curcumin loaded HA-coated O/W NEs, CD44BP-PEG_{2k} O/W NEs and PEG_{2k} O/W NEs, for 4 h at the same experimental condition of

cytotoxicity test described before. In addition, the control (CTRL) consisted in cells treated with cell medium alone.

Figure 23 and 24 show confocal microscopic images of U-87 and HUVEC cell monolayers after NCs uptakes, which shed light on the previous cytotoxicity results in an independent manner from curcumin activity. The presence of curcumin appeared in red, while the cells cytoplasm and the nuclei were in green and blue respectively. Images are representative of at least three independent experiments, and ten images were examined for each treatment. In Figure 25 and 26 are reported the plot of curcumin 'mean' fluorescence intensity normalized for the cells number for U-87 and HUVEC cell lines have been reported respectively. Interestingly the non-specific accumulation of HA-coated O/W NEs for both of cell lines could be seen. Instead, CD44BP-PEG_{2k} O/W NEs was specific for tumor CD44 over-expressing cells (U-87) and a very slight detection was found for the HUVECs one. Although HA was largely used as ligand for active targeting, we show its inability to be specific for tumor cells, without affecting healthy one. While, our peptide-functionalized NCs not only has been demonstrated to be tumor-selective, but also to accumulate in CD44 over-expressing cells 51.5 % more than HA-coated O/W NEs does. In addition, PEG_{2k} O/W NEs was not detected in both the cell lines, evidence that is the ligand-receptor interaction that promotes NCs internalization.

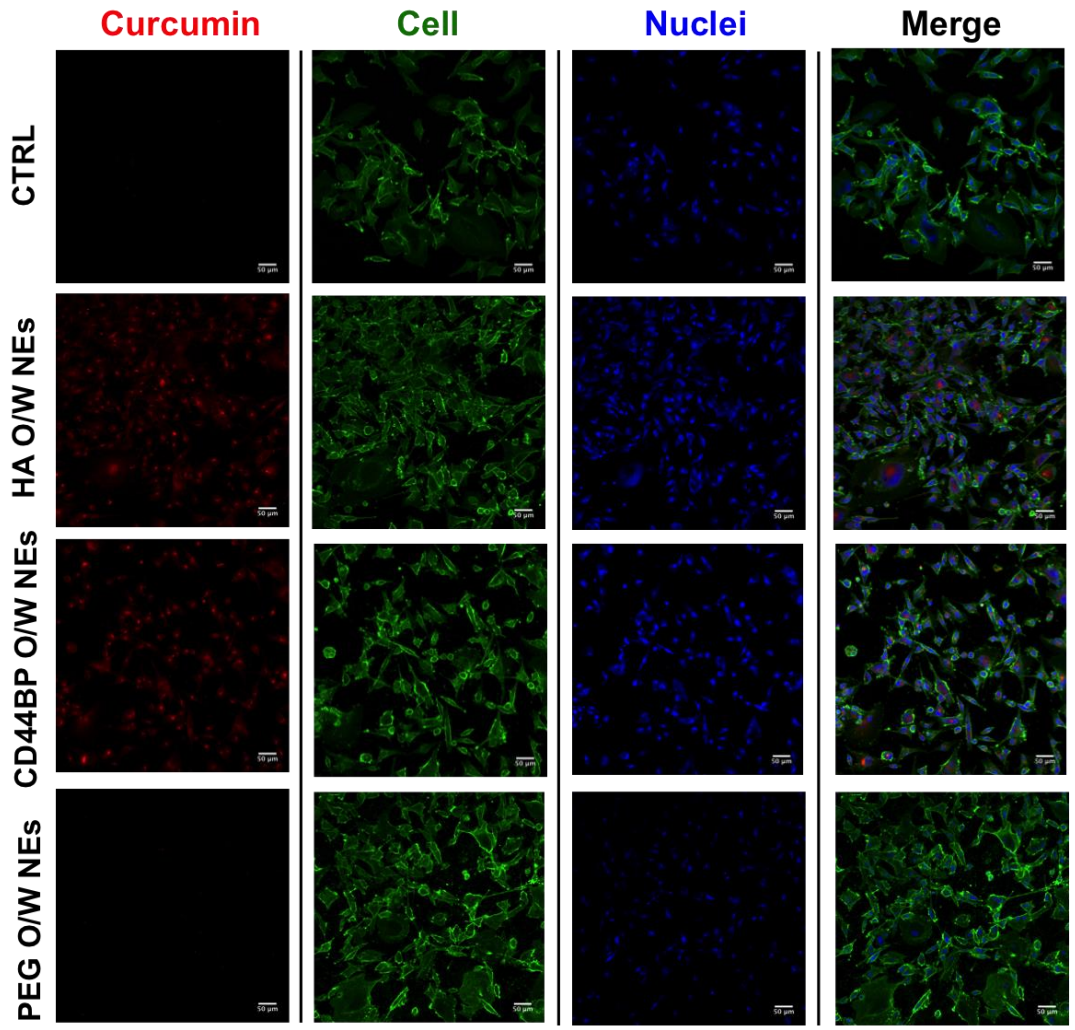

Figure 23: *Confocal images of U-87 cell. Untreated, curcumin loaded HA-CT O/W NEs, CD44BP-PEG$_{2k}$ O/W NEs and PEG$_{2k}$ O/W NEs interactions with a confluent monolayer of U-87. Nuclei (blue) and cellular membrane (green) of the cells were stained with DAPI and WGA 555 respectively, while red color represents curcumin uptake. Scale bar is 50 µm.*

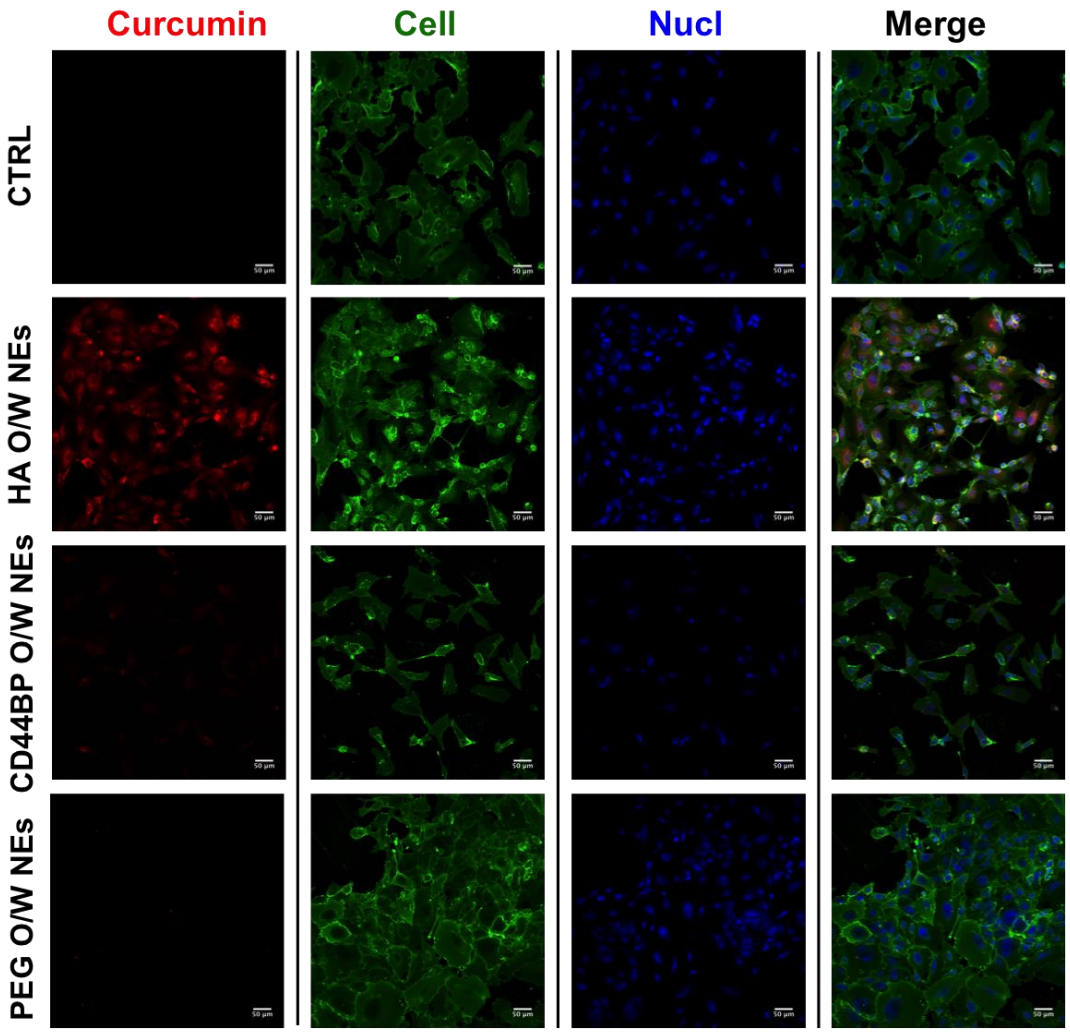

Figure 24: *Confocal images of HUVEC cell. Untreated, curcumin loaded HA-CT O/W NEs, CD44BP-PEG_{2k} O/W NEs and PEG_{2k} O/W NEs interactions with a confluent monolayer of HUVECs. Nuclei (blue) and cellular membrane (green) of the cells were stained with DAPI and WGA 555 respectively, while red color represents curcumin uptake. Scale bar is 50 µm.*

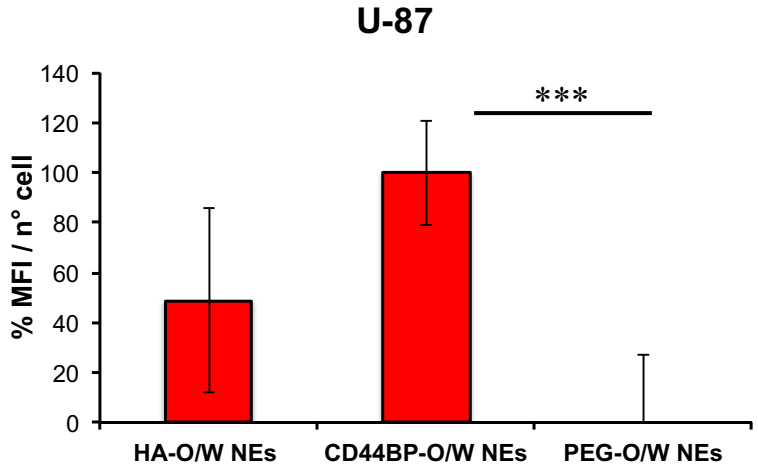

Figure 25: *Plot of mean fluorescence intensity of curcumin normalized to cells number. U-87 cells were treated with curcumin loaded in HA-CT O/W NEs, CD44BP-PEG$_{2k}$ O/W NEs and PEG$_{2k}$ O/W NEs. Data are reported as mean (n=3) ± SD.*

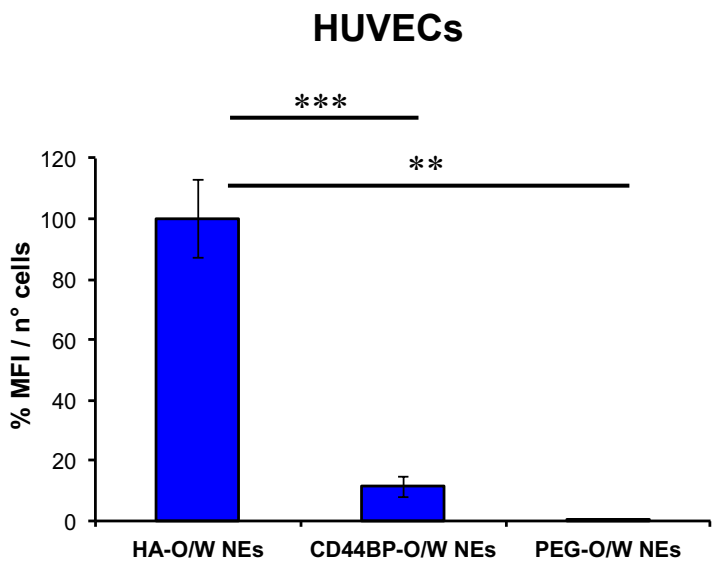

Figure 26: *Plot of mean fluorescence intensity of curcumin normalized to cells number. HUVEC cells were treated with curcumin loaded in HA-CT O/W NEs, CD44BP-PEG$_{2k}$ O/W NEs and PEG$_{2k}$ O/W NEs. Data are reported as mean (n=3) ± SD.*

Conclusions

In this work, we propose a surface functionalization of oil core polymer nanocapsules, based on bioactive peptide that recognizes CD44 receptor, for active targeting. Thanks to an easy additive approach, we have achieved a stable multilayer nano-carrier that induces cytotoxicity in glioblastoma cells that over-express CD44 receptor. Thanks to high binding affinity with biotin, streptavidin was used as linker to conjugate the synthetized peptide to the entire systems, while keeping nano-carrier stability. Uptake tests have demonstrated that both peptide and peptide-functionalized nanocapsules internalize in U-87 cells thanks to ligand-receptor binding. We compared the performance of curcumin loaded O/W NEs functionalized with CD44BP to that of the same system without the peptide and coated with hyaluronic acid that is the main ligand of CD44 receptor. U-87 and HUVEC cell lines were chosen as model of cancer site and healthy one respectively. Our results clearly demonstrate the ability of CD44BP peptide to target the human primary glioblastoma cells when conjugated to our engineered nanocarriers, also better of HA, thus paving the way to the design of novel multifunctional nanocarriers for delivery of therapeutic agents like curcumin. Further *in vitro* and then *in vivo* experiments will be performed in order to better understand the mechanism of interaction of the nanocarrier with tumours.

Materials and methods

Materials

Soybean oil and surfactant Lipoid E80 (egg lecithin powder 80-85% enriched with phosphatidylcholine and 7–9.5% content in phosphatidylethanolamine) were purchased from Lipoid GmbH and used without further purification. For preparation of all nanoemulsions and solutions, Millipore Milli-Q water was used. Chitosan (CT, LMW 90-150 kDa, DDA 84% determined via 1H-NMR), Curcumin (from *Curcuma longa* Turmeric, powder), 1-hydroxybenzotriazole hydrate (HOBt), N,N′-Diisopropylcarbodiimide (DIC), N,N-Diisopropylethylamine (DIEA), trifluoroacetic acid (TFA), dimethyl sulfoxide (DMSO), dichloromethane (DCM), anhydrous N,N-dimethyl-formamide (DMF), 1,2-Ethanedithiol (EDT), Triisopropylsilane (TIS) piperidine acetone, diethyl ether, dimethyl sulfoxide (DMSO), deuterium oxide (D_2O), Atto 655-streptavidin were purchased from Sigma Aldrich. Hyaluronic acid 250 kDa and biotin-PEG_{2k}-maleimide were purchased from Creative PEGWorks. N-α-Fmoc amino acids, HCTU and 5-Carboxy fluorescein were provided by NovaBiochem.

Peptide synthesis and purification

Targeting peptides CD44BP (5FAM- βA-RLVSYNGIIFFLK-NH_2) and a modified version, with a spacer of three glycine residues and a cysteine residue at the N-terminal (CGGG-RLVSYNGIIFFLK-NH_2) were synthesized manually. Protocols involving the use of 9-Fluorenylmethoxycarbonyl (Fmoc) chemistry and were used. The peptide scale synthesis was 0.1 mmol. It was assembled on H-Rink-amide ChemMatrix® resin with a substitution level of 0.4 mmol/g, using solid-phase peptide strategy[35].

Once loaded the resin in reaction vessel, it was swelled three times for 3 minutes with DMF and three times with NMP for 3 minutes.

The following protected amino acids were used to synthesize the peptide:

Fmoc-Lys(Boc)-OH; Fmoc-Leu-OH; Fmoc-Phe-OH; Fmoc-Ile-OH; Fmoc-Gly-OH; Fmoc-Asn(Trt)-OH; Fmoc-Tyr(tBu)-OH; Fmoc- Ser(tBu)-OH; Fmoc-Val-OH; Fmoc-Arg(Pbf)-OH; Fmoc-Cys(Mmt)-OH; Fmoc-Ala-OH.

The synthetic procedure can be summarized as follow:

1. Deprotection: Fmoc group was removed at the beginning of cycle with a 20% piperidine solution in DMF. After deprotection, the resin was washed with DMF to remove the residual piperidine. The peptide resin was then ready for coupling.
2. Activation: the carboxyl group of each Fmoc-amino acid was activated by addition of 7.5 equivalents of HCTU 0.48 M. Single coupling was conducted for each amino acid by addition of 15 equivalents of N, N'-diisopropylethylamine.
3. Coupling: the pre-activated Fmoc-amino acid reacted with the free amino-terminal group of the growing peptide chain on the resin using DMF as the reaction solvent. The resin was tested for the presence of unreacted amines using the Kaiser reagent. If the test was positive, the coupling reaction was repeated.
4. Capping: this reaction was performed after each coupling step, using Ac_2O/HOBt/DIEA solution in DMF. Capping cycle was introduced to prevent deletion byproducts.

Deprotection, coupling and capping steps were repeated with each subsequent amino acid, until the chain assembly was completed. When the coupling was complete, the resin was washed with DMF. At completion of the synthesis, the

resin was washed several times with DMF, NMP, DCM, isopropanol and methanol, and finally dried. The peptide was cleaved from the resin by treating with 94% TFA/2.5% EDT/2.5% water/1% TIS for 2 hours. The mixture was then concentrated under reduced pressure and transferred to glass centrifugal tubes for compound precipitation using ice-cold diethyl ether, which was performed repeatedly.

5-Carboxyfluorescein-peptide conjugation

The peptide was conjugated at the N-term with 5-carboxyfluorescein (5-FAM). Another non-α-amino acid (β-alanine) was introduced at the N-tem before the coupling reaction with 5-FAM to avoid an Edman-type elimination reaction[17]. β-alanine conjugation at the N-term was performed as described before. The coupling reaction of 5-carboxyfluorescein was conducted on the resin with DIC/HOBt/DIEA (1:1:2) 0.1 M; using DMF as solvent, overnight under nitrogen flow. At completion of the synthesis, the resin was washed several times with DMF, NMP, DCM, isopropanol and methanol, and finally dried.

Biotin-PEG_{2k}-Maleimide-peptide conjugation

Biotin-PEG_{2k}-Maleimide was linked to the peptide thanks to covalent bond between maleimide and the lateral chain of cysteine. Firstly, Mmt protecting group of cysteine was selectively removed whilst the peptide remained attached to the solid phase. It was performed by several wash cycles using 1% trifluoroacetic acid (TFA), 5% triisopropylsilane (TIS) in DCM[36]. The cleavage is repeated almost 10 times until no more yellow colour, due to Mmt release, can be detected. The thiol free group of cysteine was conjugated to the malemide group of Biotin-PEG_{2k}-Maleimide (1:5) directly on resin, using DMF as solvent and 10 molar excess of DIEA, overnight under nitrogen flow. At completion of the synthesis, the resin was washed several times with DMF, NMP, DCM, isopropanol and methanol to remove unreacted linker. Biotin-

PEG_{2k}-maleimide-peptide was cleaved from the resin by treating with 94% TFA/2.5% EDT/2.5% water/1% TIS for 2 hours, precipitated in ice-cold diethyl ether and lyophilized.

Peptides analysis and purification

The identity of crude peptides was analyzed by analytical RP-HPLC–ESI-MS. The LC-MS was performed with a Shimadzu LC-10ADvp equipped with an SPDM10Avp diode-array detector. ESI-MS spectra were recorded on a Shimadzu LC-MS-2010EV system with ESI interface and Shimadzu LC-MS solution Workstation software for the data processing. A Q-array-octapole-quadrupole mass analyzer was used as the detector. Mass tandem experiments were recorded on Shimadzu LC-MS-8040 triple quadrupole equipped with ESI ionization source. Argon was used as ion gas in the CID cell and data were analyzed by Shimadzu LC-MS solution Workstation software, while tandem mass spectra were analyzed using the software Molecular weight calculator. The optimized MS parameters were selected as followed: curved desolvation line (CDL) temperature 200°C; block temperature 200°C; probe temperature 200°C; detector gain 1.6 kV; probe voltage +4.5 kV; CDL voltage -15 V. Nitrogen served as nebulizer gas (flow rate: 1.5 $L \cdot min^{-1}$). All analyses were performed with a Vydac C18 column (4.6 mm x 150 mm; 5µm), eluted with a linear elution gradient from 20% to 80% B over 35 minutes at a flow rate 1 $mL \cdot min^{-1}$). The running eluents were: solvent A, H_2O 0.1% TFA and solvent B, ACN 0.1% TFA. The crude peptide (CD44BP) was further purified by preparative RP-HPLC with a Vydac C18 column (22 mm x 250 cm; 10 µm), eluted with a linear gradient (solvent A, H_2O 0.1% TFA; solvent B, ACN 0.1% TFA) from 20 to 80% B over 58 minutes at flow rate of 23 $mL \cdot min^{-1}$. All analysis was performed at detection wavelength of 220 nm. The pooled fractions, containing the desired products, were lyophilized. The peptides

homogeneity was assessed by analytical HPLC and by ESI mass spectrometry. The crude Biotin-PEG_{2k}-Maleimide-peptide (CD44BP-PEG_{2k}) was purified by preparative flash chromatography, using a Biotage ISOLERA flash purification system, ISO-1SW model, equipped with a diode-array detector. The product was eluted with a linear gradient (solvent A, H_2O 0.1% TFA; solvent B, ACN 0.1% TFA) from 5 to 95% B over 25 column volumes, using SNAP C18 12g as column. The pooled fractions, containing the desired products were analyzed by analytical RP-HPLC–ESI-MS.

MALDI-TOF analysis of PEGylated peptides

PEGylated peptide was characterized by matrix-assisted laser desorption/ionization mass spectrometry coupled to two times of flight analyzers (MALDI-TOF-TOF). The sample was prepared with a final concentration of ~ 2 pmol/μL in the matrix by mixing the peptide with a solution 60% of α-cyano-4-hydroxycinnamic acid (CHCA) and 40% of 5-Dihydroxybenzoic acid (DHB).

The two matrix solutions were prepared as follows:

1. 20 mg/mL of CHCA in a solution of H_2O 5% formic acid in ACN (30/70 v/v)
2. 20 mg/mL of DHB in a solution of H_2O 0.1% TFA in ACN (30/70 v/v)

Approximately, 0.25 μL of the sample was deposited on the MALDI plate, after a layer deposition of a saturated solution of CHCA in acetone, and allowed to dry prior to analysis. The mass spectra were recorded on an AB SCIEX TOF/TOF 5800 instrument operated in the reflector positive mode. MALDI-TOF MS analyses were conducted at a laser intensity of 4287 units and laser pulse rate of 400 Hz with a set mass range of 1000 to 6000 Da. A continuous stage motion set in a random pattern at 600 μm/s was used for sampling.

Calibration was performed using Cal mix 5 from AB SCIEX as calibrants, which contained des-Arg^1-Bradykinin, Angiotensin I, Glu^1-Fibrinopeptide B, adrenocorticotropic hormone ACTH (1–17 clip), ACTH (18–39 clip) and ACTH (7–38 clip) resulting in a mass accuracy of 50 ppm. Each spectrum represents the sum of 2040 laser pulses from randomly chosen spots per sample position. Raw data were analyzed using TOF/TOF Series Explorer software provided by the manufacturer and are reported as monoisotopic masses.

Uptake of 5-FAM-CD44BP

U-87 human primary glioblastoma cells were grown in DMEM (10% FBS, 1% L-Glu, 1% Streptomycin pennicyllin) and HUVECs human umbilical vein endothelial cells were kept in M200 (20% FBS and supplemented with LGSG kit). After seeding, cells (2×10^5) were left 2 h to allow attachment. Then were incubated and treated with 5-FAM-CD44BP dissolved in DMSO (final concentration in cells 8.5 μM), for 1 hour in cell specific medium at 37°C. Cells were then washed twice with PBS. Cells were fixed for 20 minutes in 4% of paraformaldehyde PFA. Nuclei and cell shape were labeled by DRAQ5 (excitation 633 nm) and Phalloidin 555 (labels cytoskeleton), respectively. The fluorescence intensity was analyzed by Zeiss LSM 710 confocal microscope. Images were reconstructed by ImageJ.

Quantitative real-time polymerase chain reaction (q-PCR)

Total RNA was extracted from $1 \cdot 10^6$ U-87 and HepG2 cells using the EZNA TOTAL RNA KIT-RNA extract.kit ($1x10^6$ cel-10mg) 200 preps. mRNA was reverse transcripted into cDNA using the Kit RT 2 step(rand.prim.e/o PoliT) 500 rx. q-PCR was conducted in a LightCycler 480 real-time PCR system (Roche, Basel, Switzerland) using the Kit RT 2 step(rand.prim.e/o PoliT) 500 rx. Beta-actin was used as a reference mRNA control. q-PCR cycling conditions were: 95 °C for 10 min, (95 °C for 15 s, 60 °C for 30 s, 40 cycles), 95 °C for 60 s,

followed by a dissociation curve analysis. The primer sequences used for amplification of CD44S and beta-actin was: GGAGCAGCACTTCAGGAGGTTAC (forward primer) and GGAATGTGTCTTGGTCTCTGGTAGC (reverse primer). The IDEAS2.0 software was used to analyze the curve of PCR amplification and to calculate the C_t (Cycle threshold), referring to the number of cycles at which the fluorescence exceeded the threshold. The smaller the value of C_t, the higher the content of the original mRNA in the sample.

Curcumin loaded oil in water nanoemulsion

Firstly, a 20-wt % oil in water pre-emulsion was prepared. 5.8 g of lecithin Lipoid E 80 (egg lecithin powder 80-85% enriched with phosphatidyl choline and 7-9.5% content in phosphatidyl ethanolamine) were dissolved in 24 mL of soybean oil (density at 20 °C of 0.922 $g \cdot mL^{-1}$) at 60 °C using the immersion sonicator (Ultrasonic Processor VCX500 Sonic and Materials), performing runs of 10 seconds for 1 minute at 10% of sonication amplitude (microtip screwed). Then, 100 mg of curcumin were dissolved in the oil phase for 15 minutes at 60 °C during pre-emulsion preparation. Subsequently, the oil phase was added to the aqueous phase (Milli-Q water), and mixed using the immersion sonicator with runs of 10 seconds for 8 minutes at 70% of amplitude (a pulse-on and a pulse-off respectively of 10 seconds). The pre-emulsion was finally homogenized for 3 single cycles and 200 steps at a pressure of 2000 bar by a high-pressure homogenizer (110P series microfluidizer) to obtain the final nanoemulsion.

Polymers multilayer deposition onto curcumin loaded O/W NEs

Firstly, a layer of chitosan was deposited around the oil template with a final concentration of oil and chitosan of 10 wt% and 0.1 wt%, respectively. 0.1 M acetic acid solution of chitosan (0.125 wt%) was prepared with a final pH=4. Nanoemulsion 20 wt% oil was added quickly to the chitosan solution under

vigorous stirring and kept under stirring for 15 minutes to allow uniform chitosan deposition. The nanoemulsion with the first positive layer of chitosan was passed through a high-pressure valve homogenizer at 700 bars for 100 continuous steps. The next hyaluronic acid layer was prepared by aid of two syringe pumps (HARVARD APPARATUS 11 PLUS) and an ultrasonic bath (FALC INSTRUMENTS). Starting from the secondary nanoemulsion 10 wt% oil -0.1 wt% CT, a negative charged polymer layer was deposited by mixing 1:1 (v:v) of a 0.24 wt% aqueous solution of biotinylated hyaluronic acid , with the secondary nanoemulsion suspension. The two liquid phases were injected at the same flow rate (0.4 ml min^{-1}) through two polymicro flexible fused silica micrometric capillaries (inner diameter of 200 μm) interfaced at their extremities (Molex). Each drop was then collected inside a glass tube immersed in the ultrasonic bath at room temperature, 59 kHz and 100% power for 15 minutes. The NCs were characterized at each step of preparation by DLS analysis.

Nanocarrier assembly

The streptavidin solution was prepared by dissolving 1 mg in 1 ml of Milli-Q water (16,6 μM). It was added to the HA-Biotin 0.12 wt%-CT 0.05 wt%-O/W NEs 5 wt% oil, under sonication for 15 minutes and T= 20 °C, at a final concentration of 5.69 μM. In the same way the compound CD44BP-PEG_{2k}-biotin was added under sonication for 15 minutes and T= 20 °C to the streptavidin-HA-Biotin-CT-O/W NEs at a molar ratio 2:1 between CD44BP-PEG_{2k}-biotin and the streptavidin. The final concentrations were 3.2 μM and 6.4 μM for streptavidin and CD44BP respectively, while the final oil weight percentage was 2.78 wt%. The NCs were characterized at each step of preparation measuring the size and Z-potential by dynamic light scattering as described previously.

Particle size and Z-potential measurements

All nanoemulsions and their successive functionalization were characterized at each step of preparation by measuring size and polydispersity index (PdI), using Zetasizer Nano ZS device (Malvern Instruments) with a 4 mW He-Ne ion laser at the wavelength of 633 nm and a photodiode detector at an angle of 173°. All the samples were diluted to a droplet concentration of 0.025 wt% by using acetic acid 20 mM at pH 4 for monolayer, and Milli-Q water for emulsions and bilayer suspensions. The calculation of the particle size distribution was performed using a default refractive index ratio (1.59) and 5 runs for each measurement (1 run lasting 100 s), at least 3 times for each sample. A particle electrophoresis instrument (Zetasizer zs nano series ZEN 3600, Malvern Instruments Ltd., Malvern, U.K.) was used for the Z-potential determinations. Samples were diluted as for the particle size analysis. Setting 50 runs for each measurement carried out the Z-potential analysis. Samples were collected into polystyrene cuvettes and measured three times and the results presented are the averages of these measurements. Experiments were carried out at 25 °C. Zetasizer software (Malvern Instruments) was used to obtain the data. Cumulate analysis was used to give the Z-average value, hydrodynamic diameter, polydispersity index and the intensity size distribution graphs.

Colocalization analysis of streptavidin and peptide by confocal microscopy

For the colocalization analysis of CD44BP labelled with 5-carboxyfluorescein (5FAM-CD44BP) and streptavidin built onto the HA-Biotin-CT-O/W NEs; streptavidin-Atto-655 (A655-strep) was used. The sample was arranged as described before. It was diluted 1:10 in water Milli-Q and then added (15 μL) to agarose gel at 40° (low gelling temperature agarose

A9414 Sigma-Aldrich; 2.5 % w/v, 30 µL) at a volume ratio 1/2 v/v. The sample was placed on a microscope cover glass for 5 minutes to allow the gelation of the agarose. Images of the sample were captured with a Leica TCS SP5 Laser Confocal Scanning microscope (Leica-Microsystems, Mannheim, Germany) with a Plan Apo 100x/1.4 oil immersion objective. Fluorescence were detected by hybrid detectors using 488 nm Ar and 633 nm HeNe excitation laser lines in the 500-550 nm and 650-710 nm emission bands, respectively for 5FAM-CD44BP e A655-strep. Images were acquired with a field of view 38.8 x 38.8 µm, 512 x 512 pixel frame format, for a pixel size of 76 x 76 nm. Images were visualized by LAS-AF software (Leica-Microsystems, Mannheim, Germany) and analysed by its "colocalization" tool.

Cryo-TEM characterization

For the preparation of the frozen-hydrated sample the plunge freezing method was performed. Briefly a drop of 3 µL of the samples were put on a previously glow-discharged 200 mesh holey carbon grids (Ted Pella, USA) after that the grid was inserted in the chamber of a FEI Vitrobot Mark IV (FEI company, the Netherlands) at 4°C and 90% of humidity. The droplet of sample was blotted with filter paper for 1 s, (blot force 1, drain time 0,5 s) and then the grid was plunged into the liquid propane. The grid was then stored in liquid nitrogen in a grid box until it was finally transferred to a cryo-specimen 626 holder (Gatan, Inc., USA) and loaded into the cryo-transmission electron microscope for imaging. To obtain the image of the nanoparticles we used a Tecnai G2 20, a cryo-tomo transmission electron microscope (FEI company, the Netherland) equipped with LaB6 emitter (acceleration voltage of 200 kV) and recorded at with a 2 k × 2 k CCD-Eagle 2HS camera. The Frozen-hydrated sample is radiation-sensitive material so to avoid damaging; the observation was carried out in Low Dose Mode.

Cell culture

U-87 human primary glioblastoma cells were grown in DMEM (10% FBS, 1% L-Glu, 1% Streptomycin pennicyllin). Human umbilical vein endothelial cells (HUVECs) from Invitrogen were grown in Medium 200 supplemented with LSGS kit (LifeTechnologies). Cell culture were always performed at 37 °C in 5% CO_2 and 100% relative humidity (RH).

Cytotoxicity analysis

Cell viability was quantified by the PrestoBlue Assay (Invitrogen) and compared to non- treated cells, which were used as a control. Briefly, 1×10^4 U-87 cells were seeded in a 96-well and incubated for several times (30min, 1h, 2h, and 4h) with curcumin loaded CD44BP-PEG_{2k} O/W NEs and free curcumin, diluted 1:5 in medium at a final curcumin concentration of 62.8 μM. Control experiments were carried treating cells with curcumin loaded CD44BP-PEG_{2k} O/W NEs, HA coated O/W NEs and PEG_{2k}-O/W NEs for 4h at the same experimental condition described before, also for HUVECs. PrestoBlue Assay was performed according to the manufacturer's procedure, after 24 hours. Fluorescence of PrestoBlue reagent solution (excitation 535 nm) was read at 615 nm by using a spectrofluorometer (Wallac 1420 Victor2, Perkin–Elmer, USA). All experiments were performed in triplicate.

Uptake of curcumin loaded NCs

U-87 human primary glioblastoma cells and HUVECs were grown in their respective medium as described before. After seeding, cells (2×10^5) were left 2 h to allow attachment. Then were incubated and treated with curcumin loaded CD44BP-PEG_{2k} O/W NEs, HA coated O/W NEs and PEG_{2k} O/W NEs, for 4 hours in cell specific medium at 37°C. Cells were then washed twice with PBS. Cells were fixed for 20 minutes in 4% of paraformaldehyde PFA. Nuclei and cell shape were labeled by DRAQ5 (excitation 633 nm) and WGA 555

(labels cellular membrane), respectively, while for the curcumin the excitation was fixed to 488 nm and read in a range from 500 to 530 nm. The fluorescence intensity was analyzed by Zeiss LSM 710 confocal microscope. Images were reconstructed by ImageJ.

References

1. Yoo, J., Park, C., Yi, G., Lee, D. & Koo, H. Active Targeting Strategies Using Biological Ligands for Nanoparticle Drug Delivery Systems. *Cancers (Basel).* **11**, (2019).

2. Bazak, R., Houri, M., El Achy, S., Kamel, S. & Refaat, T. Cancer active targeting by nanoparticles: a comprehensive review of literature. *Journal of Cancer Research and Clinical Oncology* **141**, 769–784 (2015).

3. Koo, O. M., Rubinstein, I. & Onyuksel, H. Role of nanotechnology in targeted drug delivery and imaging: a concise review. *Nanomedicine: Nanotechnology, Biology, and Medicine* **1**, 193–212 (2005).

4. Patra, J. K. *et al.* Nano based drug delivery systems: recent developments and future prospects. *J. Nanobiotechnology* **16**, 71 (2018).

5. Comprehensive Cancer Information - National Cancer Institute. Available at: https://www.cancer.gov/.

6. Cortes-Dericks, L. & Schmid, R. A. CD44 and its ligand hyaluronan as potential biomarkers in malignant pleural mesothelioma: Evidence and perspectives. *Respir. Res.* **18**, 1–12 (2017).

7. Lesley, J., Hyman, R., English, N., Catterall, J. B. & Turner, G. A. CD44 in inflammation and metastasis. *Glycoconj. J.* **14**, 611–622 (1997).

8. Jothy, S. CD44 and its partners in metastasis. *Clinical and Experimental Metastasis* **20**, 195–201 (2003).

9. Hefler, L. A. *et al.* The prognostic value of immunohistochemically detected CD44v3 and CD44v6 expression in patients with surgically staged vulvar carcinoma. *Cancer* **94**, 125–130 (2002).

10. Makino, M. *et al.* Identification of cell binding sites in the laminin α5-chain G domain. *Exp. Cell Res.* **277**, 95–106 (2002).

11. Hibino, S. *et al.* Identification of an active site on the laminin α5 chain globular domain that binds to CD44 and inhibits malignancy. *Cancer Res.* **64**, 4810–4816 (2004).

12. Hibino, S. *et al.* Laminin α5 chain metastasis- and angiogenesis-inhibiting peptide blocks fibroblast growth factor 2 activity by binding to the heparan sulfate chains of CD44. *Cancer Res.* **65**, 10494–10501 (2005).

13. Yang, X., Sarvestani, S. K., Moeinzadeh, S., He, X. & Jabbari, E. Effect of CD44 Binding Peptide Conjugated to an Engineered Inert Matrix on Maintenance of Breast Cancer Stem Cells and Tumorsphere Formation. *PLoS One* **8**, 1–15 (2013).

14. Zaiden, M. *et al.* CD44-Targeted Polymer–Paclitaxel Conjugates to Control the Spread and Growth of Metastatic Tumors. *Mol. Pharm.* **15**, 3690–3699 (2018).

15. Lim, S. *et al.* Glioblastoma-secreted soluble CD44 activates tau pathology in the brain. *Exp. Mol. Med.* **50**, 5 (2018).

16. Nagahama, K. *et al.* Discovery of a new function of curcumin which enhances its anticancer therapeutic potency. *Sci. Rep.* **6**, (2016).

17. Bird, G. H., Crannell, W. C. & Walensky, L. D. Chemical synthesis of hydrocarbon-stapled peptides for protein interaction research and therapeutic targeting. *Curr. Protoc. Chem. Biol.* **3**, 99–117 (2011).

18. Dai, J. *et al.* Osteopontin induces angiogenesis through activation of PI3K/AKT and ERK1/2 in endothelial cells. *Oncogene* **28**, 3412–3422 (2009).

19. The Human Protein Atlas. Available at: https://www.proteinatlas.org/.

20. Bogan, M. J. & Agnes, G. R. *Poly(ethylene glycol) Doubly and Singly Cationized by Different Alkali Metal Ions: Relative Cation Affinities and Cation-Dependent Resolution in a Quadrupole Ion Trap Mass Spectrometer*. (2001).

21. Perrault, S. D. & Chan, W. C. W. In vivo assembly of nanoparticle components to improve targeted cancer imaging.

22. Erickson, H. P. Size and Shape of Protein Molecules at the Nanometer Level Determined by Sedimentation, Gel Filtration, and Electron Microscopy.

23. BOLTE, S. & CORDELIÈRES, F. P. A guided tour into subcellular colocalization analysis in light microscopy. *J. Microsc.* **224**, 213–232 (2006).

24. Tønnesen, H. H., Másson, M. & Loftsson, T. Studies of curcumin and curcuminoids. XXVII. Cyclodextrin complexation: Solubility, chemical and photochemical stability. *Int. J. Pharm.* **244**, 127–135 (2002).

25. Sigfridsson, K., Lundqvist, A. J. & Strimfors, M. Particle size reduction for

improvement of oral absorption of the poorly soluble drug UG558 in rats during early development. *Drug Dev. Ind. Pharm.* **35**, 1479–1486 (2009).

26. Ravindran, J., Prasad, S. & Aggarwal, B. B. Curcumin and Cancer Cells: How Many Ways Can Curry Kill Tumor Cells Selectively? (2009).

27. Gersey, Z. C. *et al.* Curcumin decreases malignant characteristics of glioblastoma stem cells via induction of reactive oxygen species.

28. Klinger, N. V & Mittal, S. Therapeutic Potential of Curcumin for the Treatment of Brain Tumors. (2016).

29. Cheng, C. *et al.* Curcumin induces G2/M arrest and triggers apoptosis via FoxO1 signaling in U87 human glioma cells. *Mol. Med. Rep.* **13**, 3763–3770 (2016).

30. Anuchapreeda, S., Fukumori, Y., Okonogi, S., Ichikawa, H. & Craig, M. M. Preparation of Lipid Nanoemulsions Incorporating Curcumin for Cancer Therapy. *J. Nanotechnol.* **2012**, 11 (2012).

31. Gao, Y. *et al.* Preparation, characterization, pharmacokinetics, and tissue distribution of curcumin nanosuspension with TPGS as stabilizer. *Drug Dev. Ind. Pharm.* **36**, 1225–1234 (2010).

32. Vecchione, R. *et al.* Curcumin bioavailability from oil in water nano-emulsions: In vitro and in vivo study on the dimensional, compositional and interactional dependence. *J. Control. Release* **233**, 88–100 (2016).

33. Koo, H. J. *et al.* Introduction of Methyl Groups at C2 and C6 Positions Enhances the Antiangiogenesis Activity of Curcumin. *Sci. Rep.* **5**, (2015).

34. Soltani, B., Bodaghabadi, N., Mahpour, G., Ghaemi, N. & Sadeghizadeh, M. Nanoformulation of curcumin protects HUVEC endothelial cells against ionizing radiation and suppresses their adhesion to monocytes: potential in prevention of radiation-induced atherosclerosis. *Biotechnol. Lett.* **38**, 2081–2088 (2016).

35. Coin, I., Beyermann, M. & Bienert, M. Solid-phase peptide synthesis: from standard procedures to the synthesis of difficult sequences. *Nat. Protoc.* **2**, 3247–3256 (2007).

36. BARLOS, K., GATOS, D., HATZI, O., KOCH, N. & KOUTSOGIANNI, S. Synthesis of the very acid-sensitive Fmoc-Cys(Mmt)-OH and its application in solid-phase peptide synthesis. *Int. J. Pept. Protein Res.* **47**, 148–153(2009).

CHAPTER 4: Peptide functionalization of emulsion-based nanocarrier towards Blood Brain Barrier

Introduction

Effective cancer therapy for the treatment of brain tumours and central nervous system (CNS) diseases still remains one of the most challenging areas in drug delivery research. One of the major issues is represented by their inability to cross the physical obstacle of the blood brain barrier (BBB)[1,2]. Identifying routes for non-invasive drug delivery to brain and developing targeting strategies to transport biologics into the brain represent a research area of growing importance. Although many strategies to bypass the BBB have been proposed, to date none has shown a satisfactory efficiency–safety balance. The most common strategies are focused on improving functionalized drug delivery systems (DDS) transport across endothelial cells, enhancing lipophilicity and positive charge, in order to increase passive diffusion in the some way as glucose, water and amino acids which are crucial to neural function. However, these modifications lead to higher unspecific uptake in many tissues often resulting in off-target effects. A promising strategy for overcoming the BBB to deliver biologics is the targeting of endogenous receptor-mediated transport (RMT) systems that engage vesicular trafficking to transport ligands across the BBB endothelium. If a drug delivery system is modified with an appropriate targeting ligand, it can gain improved access to the brain via RMT and release its cargo.

The transferrin receptor (TfR) was one of the first RMT systems studied for BBB drug delivery applications[3]. TfR is not only ubiquitously overexpresses on the brain capillary endothelial cells, but also has much higher expression in human glioblastoma than normal brain because it mediates iron delivery to the brain (also required for cancer cell proliferation) via binding and intracellular trafficking of the iron-binding protein transferrin (Tf)[4,5]. The use of Tf as targeting ligand has been demonstrated, but some types of nanoparticles showed to lose their specificity *in vivo*, probably because the endogenous Tf is in completion with the Tf-modified drug delivery systems to TfR, and thus induced insufficient delivery to the tumour site[6]. One approach to overcome this issue is the use of targeting moieties whose TfR recognition is mediated by a new molecular pathway. For example, recently it was discovered by selection of a phage display peptide library in vivo, a new cyclic iron-mimicking peptide, CRTIGPSVC (CRT), that is able to functionally "mimic" iron via binding to apo-Tf, causing it to adopt its iron-bound holo-Tf conformation, and thereby gain access to the brain through Tf-TfR interaction (Figure 1). This peptide exhibited promise results for use in the treatment of brain tumors through delivery of the herpes simplex virus thymidine kinase gene to a mouse model of human glioma. The delivery was accomplished via i.v. administration of a CRT-targeted adeno-associated virus and phage hybrid vector and resulted in significant tumor shrinkage[7,8].

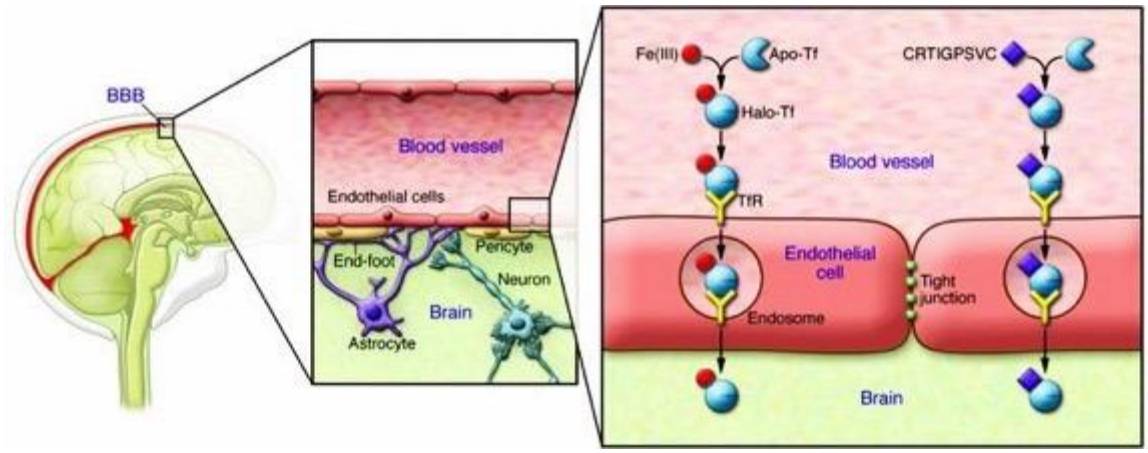

Figure 1: *Schematic representation of BBB and mechanism of CRT peptide recognition of TfR*[6].

Another example of the therapeutic prospective of CRT for the treatment of glioblastoma was provided by Jun Chen and co-workers who demonstrated a remarkably prolonged median survival when mice were treated with paclitaxel loaded CRT-NPs[9]. Besides these promising results, CRT has proven to be a promising candidate for BBB targeting. In order to develop a novel emulsion based nanocapsule (NC) able to target the BBB, CRT was integrated to the multilayer polymer coated O/W NEs described in the previous chapters. Briefly, O/W NEs were stabilized with a double layer of chitosan and biotinylated hyaluronic acid to protect the cargo and then it was functionalized with the bioactive peptide to promote the NCs accumulation on BBB, thanks to ligand-transferrin receptor recognition. The peptide was attached outside the system using an easy additive decoration strategy that exploits biotin–streptavidin physical interaction. The peptide was conjugated to a biotinylated poly(ethylene glycol) (PEG) chain in order to inhibit the NCs clearance by reticuloendothelial system (RES) and expose it to the external side. In order to verify the peptide specificity toward cells over-expressing TfR

receptor, biological tests of peptide functionalized O/W NEs were carried out. We chose a mouse brain cell line (bEnd.3) as model of endothelial brain tissue and thus the blood-brain-barrier, and paclitaxel (PTX), a well-known synthetic drug, to appreciate peptide-mediated accumulation on bEnd.3 cells by the induced cytotoxicity. Even if PTX is an anticancer drug, in this context its purpose was not for therapeutic applications, but only as harmful substance toward healthy BBB cells used in biological tests to assess NCs accumulation ability. Indeed, CRT can provide the accumulation of the carrier to brain site, but it is not able to cross it. To this aim, in future, we will need to integrate a cell penetrating peptide (discussed in Chapter 1) able to get across the brain.

Results and discussion

Synthesis, purification and characterization of CRT

Among a plethora of peptides reported to be able to recognize the TfR receptor, the most promising was a cyclic 9-mer peptide (CRT), whose sequence was CRTIGPSVC. The amino acid sequence was modified introducing a non-α-amino acid (β-alanine) at the N-tem and C-term, and a lysine at the C-term as last amino acid (βA-CRTIGPSVC-βA-K). β-alanine acts as spacer in order to retain the native peptide conformation when conjugated to the nanocapsules, while the Lys was inserted to exploit his side chain ($-NH_2$) for future functionalization (i.e. fluorophore labelling). The peptide synthesis was performed exploiting the solid-phase peptide strategy (SPPS), using 9-fluorenylmethoxycarbonyl (Fmoc) chemistry and a super acid labile resin. The resulting peptide was deprotected and cleaved from the resin. The crude peptide purity was assessed by analytical RP-LC-MS, whose chromatogram and mass spectra were reported in Figure 2. Purified CRT peptide was cyclized by dissolving it in aqueous solution containing 5% DMSO, employing the

recommended dilute concentration of the thiol moieties (0.01–0.1 mM) to allow the formation of the intra-chain disulphide bond between the two cysteine residues, avoiding dimers formation, which is a frequent side reaction during cyclization[10,11]. Unambiguous identification that peptide cyclization occurred, was accomplished through LC-MS analysis reported in Figure 3. It's possible to observe a slight shift in the retention time of non-cyclic and cyclic peptides, followed by a difference in the mass values corresponding exactly to the two protons that has been lost for the formation of cysteine disulphide bridge.

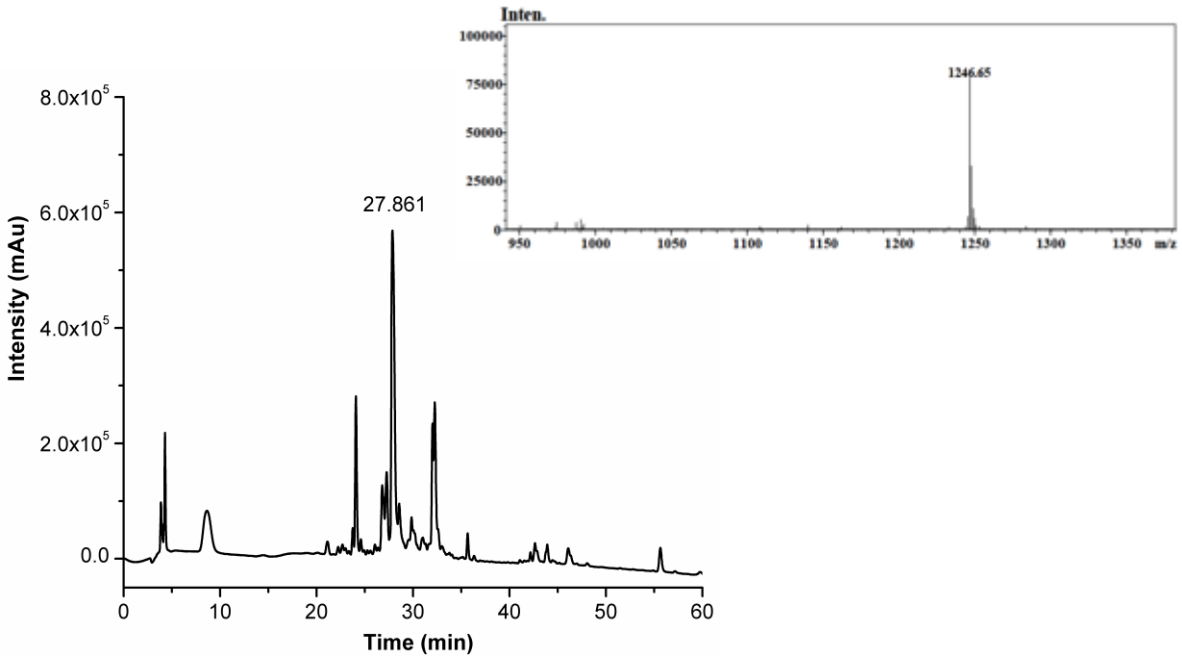

Figure 2: *RP-HPLC chromatogram of crude CRT. ESI-MS spectrum relative to the peak at R_t = 27.86 min that corresponds to $[M+H]^+$ of CRT (theoretical mass: 1246.50 Da; observed mass: 1246.65 Da).*

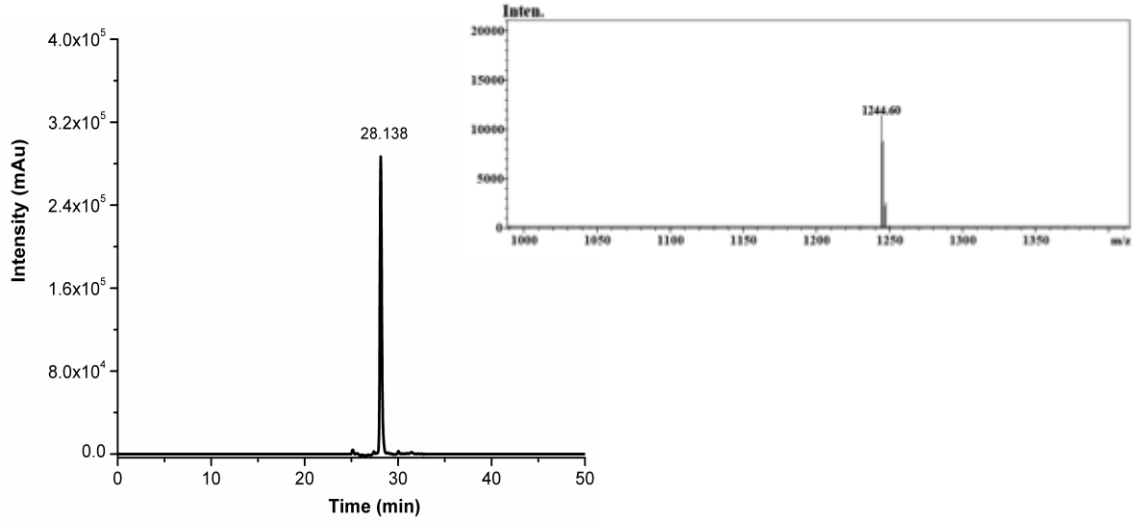

Figure 3: *RP-HPLC chromatogram of pure cyclic CRT. ESI-MS spectrum relative to the peak at R_t = 28.14 min that corresponds to $[M+H]^+$ of cyclic-CRT (theoretical mass: 1244.49 Da; observed mass: 1244.60 Da).*

In order to anchor the cyclic peptide to our nanocapsules exploiting biotin-streptavidin affinity, as largely described in the previous chapter, a peptide PEGylation was performed as schematically represented in Figure 4.

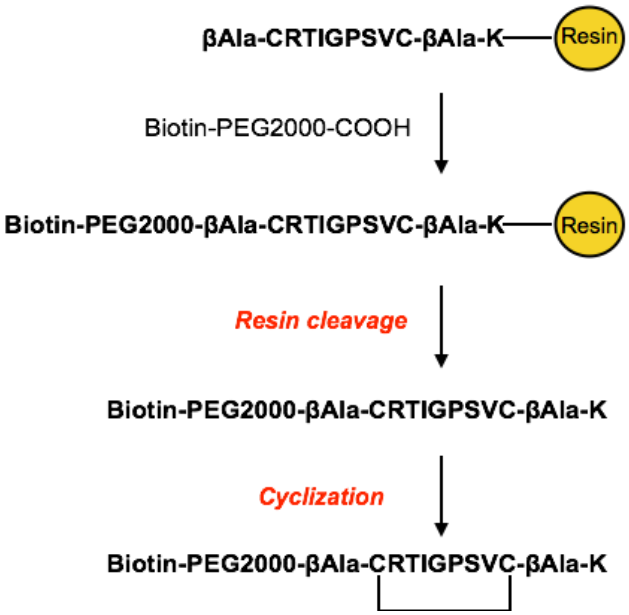

Figure 4: *Schematic representation of the solid-phase synthetic strategy of CRT peptide PEGylation.*

A biotin functionalized PEG_{2k} linker (biotin-PEG_{2k}-COOH) was conjugated at the N-term of peptide sequence, directly on the resin, via amide bond formation with carboxyl group.

The solid-phase synthesis was chosen to simplify the purification of unreacted biotin-PEG_{2k}-COOH from PEGylated peptide, performed by several wash steps after the reaction was over. Once the peptide coupling with the biotin-PEG_{2k}-COOH linker was done, it was deprotected and cleaved from the resin. The crude biotin-PEG_{2k}–CRT peptide (CRT-PEG_{2k}) was purified by preparative flash chromatography, using a Biotage ISOLERA flash purification system, obtaining the pure product with a final yield of approximately 5%. The pooled fractions, containing the desired products were analysed by analytical RP-HPLC, whose chromatogram was reported in Figure 5.

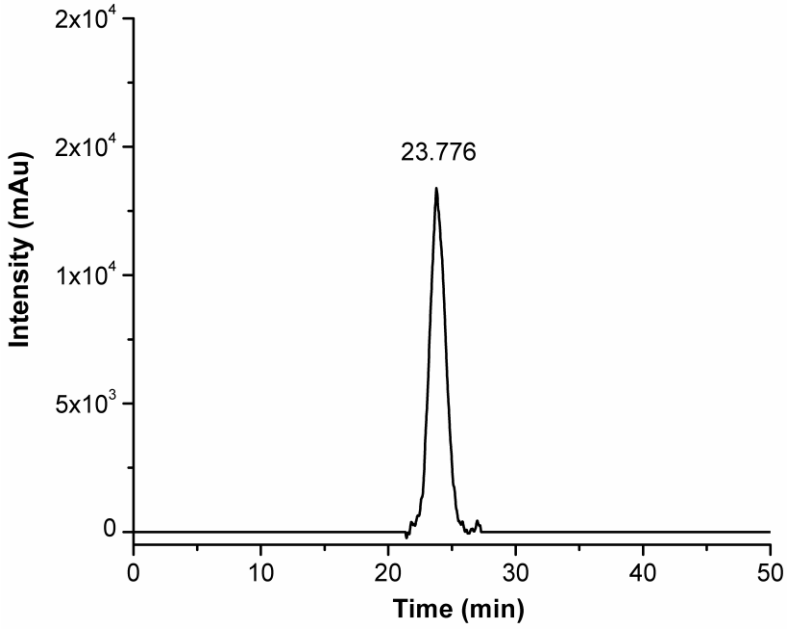

Figure 5: *Analytical RP-HPLC chromatogram of purified CRT-PEG2k, detected at λ = 220 nm.*

The recognition of the product at R_t = 23.78 min was established by matrix-assisted laser desorption/ionization mass spectrometry coupled to two time of flight analyzers (MALDI-TOF-TOF), whose mass spectrum was reported in Figure 6. The centroid mass spectrum of biotin-PEG_{2k}-COOH linker acquired before and after peptide conjugation was reported.

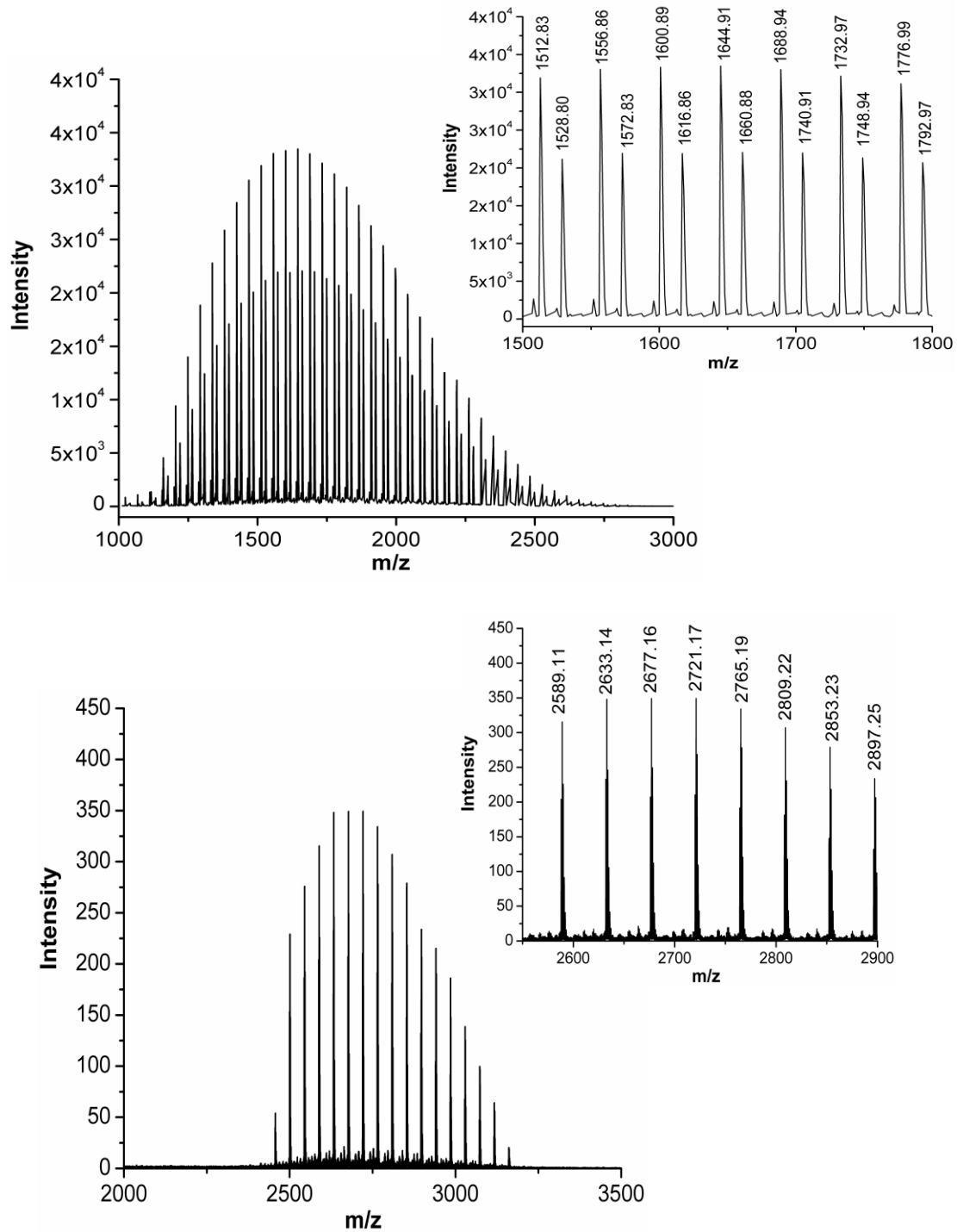

Figure 6: *MALDI mass spectra (centroid) of Biotin-PEG$_{2k}$-COOH linker on the top and CRT-PEG$_{2k}$ peptide at the bottom. On the top right-hand side of each image is reported a zoomed section.*

By making a comparison between them, the intense polydisperse Gaussian distribution and the typical expected ethylene oxide repeat units of 44 Da were observed, corroborating the presence of PEG within the samples. The increment of mass value for CRT-PEG_{2k} was an evidence that the reaction took place. Respect to the theoretical isotopic mass of CRT-PEG_{2k} (2566.22 ± 44 Da) expected, the experimental one (2589.11 ± 44 Da; reported in figure) showed an increment of +23 *m/z* due to the sodiated species $(MNa)^+$. Once the pegylated peptide was obtained, its cyclization was performed as described before.

Nanocarrier assembly

In order to build up nancapsules able to target the cerebral endothelium, the pegylated CRT peptide was linked to multi-layer O/W NEs, with the aim to exploit its recognition to transferrin receptor overexpressed on the brain endothelium. The decoration strategy used was largely discussed in the previous chapters, with the only difference that the oil core of nanoemulsions was loaded with paclitaxel. Briefly, the streptavidin was added to the HA-biotin-CT-O/W NEs under sonication, followed by addition of CRT-PEG_{2k}, characterized at all stages by DLS, whose measurements are reported in Table 1 and Figure 7. As illustrated, also in this case narrowly monodispersed functionalized nanocapsules were obtained.

Table 1: *Size, PdI and Z-potential measurement of each NCs component, loaded with paclitaxel, during the several steps of assembly. Data are reported as mean (n=3) ± SD.*

	Size (nm)	PdI	Z-potential (mV)
O/W NEs	88.81 ± 1.51	0.080 ± 0.015	-27.0 ± 4.0
CT-O/W NEs	93.25 ± 1.94	0.086 ± 0.003	+24.8 ± 1.0
HA-biotin-CT-O/W NEs	112.71 ± 8.63	0.094 ± 0.015	-31.5 ± 2.3
Streptavidin-HA-biotin-CT-O/W NEs	131.12 ± 7.08	0.145 ± 0.017	-27.9 ± 2.5
CRT-PEG$_{2k}$-Streptavidin-HA-biotin-CT-O/W NEs	137.50 ± 7.35	0.152 ± 0.002	-30.3 ± 0.1
PEG-Streptavidin-HA-biotin CT-O/W NEs	137.85 ± 4.74	0.139 ± 0.002	-30.3 ± 0.6

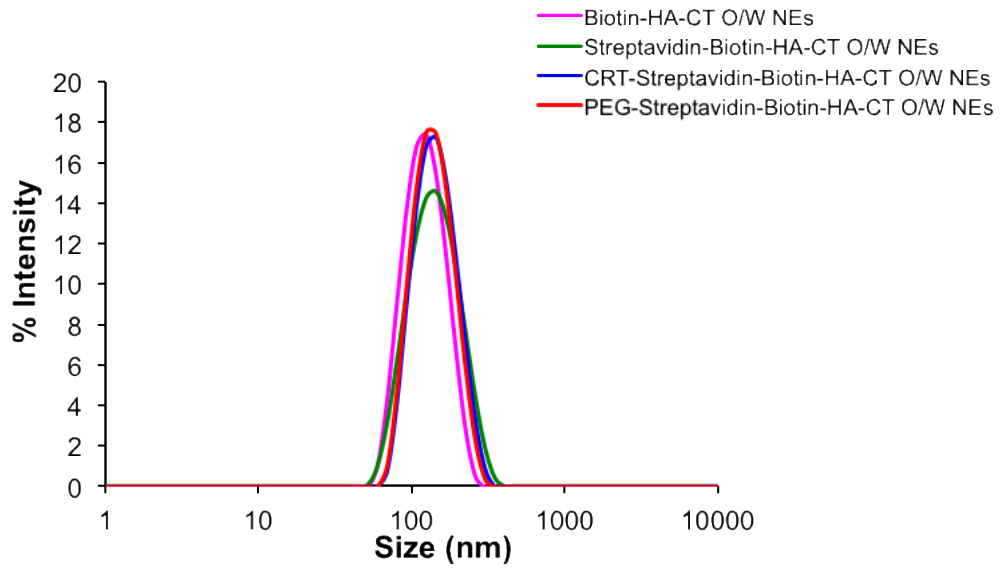

Figure 7: *Overlapping of mean hydrodynamic size of each component deposited around O/W NEs.*

The morphological characterization of the paclitaxel-loaded nanocapsule was performed by cryo-TEM analysis, as reported in Figure 8. They clearly show a homogeneous sample fixed in its frozen hydrated state confirming the size distribution observed by DLS. The image displays a well-defined electron-dense core, corresponding to the PTX loaded in the oil core that makes it difficult to observe the polymer layers around the O/W NEs.

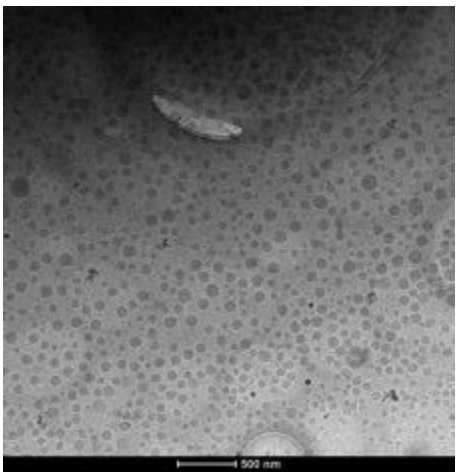

Figure 8: *Cryo-TEM projection image of paclitaxel loaded HA-CT-O/W NEs. Scale bar was 500 nm.*

Overall, DLS periodical measurements were performed to evaluate the size evolution over time. Figure 9 shows that the hydrodynamic diameter of CRT-streptavidin-HA-biotin-CT-O/W NE is quite stable within the one month temporal detection window.

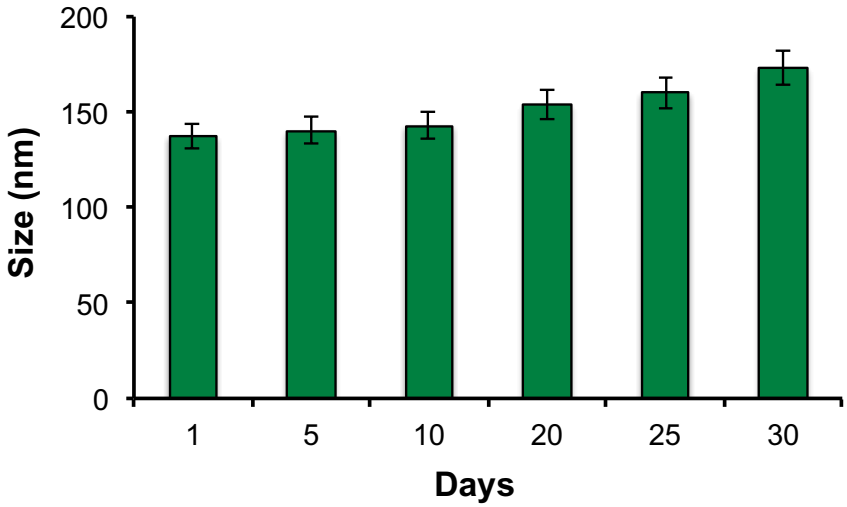

Figure 9: *Dimensional behaviour over time for PTX loaded CRT-streptavidin-HA-biotin-CT O/W NEs measured by DLS analysis.*

Preliminary biological tests

bEnd.3 cells are an immortalized mouse brain endothelial cell line, that represent an attractive candidate as model of the BBB due to their rapid growth, maintenance of BBB characteristics and formation of functional barriers[12]. It was demonstrated in our group, that the number of TfRs per bEnd3 cells was 100-fold higher than in HUVEC cells, confirming a high value expression of TfRs[13]. In order to understand the best conditions to appreciate the selective activity of CRT-PEG_{2k}-O/W NEs toward bEnd.3 cells, thanks to CRT-TfRs interaction, we investigated the PTX effect on this cell line using the same procedure of Falanga *et al.*[14].

A confluent monolayer of bEnd.3 cells were incubated with PTX loaded CRT-PEG_{2k}-O/W NEs, diluted 1:5 in cells, at a final PTX concentration of 1.4 μM for several times (30 min, 2h and 4h). Moreover, cells were treated with cell medium alone as positive control, free PTX as negative control and un-functionalized PEG_{2k}-O/W NEs that act as blank. After incubation, the cells

were washed and a quantitative evaluation of cell viability (normalized to positive control, which is set to 100%) was obtained by PrestoBlue® assay after 48 hours (Figure 10).

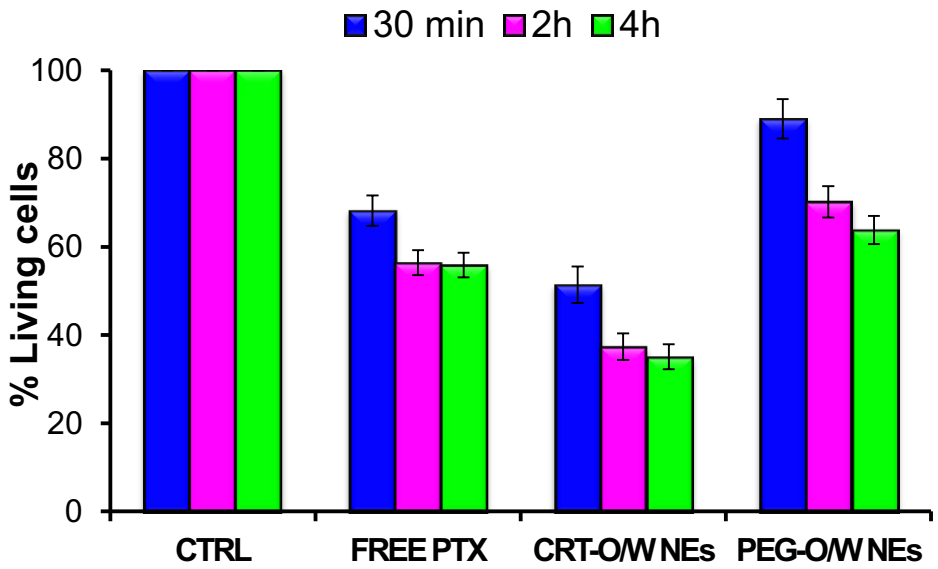

Figure 10: *Cytotoxicity assay of PTX loaded CRT-PEG$_{2k}$-O/W NEs and PEG$_{2k}$-O/W NEs, and free PTX. bEnd.3 cells were treated for several incubation times (30 min, 2h and 4h) and cell viability was evaluated after 48 h. Data are reported as mean of three independent experiment (n=3 ±SD) and expressed as percentage compared to control cells. The asterisk (*) indicates the statistical significance vs CTRL using Student's t test; (***) p ≤ 0.001.*

Data have shown an increase of cell mortality both for free PTX and for CRT-PEG$_{2k}$ O/W NEs over time, with no significant difference between two and four hours. Very interestingly, it was possible to observe a significant cytotoxicity effect of CRT-PEG$_{2k}$ O/W NEs compared to blank (PEG$_{2k}$ O/W NEs). This is an evident consequence of peptide capability to accumulate the nanocarrier on the cells surface, and allow its internalization, thanks to ligand-receptor recognition. Best results were obtained at 30 minutes of incubation for which CRT-PEG$_{2k}$ O/W NEs exhibit an increase of 38% of cell death respect to PEG$_{2k}$ O/W NEs and almost 17% respect to free PTX. Making an average over all the

times, respect to un-functionalized PEG_{2k}-O/W NEs, CRT-PEG_{2k}-O/W NEs induced an increased cells death of 33.05 ± 4.42 %.

To better understand these preliminary results, cellular uptake assays by confocal microscopy was performed. A confluent monolayer of bEnd.3 cells were incubated with CRT-PEG_{2k} O/W NEs and PEG_{2k} O/W NEs, for 4 h at the same experimental condition of cytotoxicity test described before. Rhodaminated streptavidin was used during the nanocapsules assembling to detect their fluorescence. In addition, the control (CTRL) consisted in cells treated with cell medium alone. Figure 11 shows confocal microscopic images of bEnd.3 cell monolayer after NCs uptakes, which shed light on the previous cytotoxicity results. The presence of functionalized nanocapsules was shown in red, while the cells cytoplasm and the nuclei were in green and blue respectively. In Figure 12 is reported the plot of rhodaminated-NCs 'mean' fluorescence intensity normalized for the bEnd.3 cell number.

The uptake data are in accordance with the previous cytotoxicity results by showing a clear fluorescence difference between CRT-PEG_{2k} O/W NEs and PEG_{2k} O/W NEs. However, no fluorescence can be detected from the images of the control cells. Indeed the fluorescence intensity of peptide functionalized NCs was 41.5 ± 24 % more respect to the negative control. As well as in the chapter 3, we have demonstrated the peptide capability to induce a higher internalization of functionalized NCs thanks to ligand-receptor interaction. Furthermore, a slight amount of PEG_{2k} O/W NEs was detected in the cells.

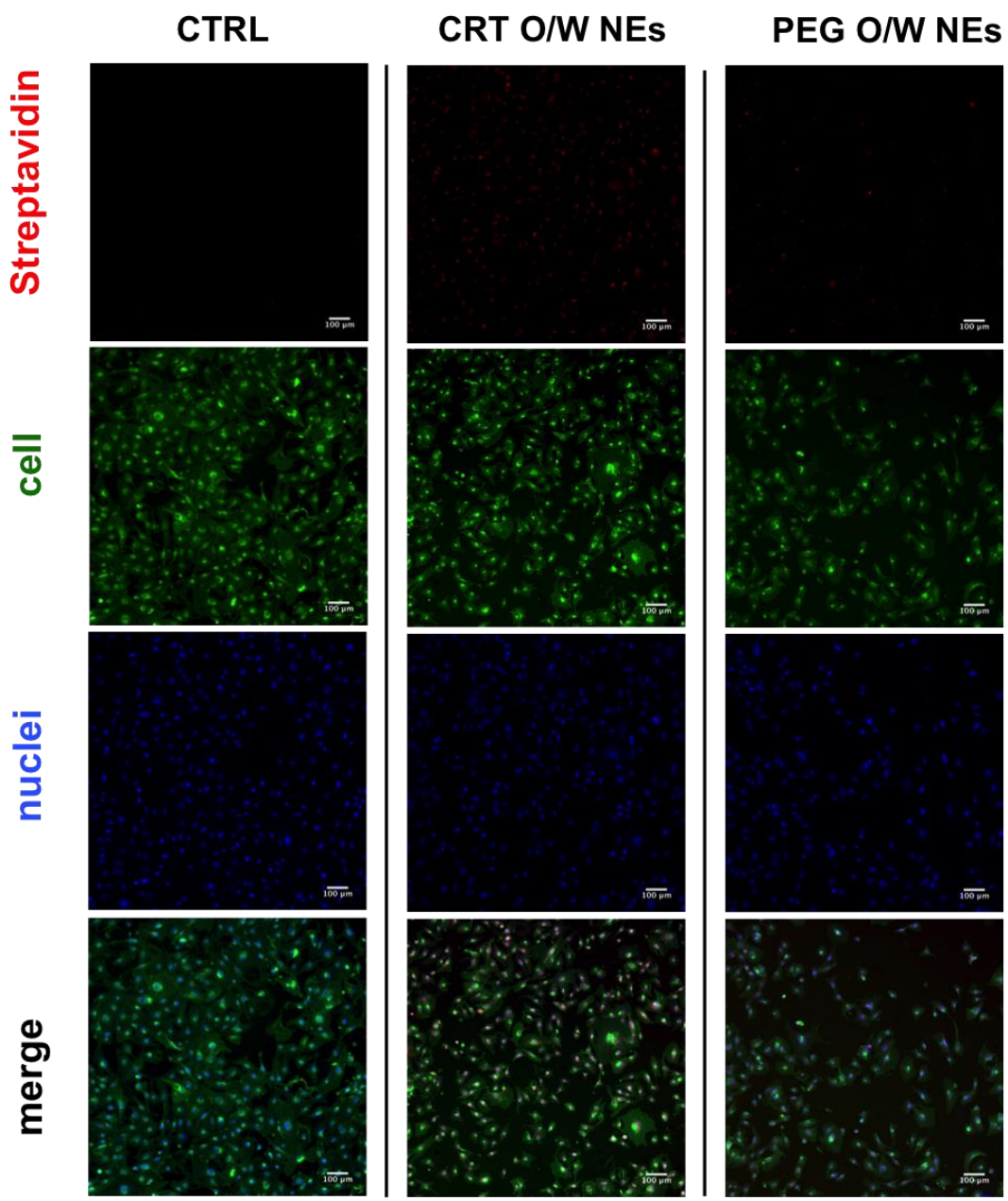

Figure 11: *Confocal images of bEnd.3 cell. Untreated, rhodaminated CRT-PEG$_{2k}$ O/W NEs and PEG$_{2k}$ O/W NEs interactions with a confluent monolayer of bEnd.3 cells. Nuclei (blue) and cellular membrane (green) of the cells were stained with DAPI and WGA 555 respectively, while red color represents rhodamine uptake. Scale bar is 100 µm.*

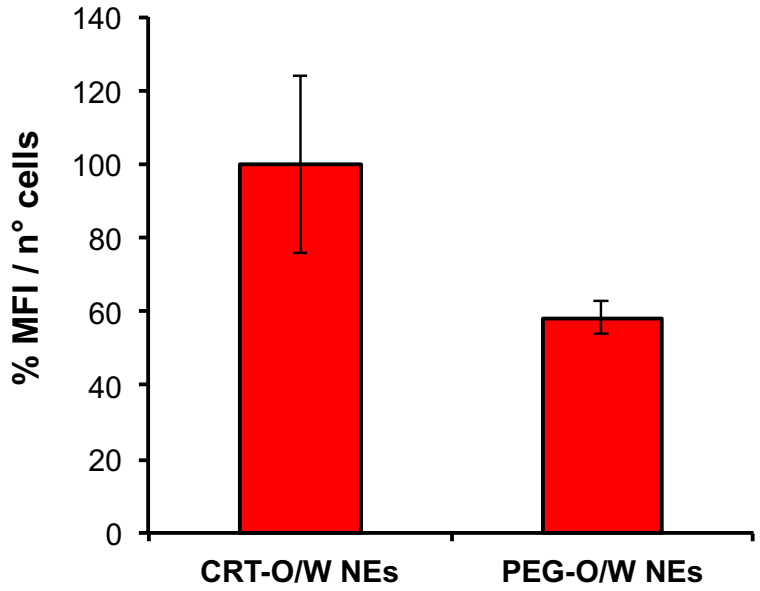

Figure 12: *Plot of mean fluorescence intensity of rhodaminated nanocapsules normalized to cells number. bEnd.3 cells were treated with CRT-PEG$_{2k}$ O/W NEs and PEG$_{2k}$ O/W NEs . Data are reported as mean (n=3) ± SD.*

Conclusions

The aim of this work was to characterize and demonstrate the versatility of our engineered layer by layer nanocapsules for active targeting. In order to develop a novel emulsion based nanocapsule (NC) able to target the BBB, we integrated a new peptide reported to be able to recognize and cross the BBB cells thanks to transferrin/transferrin receptor mechanism. We stabilized O/W NEs with a double layer of chitosan and biotinylated hyaluronic acid and then we functionalized the outer layer with the bioactive peptide thanks to our additive strategy, without purification steps, to promote the NCs accumulation on BBB, thanks to ligand-transferrin receptor recognition. Notwithstanding we attached a new peptide than that described in the previous chapter, the functionalized NCs keep a narrow distributed hydrodynamic diameter below 150 nm, stable over time. Preliminary biologic tests were carried out using mouse brain cell line (bEnd.3) as model of endothelial brain tissue and thus the blood-brain-barrier, and paclitaxel (PTX) as toxic drug. The cytotoxic results showed an increased cellular death of 33.05 ± 4.42 % for CRT-PEG_{2k}-O/W NEs compared to PEG_{2k}-O/W NEs that act as blank; while the uptake of CRT-PEG_{2k}-O/W NEs was 41.5 ± 24 % more respect to the negative control. In conclusion, we demonstrated the ability of CRT peptide to target the brain endothelium when conjugated to our nanocarrier, completely made of FDA-approved materials, thus paving the way to the design of novel multifunctional nanocarriers for delivery of therapeutic agents to the central nervous systems (CNS). Further development will concern the integration of a cell penetrating peptide, like gH625, able to cross the BBB. In addition, for anticancer therapeutic purposes, curcumin will substitute the use of PTX that in our case was used only as toxic molecule to test NCs accumulation ability. Curcumin not only has been demonstrated to be a good anticancer substance, but also it was

specific for tumor cells. Therefore, it is an ideal candidate for blood-brain-barrier treatments, because, although a fraction of NCs will break and release curcumin in the endothelial cells instead of crossing them, such a molecule has no activity toward these cells, avoiding side effect to healthy sites.

Materials and methods

Materials

Soybean oil and surfactant Lipoid E80 (egg lecithin powder 80-85% enriched with phosphatidylcholine and 7–9.5% content in phosphatidylethanolamine) were purchased from Lipoid GmbH and used without further purification. For preparation of all nanoemulsions and solutions, Millipore Milli-Q water was used. Chitosan (CT, LMW 90-150 kDa, DDA 84% determined via 1H-NMR), 1-hydroxybenzotriazole hydrate (HOBt), N,N′-Diisopropylcarbodiimide (DIC), N,N-Diisopropylethylamine (DIEA), trifluoroacetic acid (TFA), dimethyl sulfoxide (DMSO), dichloromethane (DCM), anhydrous N,N-dimethyl-formamide (DMF), 1,2-Ethanedithiol (EDT), Triisopropylsilane (TIS) piperidine acetone, diethyl ether, dimethyl sulfoxide (DMSO), were purchased from Sigma Aldrich. Hyaluronic acid 250 kDa and biotin-PEG_{2k}-maleimide were purchased from Creative PEGWorks. N-α-Fmoc amino acids were provided by NovaBiochem. Paclitaxel was purchased from Discovery Fine Chemicals Ltd.

Peptide synthesis and purification

CRT (βA-CRTIGPSVC-βA-K) peptide were synthesized using the standard solid-phase-9-fluorenyl methoxy carbonyl (Fmoc) procedure and were obtained with good overall yields (50-60%). The syntheses were performed by using the Biotage®Syro WaveTM peptide synthesizer (Biotage, Uppsala, The Netherlands). The peptide scale synthesis was 0.1 mmol. It was assembled on Rink Amide resin with a substitution level of 0.71 mmol/g. The following protected amino acids were used to synthesize the peptide:

Fmoc-Lys(Boc)-OH; Fmoc-Ile-OH; Fmoc-Gly-OH; Fmoc- Ser(tBu)-OH; Fmoc-Arg(Pbf)-OH; Fmoc-Pro-OH; Fmoc-Cys(Trt)-OH; Fmoc-Ala-OH; Fmoc-

Thr(tBu)-OH; Fmoc-Val-OH

The synthetic procedure can be summarized as follow:

1. Deprotection: Fmoc group was removed at the beginning of cycle with a 40% piperidine solution in DMF. After deprotection, the resin was washed with DMF to remove the residual piperidine. The peptide resin was then ready for coupling.
2. Activation: the carboxyl group of each Fmoc-amino acid was activated by addition of HBTU (2 eq.)/Oxima Pure (2 eq.)/ DIEA (4 eq.).
3. Coupling: the pre-activated Fmoc-amino acid reacted with the free amino-terminal group of the growing peptide chain on the resin using DMF as the reaction solvent
4. Capping: this reaction was performed after each coupling step, using a solution of Ac_2O 20% and DIEA 5% in DMF. Capping cycle was introduced to prevent deletion byproducts.

Deprotection, coupling and capping steps were repeated with each subsequent amino acid, until the chain assembly was completed. When the coupling was complete, the resin was washed with DMF. At completion of the synthesis, the resin was washed several times with DMF and finally dried. The peptide was cleaved from the resin by treating with 94% TFA/2.5% EDT/2.5% water/1% TIS for 2 hours at room temperature. The mixture was then concentrated and transferred to glass centrifugal tubes for compound precipitation using ice-cold diethyl ether, which was performed repeatedly. Purified CRT peptide was obtained by preparative RP-HPLC with a Vydac C18 column (22 mm x 250 cm; 10 µm), eluted with a linear gradient (solvent A, H_2O 0.1% TFA; solvent B, ACN 0.1% TFA) from 20 to 70% B over 58 minutes at flow rate of 23 $mL \cdot min^{-1}$. All analysis was performed at detection wavelength of 220 nm. Peptides were

lyophilized and then characterized using ESI-LC-MS. These analyses were carried out by injecting aqueous solutions of peptides into a Shimadzu LC-MS-2010EV system with ESI interface and Shimadzu LC-MS solution Workstation software for the data processing. A Q-array-octapole-quadrupole mass analyzer was used as the detector. Argon was used as ion gas in the CID cell and data were analyzed by Shimadzu LC-MS solution Workstation software. All analyses were performed with a Vydac C18 column (4.6 mm x 150 mm; 5μm), eluted with a linear elution gradient from 20% to 70% B over 35 minutes at a flow rate 1 $mL \cdot min^{-1}$). The running eluents were: solvent A, H_2O 0.1% TFA and solvent B, ACN 0.1% TFA.

Peptide Cyclization

CRT peptide was dissolved in an aqueous solution at a concentration of 0.1 mM. Then, DMSO was added dropwise until its final concentration was 5%. The reaction mixture was kept open to atmosphere under vigorous magnetic stirring over-night. The product was monitored by LC-MS analysis. When the reaction was completed, the water was evaporated; the peptide was precipitated in cold ethyl acetate and lyophilized.

Biotin-PEG_{2k}-COOH peptide conjugation

The peptide was conjugated at the N-term with Biotin-PEG_{2k}-COOH directly on the resin. Firsly, Fmoc protecting group was removed with a 20% piperidine solution in DMF, followed by several washing steps. Then, the coupling reaction with Biotin-PEG_{2k}-COOH was conducted directly on the resin with DIC/HOBt/DIEA (1:1:2) 0.1 M; using DMF as solvent, overnight under nitrogen flow. At completion of the synthesis, the resin was washed several times with DMF, NMP, DCM, isopropanol and methanol, and finally dried. Biotin-PEG_{2k}-peptide was cleaved from the resin by treating with 94% TFA/2.5%

EDT/2.5% water/1% TIS for 2 hours, precipitated in ice-cold diethyl ether and lyophilized.

Peptides analysis and purification

The identity of crude peptides was analyzed by analytical RP-HPLC–ESI-MS. The LC-MS was performed with a Shimadzu LC-10ADvp equipped with an SPDM10Avp diode-array detector. ESI-MS spectra were recorded on a Shimadzu LC-MS-2010EV system with ESI interface and Shimadzu LC-MS solution Workstation software for the data processing. A Q-array-octapole-quadrupole mass analyzer was used as the detector. Argon was used as ion gas in the CID cell and data were analyzed by Shimadzu LC-MS solution Workstation software. The optimized MS parameters were selected as followed: curved desolvation line (CDL) temperature 200°C; block temperature 200°C; probe temperature 200°C; detector gain 1.6 kV; probe voltage +4.5 kV; CDL voltage -15 V. Nitrogen served as nebulizer gas (flow rate: 1.5 L·min^{-1}). All analyses were performed with a Vydac C18 column (4.6 mm x 150 mm; 5µm), eluted with a linear elution gradient from 1% to 70% B over 35 minutes at a flow rate 1 mL·min^{-1}). The running eluents were: solvent A, H_2O 0.1% TFA and solvent B, ACN 0.1% TFA.

The crude non cyclic peptide was further purified by preparative RP-HPLC with a Vydac C18 column (22 mm x 250 cm; 10 µm), eluted with a linear gradient (solvent A, H_2O 0.1% TFA; solvent B, ACN 0.1% TFA) from 20 to 80% B over 58 minutes at flow rate of 23 mL·min^{-1}. All analysis was performed at detection wavelength of 220 nm. The pooled fractions, containing the desired products, were lyophilized. The peptides homogeneity was assessed by analytical HPLC and by ESI mass spectrometry. The crude Biotin-PEG_{2k}-peptide was purified by preparative flash chromatography, using a Biotage ISOLERA flash purification system, ISO-1SW model, equipped with a diode-

array detector. The product was eluted with a linear gradient (solvent A, H_2O 0.1% TFA; solvent B, ACN 0.1% TFA) from 0% to 95% B over 20 column volumes, using SNAP C18 12g as column. The pooled fractions, containing the desired products were analyzed by analytical RP-HPLC–ESI-MS.

MALDI-TOF analysis of PEGylated peptides

PEGylated peptide was characterized by matrix-assisted laser desorption/ionization mass spectrometry coupled to two times of flight analyzers (MALDI-TOF-TOF). The sample was prepared with a final concentration of ~ 2 pmol/μL in the matrix by mixing the peptide with a solution 60% of α-cyano-4-hydroxycinnamic acid (CHCA) and 40% of 5-Dihydroxybenzoic acid (DHB).

The two matrix solutions were prepared as follows:

1. 20 mg/mL of CHCA in a solution of H_2O 5% formic acid in ACN (30/70 v/v)
2. 20 mg/mL of DHB in a solution of H_2O 0.1% TFA in ACN (30/70 v/v)

Approximately, 0.25 μL of the sample was deposited on the MALDI plate, after a layer deposition of a saturated solution of CHCA in acetone, and allowed to dry prior to analysis. The mass spectra were recorded on an AB SCIEX TOF/TOF 5800 instrument operated in the reflector positive mode. MALDI-TOF MS analyses were conducted at a laser intensity of 4287 units and laser pulse rate of 400 Hz with a set mass range of 1000 to 6000 Da. A continuous stage motion set in a random pattern at 600 μm/s was used for sampling. Calibration was performed using Cal mix 5 from AB SCIEX as calibrants, which contained des-Arg^1-Bradykinin, Angiotensin I, Glu^1-Fibrinopeptide B, adrenocorticotropic hormone ACTH (1–17 clip), ACTH (18–39 clip) and ACTH (7–38 clip) resulting in a mass accuracy of 50 ppm. Each spectrum represents the sum of 2040 laser pulses from randomly chosen spots per sample position.

Raw data were analyzed using TOF/TOF Series Explorer software provided by the manufacturer and are reported as monoisotopic masses.

Paclitaxel loaded oil in water nanoemulsion

Firstly, a 20-wt % oil in water pre-emulsion was prepared. 5.8 g of lecithin Lipoid E 80 (egg lecithin powder 80-85% enriched with phosphatidyl choline and 7-9.5% content in phosphatidyl ethanolamine) were dissolved in 24 mL of soybean oil (density at 20 °C of 0.922 $g \cdot mL^{-1}$) at 60 °C using the immersion sonicator (Ultrasonic Processor VCX500 Sonic and Materials), performing runs of 10 seconds for 1 minute at 10% of sonication amplitude (microtip screwed). Then, 1 mL of ethanol solution of PTX (5 mg/mL) was added to the oil phase and kept for 1 hours at 70 °C to evaporate the ethanol. Subsequently, the oil phase was added to the aqueous phase (Milli-Q water), and mixed using the immersion sonicator with runs of 10 seconds for 8 minutes at 70% of amplitude (a pulse-on and a pulse-off respectively of 10 seconds). The pre-emulsion was finally homogenized for 3 single cycles and 200 steps at a pressure of 2000 bar by a high-pressure homogenizer (110P series microfluidizer) to obtain the final nanoemulsion.

Polymers multilayer deposition above paclitaxel loaded O/W NEs

Firstly, a layer of chitosan was deposited around the oil template with a final concentration of oil and chitosan of 10 wt% and 0.1 wt%, respectively. 0.1 M acetic acid solution of chitosan (0.125 wt%) was prepared with a final pH=4. Nanoemulsion 20 wt% oil was added quickly to the chitosan solution under vigorous stirring and kept under stirring for 15 minutes to allow uniform chitosan deposition. The nanoemulsion with the first positive layer of chitosan was passed through a high-pressure valve homogenizer at 700 bars for 100 continuous steps. The next hyaluronic acid layer was prepared by aid of two syringe pumps (HARVARD APPARATUS 11 PLUS) and an ultrasonic bath

(FALC INSTRUMENTS). Starting from the secondary nanoemulsion 10 wt% oil - 0.1 wt% CT, a negative charged polymer layer was deposited by mixing 1:1 (v:v) of a 0.24 wt% aqueous solution of biotinylated hyaluronic acid, with the secondary nanoemulsion suspension. The two liquid phases were injected at the same flow rate (0.4 mL min^{-1}) through two polymicro flexible fused silica micrometric capillaries (inner diameter of 200 μm) interfaced at their extremities (Molex). Each drop was then collected inside a glass tube immersed in the ultrasonic bath at room temperature, 59 kHz and 100% power for 15 minutes. The NCs were characterized at each step of preparation by DLS analysis.

Nanocarrier assembly

The streptavidin solution was prepared by dissolving 1 mg in 1 mL of Milli-Q water (16,6 μM). It was added to the HA-Biotin 0.12 wt%-CT 0.05 wt%-O/W NEs 5 wt% oil, under sonication for 15 minutes and T= 20 °C, at a final concentration of 5.69 μM. In the same way the compound CRT-PEG_{2k}-biotin was added under sonication for 15 minutes and T= 20 °C to the streptavidin-HA-Biotin-CT-O/W NEs at a molar ratio 2:1 between CRT-PEG_{2k}-biotin and the streptavidin. The final concentrations were 3.2 μM and 6.4 μM for streptavidin and CRT respectively, while the final oil weight percentage was 2.78 wt%. The NCs were characterized at each step of preparation measuring the size and Z-potential by dynamic light scattering as described previously.

Particle size and Z-potential measurements

All nanoemulsions and their successive functionalization were characterized at each step of preparation by measuring size and polydispersity index (PdI), using Zetasizer Nano ZS device (Malvern Instruments) with a 4 mW He-Ne ion laser at the wavelength of 633 nm and a photodiode detector at an angle of 173°. All the samples were diluted to a droplet concentration of 0.025 wt% by

using acetic acid 20 mM at pH 4 for monolayer, and Milli-Q water for emulsions and bilayer suspensions. The calculation of the particle size distribution was performed using a default refractive index ratio (1.59) and 5 runs for each measurement (1 run lasting 100 s), at least 3 times for each sample. A particle electrophoresis instrument (Zetasizer zs nano series ZEN 3600, Malvern Instruments Ltd., Malvern, U.K.) was used for the Z-potential determinations. Samples were diluted as for the particle size analysis. Setting 50 runs for each measurement carried out the Z-potential analysis. Samples were collected into polystyrene cuvettes and measured three times and the results presented are the averages of these measurements. Experiments were carried out at 25 °C. Zetasizer software (Malvern Instruments) was used to obtain the data. Cumulate analysis was used to give the Z-average value, hydrodynamic diameter, polydispersity index and the intensity size distribution graphs.

Cryo-TEM Characterization

For the preparation of the frozen-hydrated sample the plunge freezing method was performed. Briefly a drop of 3 μL of the samples were put on a previously glow-discharged 200 mesh holey carbon grids (Ted Pella, USA) after that the grid was inserted in the chamber of a FEI Vitrobot Mark IV (FEI company, the Netherlands) at 4°C and 90% of humidity. The droplet of sample was blotted with filter paper for 1 s, (blot force 1, drain time 0,5 s) and then the grid was plunged into the liquid propane. The grid was then stored in liquid nitrogen in a grid box until it was finally transferred to a cryo-specimen 626 holder (Gatan, Inc., USA) and loaded into the cryo-transmission electron microscope for imaging. To obtain the image of the nanoparticles we used a Tecnai G2 20, a cryo-tomo transmission electron microscope (FEI company, the Netherland) equipped with LaB6 emitter (acceleration voltage of 200 kV) and recorded at

with a 2 k × 2 k CCD-Eagle 2HS camera. The Frozen-hydrated sample is radiation-sensitive material, so to avoid damaging; the observation was carried out in Low Dose Mode.

Cell culture

bEnd.3 cells were grown in DMEM (10% FBS, 1% L-Glu, 1% Streptomycin pennicyllin). Cell culture were always performed at 37 °C in 5% CO_2 and 100% relative humidity (RH). Cells were used from passages 23 to 30.

Cytotoxicity analysis

Cell viability was quantified by the PrestoBlue Assay (Invitrogen) and compared to non- treated cells, which were used as a control. Briefly, 1×10^4 bEnd.3 cells were seeded in a 96-well and incubated for several times (30min, 2h, and 4h) with PTX loaded CRT-PEG_{2k} O/W NEs, PEG_{2k} -O/W NEs and free PTX, diluted 1:5 in cells, at a final PTX concentration of 1.4 µM. PrestoBlue Assay was performed according to the manufacturer's procedure, after 24 hours. Fluorescence of PrestoBlue reagent solution (excitation 535 nm) was read at 615 nm by using a spectrofluorometer (Wallac 1420 Victor2, Perkin–Elmer, USA). All experiments were performed in triplicate.

Uptake of PTX loaded NCs

bEnd.3 cells were grown in DMEM (10% FBS, 1% L-Glu, 1% Streptomycin pennicyllin). After seeding, cells (1×10^4) were left overnight to allow attachment. Then were incubated and treated with PTX loaded CRT-PEG_{2k} O/W NEs and PEG_{2k}-O/W NEs (using rhodaminated streptavidin during NCs assembly) for 4 hours in cell specific medium at 37°C. Cells were then washed twice with PBS. Cells were fixed for 20 minutes in 4% of paraformaldehyde PFA. Nuclei and cell shape were labeled by DRAQ5 (excitation 633 nm) and WGA 555 (labels cellular membrane), respectively. The fluorescence intensity

was analyzed by Zeiss LSM 700 confocal microscope. Images were reconstructed by ImageJ.

References

1. Pardridge, W. M. Drug Transport across the Blood–Brain Barrier. *J. Cereb. Blood Flow Metab.* **32**, 1959–1972 (2012).

2. Oller-Salvia, B., Sánchez-Navarro, M., Giralt, E. & Teixidó, M. Blood-brain barrier shuttle peptides: An emerging paradigm for brain delivery. *Chemical Society Reviews* **45**, 4690–4707 (2016).

3. Friden, P. M. *et al.* Anti-transferrin receptor antibody and antibody-drug conjugates cross the blood-brain barrier. *Proc. Natl. Acad. Sci. U. S. A.* **88**, 4771–4775 (1991).

4. Recht, L., Torres, C. O., Smith, T. W., Raso, V. & Griffin, T. W. Transferrin receptor in normal and neoplastic brain tissue: Implications for brain-tumor immunotherapy. *J. Neurosurg.* **72**, 941–945 (1990).

5. Gomme, P. T. & McCann, K. B. Transferrin: Structure, function and potential therapeutic actions. *Drug Discovery Today* **10**, 267–273 (2005).

6. Salvati, A. *et al.* Transferrin-functionalized nanoparticles lose their targeting capabilities when a biomolecule corona adsorbs on the surface. *Nat. Nanotechnol.* **8**, 137–143 (2013).

7. Staquicini, F. I. *et al.* Systemic combinatorial peptide selection yields a non-canonical iron-mimicry mechanism for targeting tumors in a mouse model of human glioblastoma. *J. Clin. Invest.* **121**, 161–173 (2011).

8. Hajitou, A. *et al.* A Hybrid Vector for Ligand-Directed Tumor Targeting and Molecular Imaging. *Cell* **125**, 385–398 (2006).

9. Kang, T. *et al.* Enhancing Glioblastoma-Specific Penetration by Functionalization of Nanoparticles with an Iron-Mimic Peptide Targeting Transferrin/Transferrin Receptor Complex. *Mol. Pharm.* **12**, 2947–2961 (2015).

10. CHAN, W. C. & WHITE, P. D. Fmoc Solid Phase Peptide Synthesis: A Practical Approach. *Oxford Univ. Press* 1–341 (2000).

11. Chen, L., Annis, I. & Barany, G. Disulfide Bond Formation in Peptides. *Curr. Protoc. Protein Sci.* **23**, (2001).

12. Brown, R. C., Morris, A. P. & O'Neil, R. G. Tight junction protein expression and barrier properties of immortalized mouse brain microvessel endothelial cells. *Brain Res.* **1130**, 17–30 (2007).

13. Fotticchia, I. *et al.* Energetics of ligand-receptor binding affinity on endothelial cells: An in vitro model. *Colloids Surfaces B Biointerfaces* **144**, 250–256 (2016).

14. Falanga, A. *et al.* Design, Synthesis and Characterization of Novel Co-Polymers Decorated with Peptides for the Selective Nanoparticle Transport across the Cerebral Endothelium. *Molecules* **23**, 1655 (2018).

CHAPTER 5: Coenzyme Q_{10}: cardioprotection and hepatoprotection properties of nanocarriers during exposure to doxorubicin and trastuzumab for the management of HER2+ breast cancer

Abstract

Coenzyme Q_{10} (CoQ_{10}), is a well-known antioxidant and anti-inflammatory agent with cardioprotective properties. However, clinical trials based on its oral administration were fallimentary without any significant effect on cardiac functionality. The main limitation of CoQ_{10} is based on its very low oral bioavailability and instability that limits dramatically its effects as cardioprotective agent. Herein we loaded CoQ_{10} in high bioavailable nanoemulsions (NEs) coated with chitosan or chitosan and hyaluronic acid in order to improve its performance. We tested cardioprotective and hepatoprotective effects of CoQ_{10} loaded nanocarriers against Doxorubicin and Trastuzumab toxicities. Nanocarriers showed high stability and loading ability and increased cell viability both in hepatocytes and cardiomyocytes during anticancer treatments. We observed that these effects are mediated by the inhibition of lipid peroxidation and reduction of the inflammation. CoQ_{10} loaded nanoemulsions showed also strong anti-inflammatory effects reducing leukotriene B4 and p65/NF-kB expression and Interleukin 1β and 6 production during anticancer treatments.

In conclusion, nanocarriers loaded with Coenzyme Q_{10} placed the scientific bases for preclinical studies of cardio and hepatoprotection in HER2+ breast cancer-bearing mice treated with doxorubicin and trastuzumab.

Introduction

Improvements in cancer survival due to new therapies determined a significant increase of the overall survival[1] with consequent decreases of toxicities[2,3]. Several cancer therapies increase risk of adverse cardiac outcomes such as heart failure (HF) and cardiomyopathy[4]. Such cardiotoxicity is of particular concern for patients undergoing an adjuvant therapy for breast cancer, especially in HER2+ subtype ones, because several widely used drugs can cause abnormalities in left ventricular function, leading to heart failure or cardiomyopathy[5]. Anthracycline is a common breast cancer therapy that increases the risk of HF and cardiomyopathy, as well as hepatotoxicity, which then can persist many years after the conclusion of chemotherapy[6,7]. The monoclonal antibody trastuzumab, also causes cardiotoxicity and hepatotoxicity in breast cancer patients[8,9]. Pooled data from randomized clinical trials estimate that trastuzumab is associated with an absolute increase in HF incidence by 1.6% and abnormalities in left ventricular systolic function by 7.2%[10] which have been reported to be transient in some cases. However, the combination therapy of anthracyclines and anti-HER2 antibodies increases the incidence of cardiotoxicity; in fact, the cumulative incidence of cardiac events in women treated with anthracycline and trastuzumab at 1 year after the diagnosis of breast cancer was 16.4%, at 2 years 23.8 %, and at 3 years 28.2% [11]. Based on these data and to the limited efficacy of traditional cardioprotectants (i.e. beta-blockers and RAAS-inhibitors), the discovery of new cardioprotective agents in these patients

could be of key importance in order to avoid the discontinuation or interruption of the cancer chemotherapy[12] thus potentially increasing overall survival. In a recent trial, lisinopril or carvedilol failed to reduce cardiovascular events in patients with breast cancer[13], confirming the need of new cardioprotective agents. In recent years, our group has performed studies on the detection, management, and pathophysiology mechanisms of the left ventricular dysfunction induced by trastuzumab in breast cancer patients, with evidences that the targeting of oxidative stress, mitochondrial proteins and pro-inflammatory cytokines could be of crucial interest in countering these phenomena in a clinically relevant manner[14]. Notably, doxorubicin and trastuzumab exerts hepatotoxic effects in breast cancer patients[6] with significant increases in aspartate aminotransferase and alanine aminotransferase levels after intravenous administration[15,16] which led to discontinuation of therapy and the biochemical toxic mechanisms underlying these processes are very similar to those described in the heart, always based on the increase in peroxidation, pro-inflammatory cytokines, reduction of calcium homeostasis and mitochondrial metabolism[15,16].

Coenzyme Q_{10}, also called ubiquinone, enhance cardiac function through a variety of mechanisms[17]. In addition to its critical role as a component of the electron transport chain, CoQ_{10} reduces the oxidative processes in vivo[18] like the peroxidation of cell membrane lipids that are strictly associated to HF and atherosclerosis[19].

A recent clinical trial has suggested that CoQ_{10} may be an adjunctive therapeutic option for patients with HF with preserved ejection fraction[17]. Moreover, a recent preclinical trial demonstrated that CoQ_{10} protected cardiomyocytes and ameliorated fibrosis and cell death induced by doxorubicin[20]. Evidence to support its widespread use in cardiology is limited

by small, heterogeneous studies, which are affected by the lower bioavailability of the CoQ_{10} due to its easy degradation in several microenvironments[17]. Dosing of CoQ_{10} suggests that serum targets of >2 mg/L are reasonable to achieve clinical benefit, after oral administration[21] but this blood concentration is not easy to achieve after oral administration without a proper formulation.

To this aim, we loaded CoQ_{10} in high bioavailable nanocarriers and investigated the main biological effects involved in hepato and cardioprotection from doxorubicin and trastuzumab toxicities.

The secondary end-point of the study is based on the active targeting of the nanocarriers, loaded with $CoQ_{10,}$ using a hyaluronic acid-based coating. Hyaluronic acid (HA) is a well known bioavailable polymer that recognize the Cluster Differentiation type 44 (CD44) receptor, overexpressed in heart and liver tissue[22] and strictly involved in cardiac remodeling[23] and atherosclerosis[24] in case of intravenous injection.

The proposed strategy of hepatoprotection and cardioprotection could be of translational importance for oncologists and cardiologists considering the need of new strategies aimed to counteract clinical toxicities of doxorubicin and trastuzumab therapies in HER2+ breast cancer patients.

Results

Dimensional analysis of Co Q_{10} loaded -loaded nanocarriers

O/W NEs were produced as previously described[25]. Because of the importance of scaling down the size in terms of bioavailability once in vivo[26], it was chosen to use the smallest size, among different possible ones that can be tuned with the amount of surfactants. A complete dimensional and morphological study of the simple O/W NEs was performed by DLS and Cryo-TEM analysis. The size

measurements of CoQ_{10} loaded O/W NEs, performed by DLS, was around 100 nm with a narrow size distributions (PdI ≤ 0.1). The Cryo-TEM analysis performed on CoQ_{10} loaded O/W NEs are shown in Figure 1. It is evident from the morphological analysis the level of monodispersions of the basic carrier, and the size distributions are corroborated by DLS analysis. Based on the dimensional results of the simple system, a first layer of chitosan and a second one of hyaluronic acid were deposited above the template of O/W NEs via layer-by-layer technique (LbL)[25]. Indeed, polymers of opposite charge like these were held together thanks to electrostatic interactions. In Table 1, DLS analysis of all the nanocarriers starting from simplest until the more complex ones is summarized (Figure 2). A little increase in term of size from the uncoated to multilayer systems, but with the maintenance of narrow distributions, is observed.

The Z-potential data are reported for all of them. A switch of the charge passing from positively charged CT layer to HA layer is also observed as evidence of complete polymers coating.

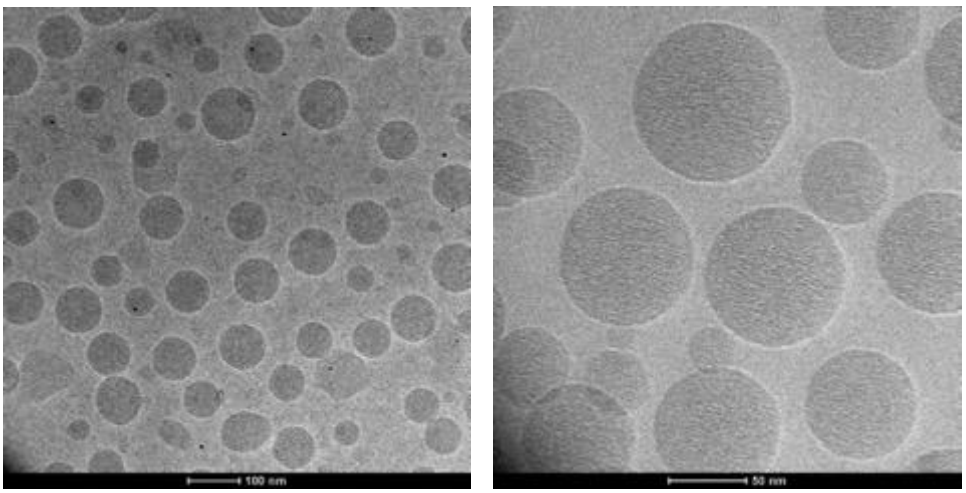

Figure 1: *Cryo-TEM analysis of CoQ_{10} loaded O/W NEs at different magnification. Scale bar is 100 nm on the left and 50 nm on the right.*

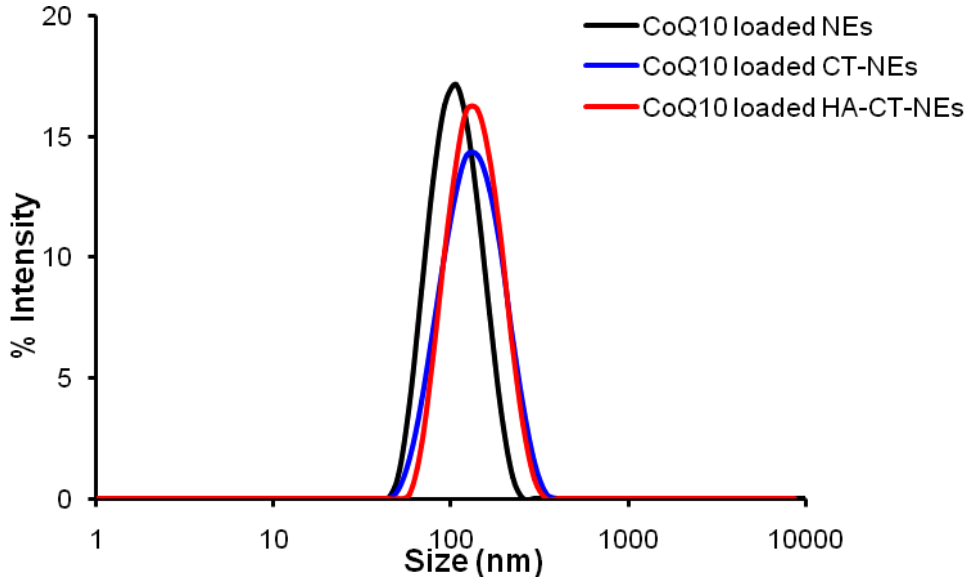

Figure 2: *DLS analysis of CoQ_{10} loaded O/W NEs (black), CoQ_{10} loaded CT-O/W NEs (blue), CoQ_{10} loaded HA-CT-O/W NEs (red).*

Table 1: *Hydrodynamic size, polydispersity index and Z- potential of multilayer nanocarriers.*

	Mean hydrodynamic size (nm)	Polydispersity Index	Z-Potential (mV)
CoQ_{10} loaded NEs	99.77 ± 1.12	0.082 ± 0.008	−24.2± 1.4
CoQ_{10} loaded CT-NEs	127.70 ± 3.95	0.145 ± 0.018	25.5 ± 1.2
CoQ_{10} loaded HA-CT-NEs	129.76 ± 4.30	0.1472 ± 0.021	−24.8 ± 2.6

Secondary and tertiary nanoemulsions were monitored by DLS analysis for several weeks. The samples were stored at room temperature and periodically they were characterized. As reported in Figure 3, a constant size for both

systems is observed. Their stability is also confirmed by unchanged value of PdI, which remains below the conventional stability rank of 0.1, Table 2.

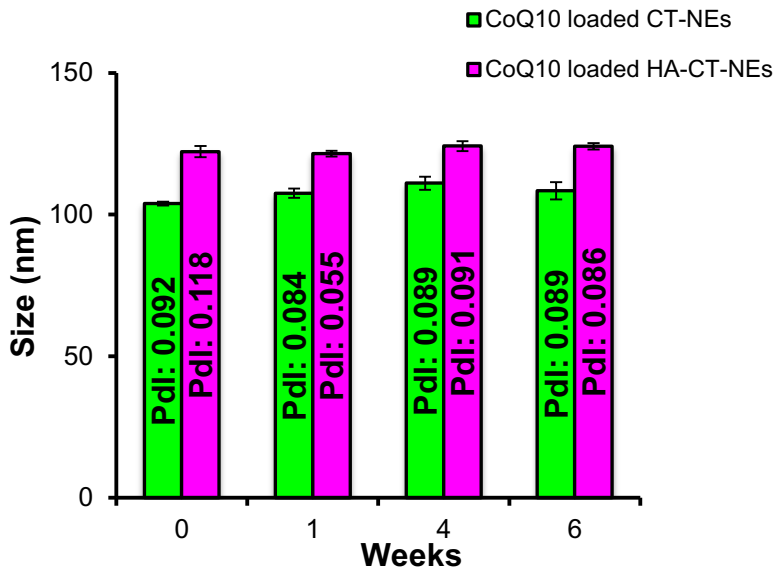

Figure 3: *DLS analysis of CoQ_{10} loaded CT-NEs (green) and CoQ_{10} loaded HA-CT-NEs (purple) over time. Data are expressed as mean ± SD (n=3).*

Table 2: *Stability analysis performed by DLS of multilayer systems*

	Time (weeks)	Size (nm)	PdI	Z-Potential (mV)
CoQ_{10} loaded CT-NEs	0	103.93 ± 0.68	0.092 ± 0.01	20.26 ± 2.11
	1	107.55 ± 1.62	0.083 ± 0.01	32.95 ± 1.12
	4	111.06 ± 2.31	0.087 ± 0.01	41.73 ± 5.98
	6	108.43 ± 3.03	0.089 ± 0.01	43.50 ± 4.68
CoQ_{10} loaded HA-CT-NEs	0	122.23 ± 2.00	0.118 ± 0.01	−31.50 ± 2.66
	1	121.53 ± 1.02	0.055 ± 0.02	−34.33 ± 1.64
	4	124.20 ± 1.73	0.091 ± 0.01	−37.67 ± 1.45
	6	124.10 ± 1.13	0.086 ± 0.01	−34.93 ± 1.45

Cell viability

As shown in Figure 4.1 and Figure 4.2, doxorubicin and trastuzumab at subclinical concentration decreased the cardiomyocytes and hepatocytes viability indicating cellular toxicities but the co-incubation with CoQ_{10} loaded nanocarriers changed the overall picture. The unformulated CoQ_{10} increased up to 15 and 17 % the cardiomyocytes viability during treatments with Doxorubicin and Trastuzumab, however its delivery through nanocarriers enhanced significantly the cardioprotective properties; interestingly, the best protective spectra was observed during the incubation of cells with CoQ_{10}-HA-CT-NEs with a protection rate of about 53 and 47%, at the highest concentration used, compared to doxorubicin and trastuzumab damage, respectively. In human liver cells we have seen the same behavior with the best protection rate while using CoQ_{10} loaded HA-CT-NEs.

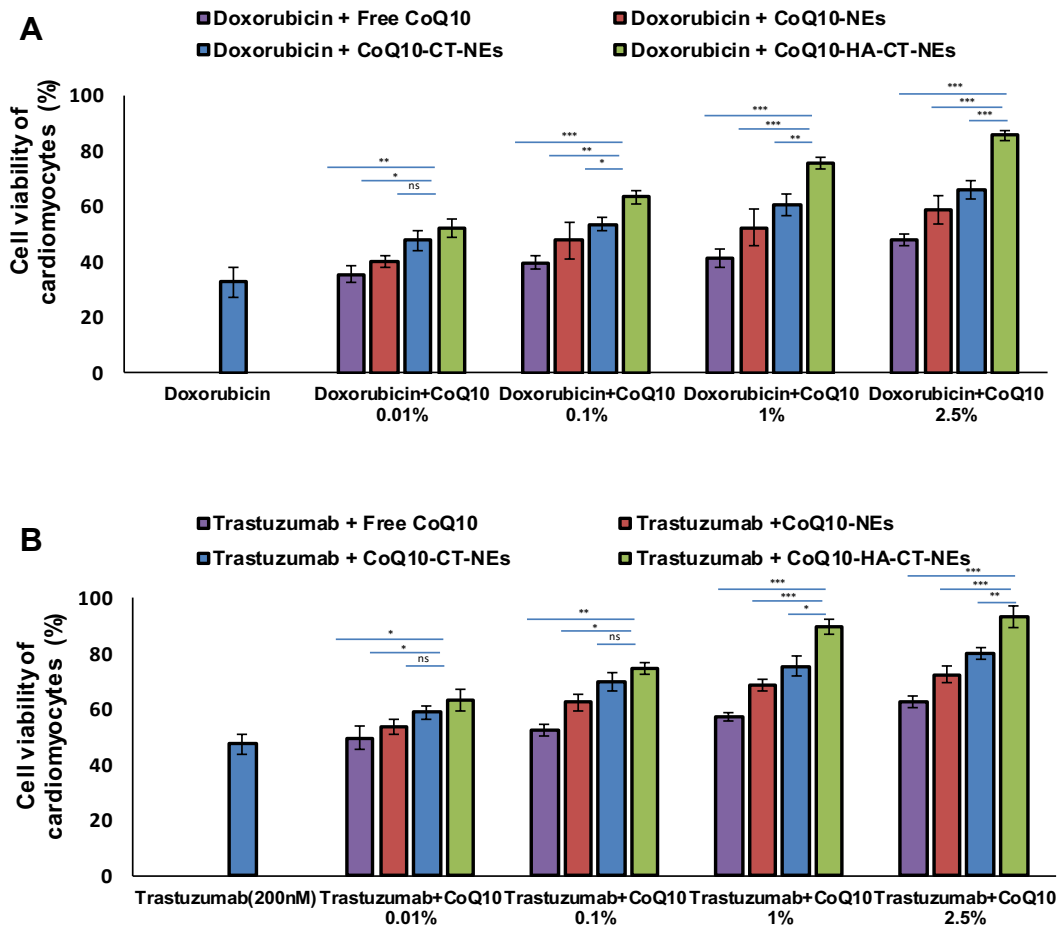

Figure 4.1: *Cell viability in function of the concentration of free CoQ_{10} or CoQ_{10} loaded O/W NEs, CT-O/W NEs and HA-CT-O/W NEs tested alone or combined with doxorubicin or trastuzumab at 200 nM for 72h: cardiomyocytes were treated with doxorubicin 200 nM (A), and with trastuzumab 200 nM (B). *p<0.001 ;**p<0.05; ns: not significant.*

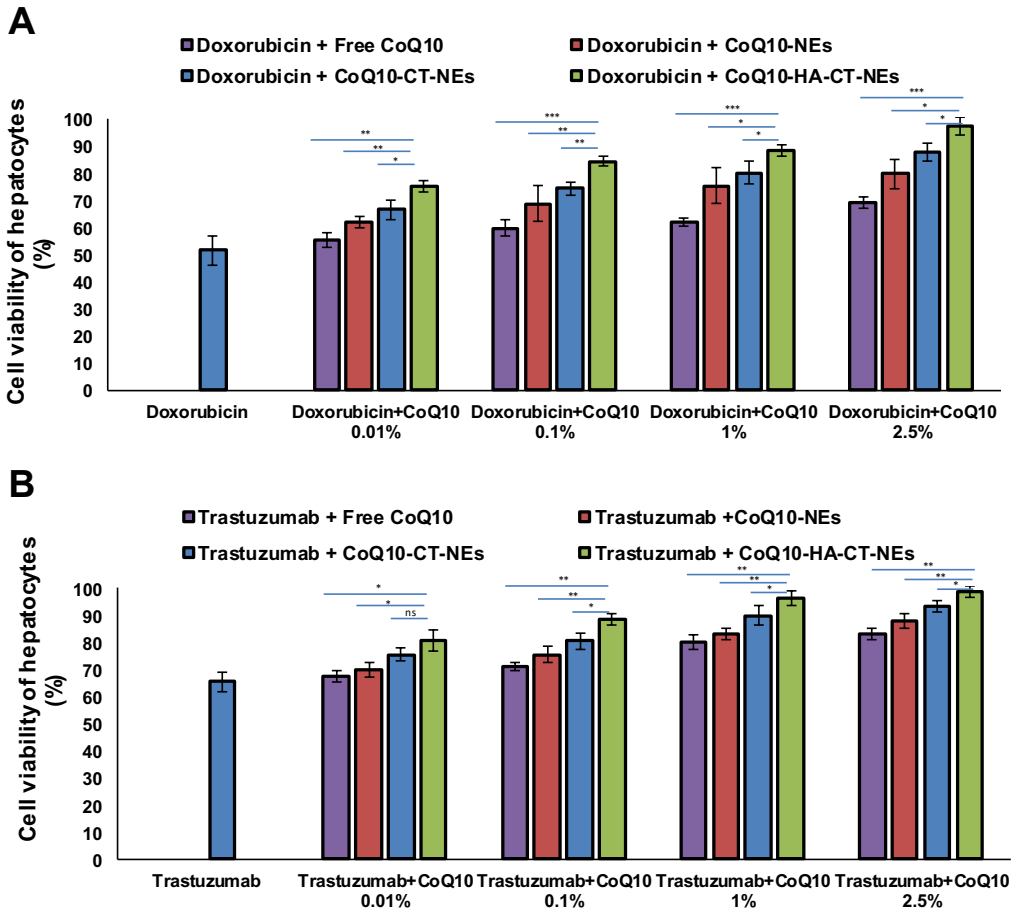

Figure 4.2: *Cell viability in function of the concentration of free CoQ_{10} or CoQ_{10} loaded O/W NEs, CT-O/W NEs and HA-CT-O/W NEs tested alone or combined with doxorubicin or trastuzumab at 200 nM for 72h: hepatocytes were treated with doxorubicin 200 nM (A), and with trastuzumab 200 nM (B). *p<0.001 ;**p<0.05; ns: not significant.*

Detection of intracellular reactive oxygen species

The H9c2 cell lysate fraction is used as a model to measure the antioxidative effect of CoQ_{10}-loaded nanocarriers under anticancer treatments (Figure 5.1 and 5.2). As reported elsewhere[27,28], cardiotoxicity of doxorubicin and trastuzumab is also mediated by the production of intracellular ROS (iROS) and the same mechanism is at the basis of the hepatotoxicity of these drugs. As clearly shown, both drugs increase iROS production and co-incubation with CoQ_{10} shows very evident antioxidant effects. In particular, with respect to cardiomyocytes treated with doxorubicin and trastuzumab alone, iROS are only reduced of 10-13% by treatment with unformulated CoQ_{10}. Conversely, nanocarrier based formulations, also in this case, have improved CoQ_{10} antioxidant properties, which have been maximized in case of CoQ_{10}-HA-CT-NEs, with a reduction of iROS production up to 74-80% ($p<0.001$). The same pattern was seen in liver cells.

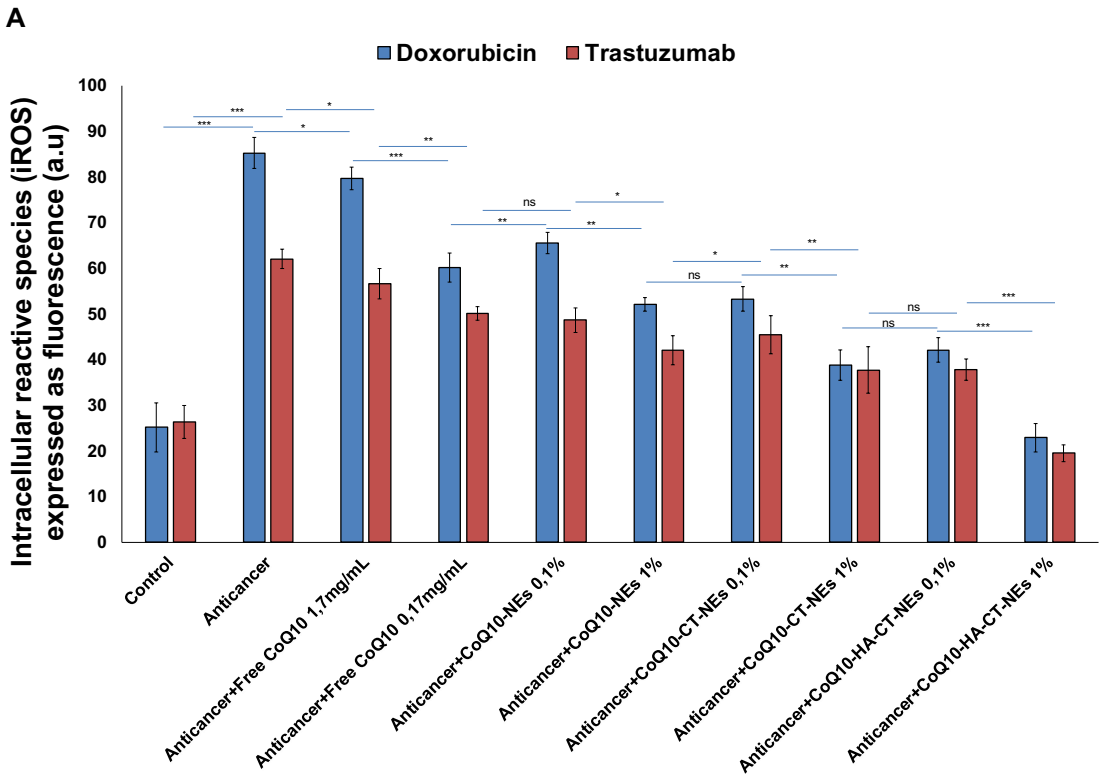

Figure 5.1: *(A) Detection of intracellular reactive oxygen species by fluorescence (a.u) in cardiomyocytes (5000 cells/well). Cells were pretreated with free CoQ_{10} or CoQ_{10} loaded O/W NEs, CT-O/W NEs, HA-CT-O/W NEs at 0.1 and 1% of oil for 4 h, before stimulation with doxorubicin or trastuzumab at 200 nM for 12 h. * $p < 0.001$; ** $p<0.05$.*

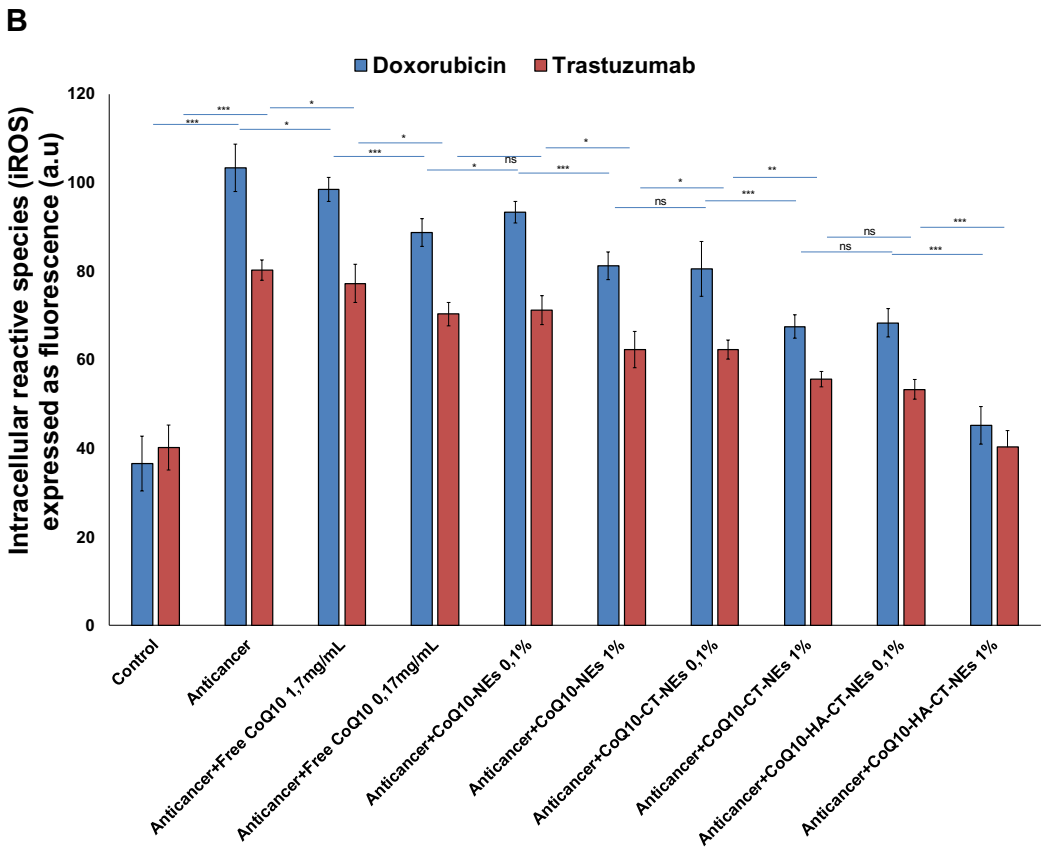

Figure 5.2: *(B) Detection of intracellular reactive oxygen species by fluorescence (a.u) in human liver cells (5000 cells/well). Cells were pretreated with free CoQ_{10} or CoQ_{10} loaded O/W NEs, CT-O/W NEs, HA-CT-O/W NEs at 0.1 and 1% of oil for 4 h, before stimulation with doxorubicin or trastuzumab at 200 nM for 12 h. * p < 0.001; ** p<0.05.*

Lipid peroxidation studies

As a marker of oxidative stress at the membrane lipid level, we quantified the production of malondialdehyde in both cardiomyocytes and liver cells exposed to doxorubicin and trastuzumab and, interestingly, we have shown that both drugs induce toxic effects also through cellular hyperproduction of malondialdehyde which is a well known mutagenic and pro apoptotic factor. CoQ_{10} acts at the level of cellular membrane so we have shown that its co-incubation decreases lipid peroxidation too. In fact, in the formulations

studied, CoQ_{10} is able to drastically reduce the formation of malondialdehyde up to baseline values of non-exposure to anticancer drugs. CoQ_{10}-HA-CT-NEs had the best properties thereby corroborating the results previously described (Figure 6.1 and 6.2).

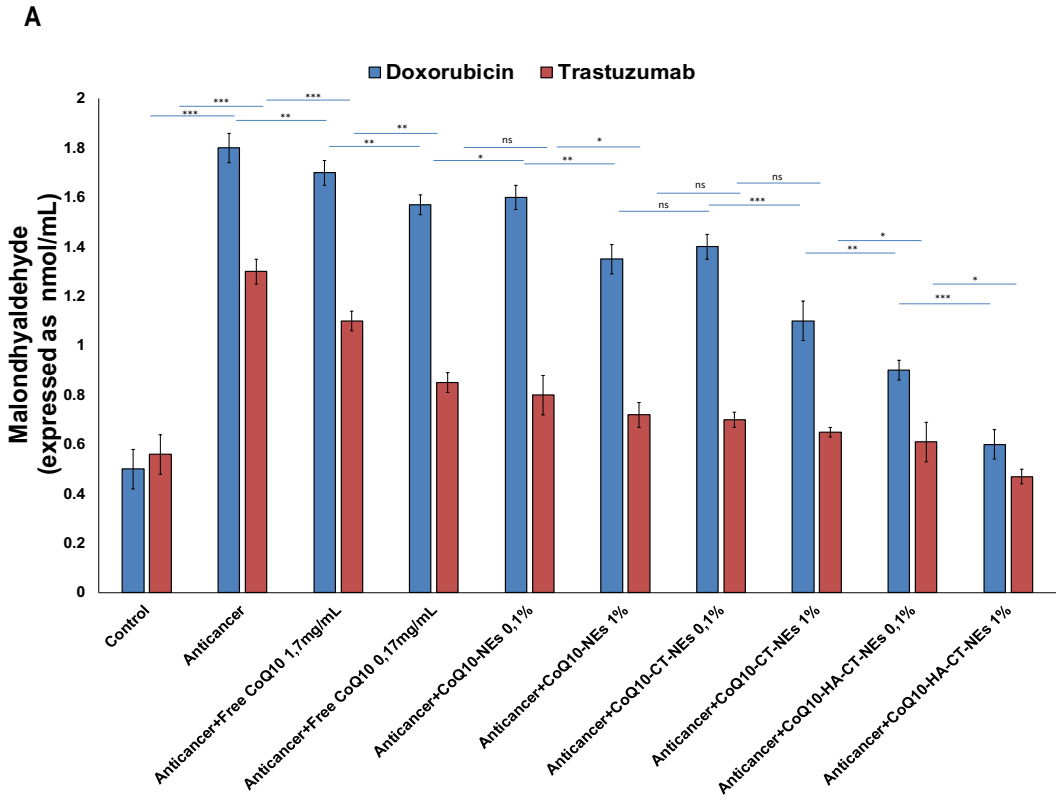

Figure 6.1: *(A) Quantification of MDA production in cardiomyocytes treated with doxorubicin or trastuzumab alone or combined to free CoQ_{10} or CoQ_{10} loaded O/W NEs, CT-O/W NEs, HA-CT-O/W NEs at 0.1 and 1% of oil. *p<0.001; **p<0.05.*

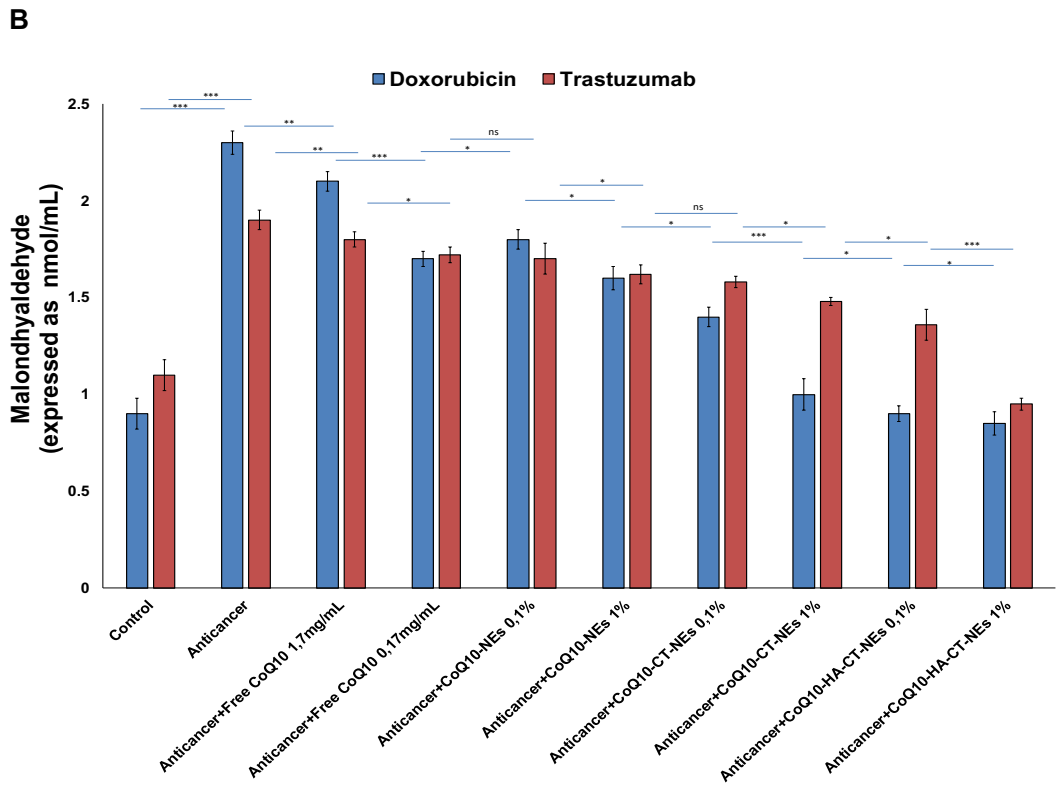

Figure 6.2: *(B) Quantification of MDA production in hepatocytes treated with doxorubicin or trastuzumab alone or combined to free CoQ_{10} or CoQ_{10} loaded O/W NEs, CT-O/W NEs, HA-CT-O/W NEs at 0.1 and 1% of oil. *p<0.001; **p<0.05.*

Leukotriene B_4 expressions

Considering the close link between inflammation and cellular apoptosis, we investigated changes in the expression of Leukotrienes in cardiac and hepatic cells exposed to anticancer drugs. Both the pro-oxidative pathway induced by doxorubicin and the inhibition of the ERB2-dependent pathway mediated by trastuzumab determines a great activation of pro-inflammatory prostaglandins[29,30]. In fact the exposure of cardiac and hepatic cells to both drugs increases the protein expression of Leukotrienes by about 3-4 times. CoQ_{10} loaded nanocarriers reduces drastically the production of leukotrienes; also in this case, the best ones with anti-inflammatory activities were the

hyaluronic acid coated nanoemulsions, both in cardiomyocytes and liver cells (Figure 7.1 and 7.2).

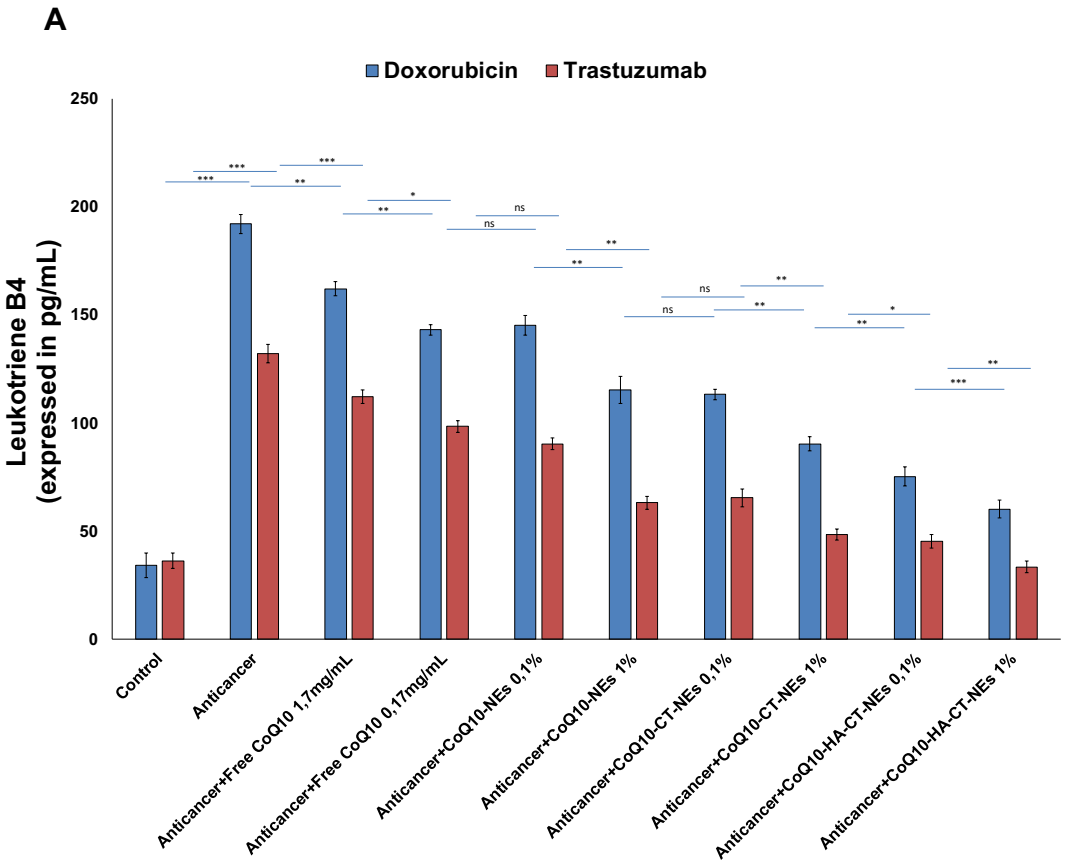

Figure 7.1: *(A) Leukotriene B_4 protein expression in cardiomyocytes both unexposed or exposed to doxorubicin or trastuzumab alone or combined with free CoQ_{10} or CoQ_{10} loaded O/W NEs, CT-O/W NEs, HA-CT-O/W NEs at 0.1 and 1% of oil. *p<0.001; **p<0.05.*

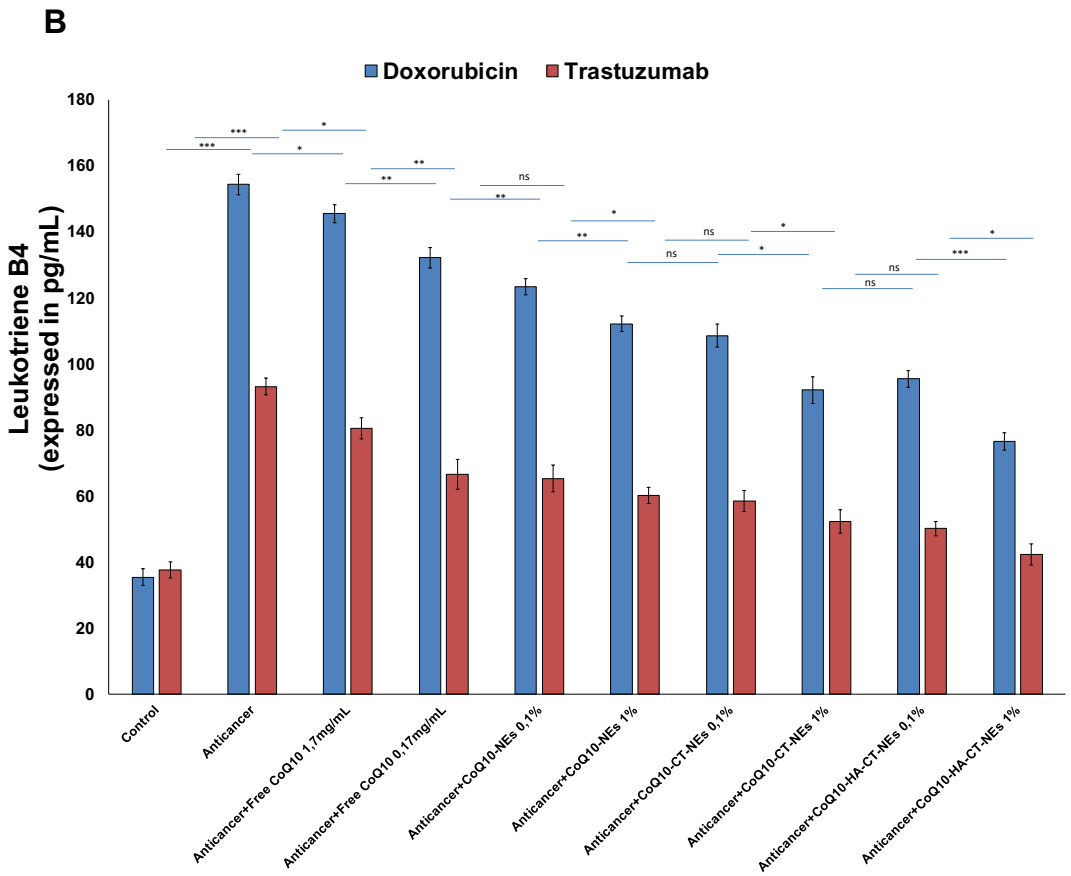

Figure 7.2: *(B) Leukotriene B_4 protein expression in liver cells both unexposed or exposed to doxorubicin or trastuzumab alone or combined with free CoQ_{10} or CoQ_{10} loaded O/W NEs, CT-O/W NEs, HA-CT-O/W NEs at 0.1 and 1% of oil. *p<0.001; **p<0.05.*

p65/NF-kB expression

Considering that IKK/NF-κB activation in cardiomyocytes is sufficient to induce cardiomyopathy and HF by enhancing inflammatory response and myocyte atrophy as well as liver cirrhosis and hepatomegaly[31,32], we investigated on the role of this mediator in the genesis of cardiac and liver toxicity of doxorubicin and trastuzumab. In agreement with the previous results, both the anthracycline and the ERB2 inhibitor increases the

expression of p65/NF-kB thus giving rise to a strong cellular inflammatory state that exacerbates cell death (Figure 8.1 and 8.2). Doxorubicin triples the expression of NF-kB whereas trastuzumab increases it by about 2.3-fold compared to untreated cells. Liver cells exhibit similar behavior but are generally less susceptible to pro-inflammatory damages of the drugs being tested. However, co-incubation with CoQ_{10} improves the general inflammatory status of both cardiac and hepatic cells from the damage of the drugs used herein. Also in this case the best formulation was the CoQ_{10}-HA-CT-NEs, which improves the biological properties of CoQ_{10} by 25-20% compared to CoQ_{10}-CT-NEs.

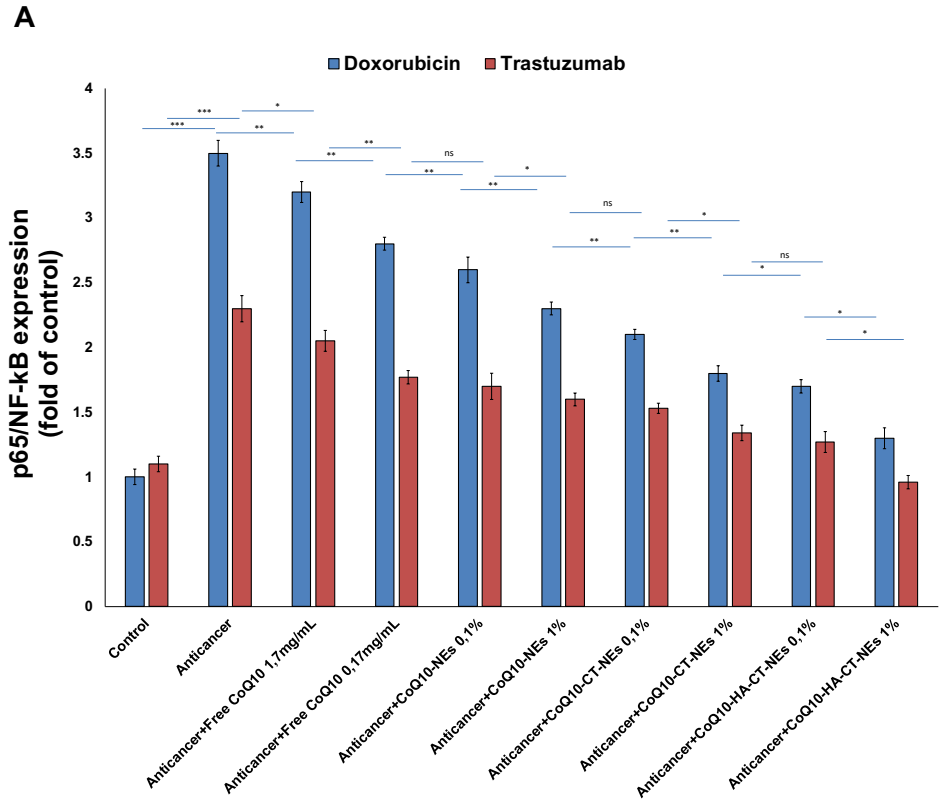

Figure 8.1: *(A) p65/NF-κB expression in cardiomyocytes either unexposed or exposed to doxorubicin or trastuzumab alone or combined with free CoQ_{10} or CoQ_{10} loaded O/W NEs, CT-O/W NEs, HA-CT-O/W NEs at 0.1 and 1% of oil. *p<0.001; **p<0.05.*

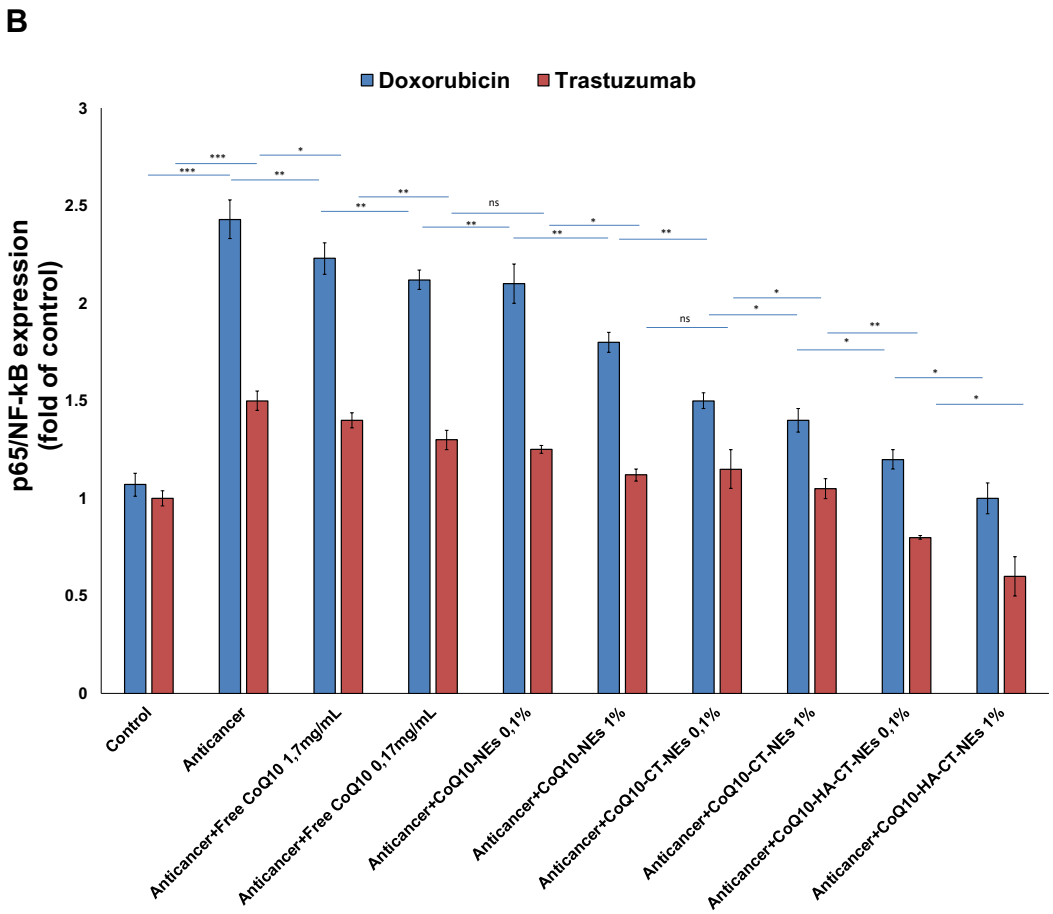

Figure 8.2: *(B) p65/NF-κB expression in liver cells either unexposed or exposed to doxorubicin or trastuzumab alone or combined with free CoQ_{10} or CoQ_{10} loaded O/W NEs, CT-O/W NEs, HA-CT-O/W NEs at 0.1 and 1% of oil. *p<0.001; **p<0.05.*

Interleukins

The NF-kB nuclear translocation induces many epigenetic changes including hyper expression of cytokines, chemokines and interleukins that stimulate tumor cell growth, chemo and radio resistance but also cardiac and hepatic toxicity to many drugs[33]. For this reason, we investigated Interleukin 6 and 1 change after exposure to doxorubicin and trastuzumab. Anthracycline increases the expression of interleukin 1 and about 3 times that of interleukin

6 by 2.5 times. Trastuzumab has a less important but still significant pro-inflammatory action with increases of about 2-2.5 times of the expression of both interleukins. We have seen similar behavior, but less evident, with human liver cells that appear to be less responsive to pro-inflammatory damage than anthracycline and ERB2 inhibitor. Also in this case the CoQ_{10} showed a behavior quite similar to that observed for NF-kB with significant reductions in both cell lines, up to lower values compared to the basal ones, in the case of CoQ_{10}-HA-CT-NEs, at 1% of oil (Figure 9 to 12).

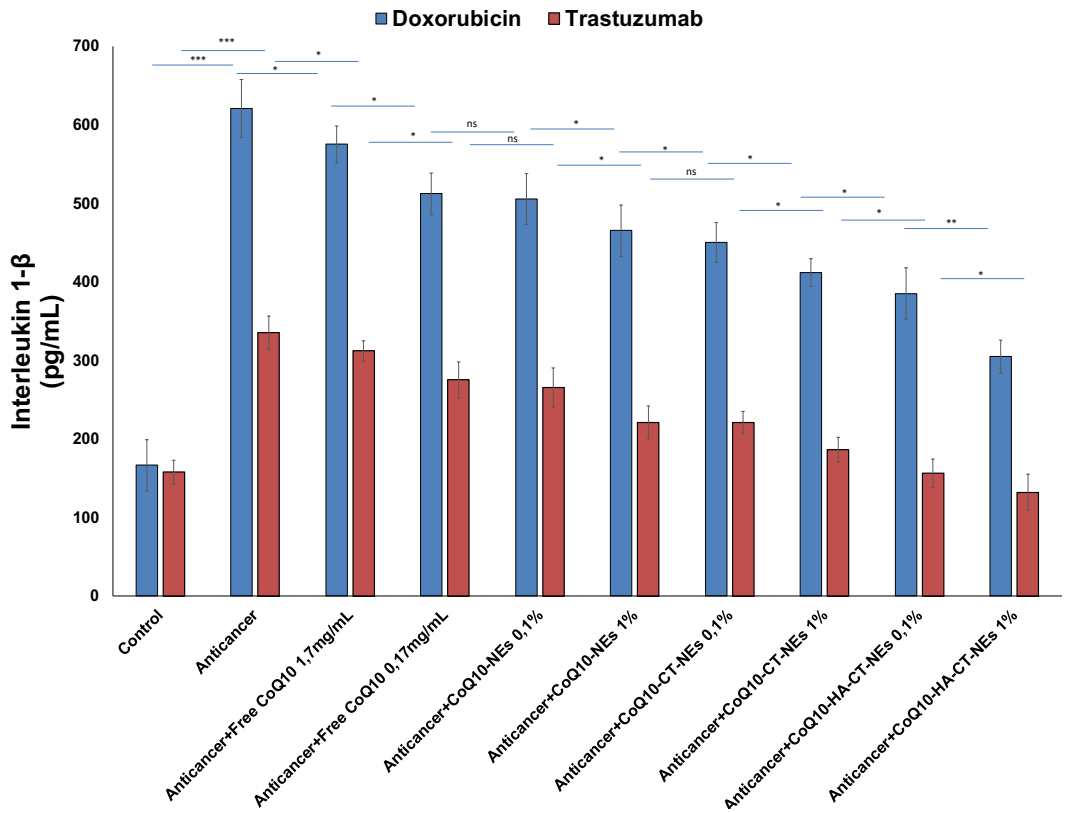

***Figure 9**: Interleukins1-β expression in cardiomyocytes either unexposed or exposed to doxorubicin or trastuzumab alone or combined with free CoQ_{10} or CoQ_{10} loaded O/W NEs, CT-O/W NEs, HA-CT-O/W NEs at 0.1 and 1% of oil. *p<0.001; **p<0.05.*

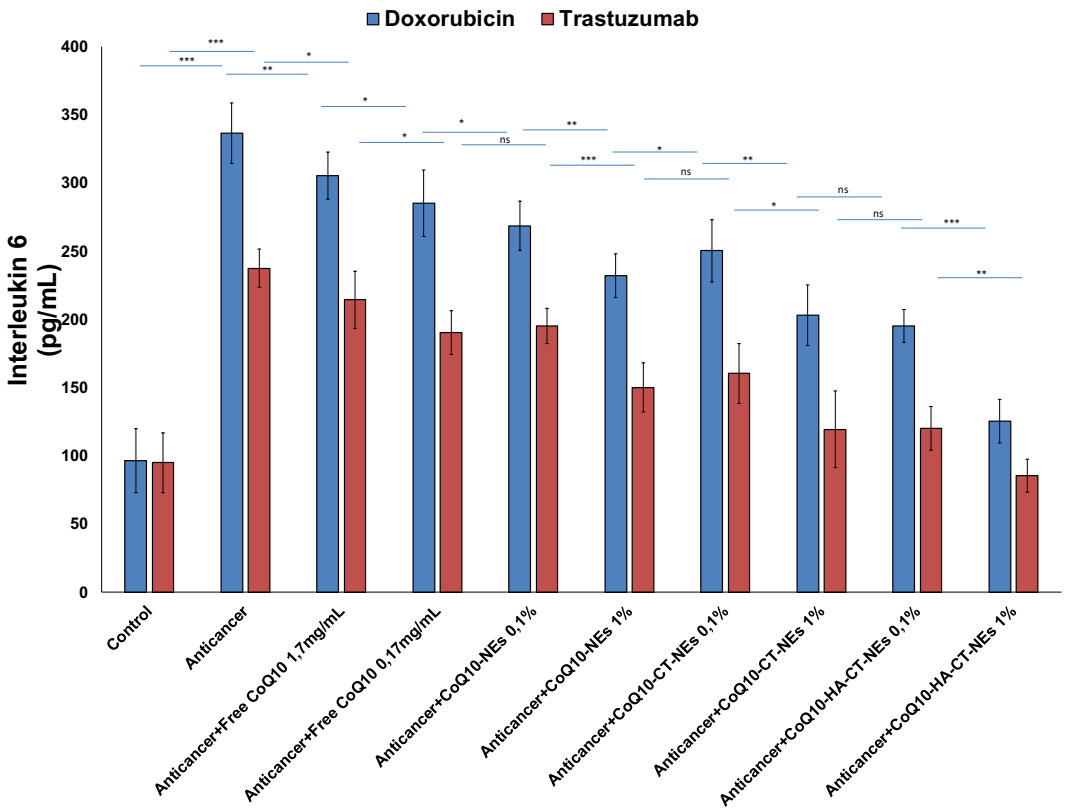

***Figure 10**: Interleukins 6 expression in cardiomyocytes either unexposed or exposed to doxorubicin or trastuzumab alone or combined with free CoQ_{10} or CoQ_{10} loaded O/W NEs, CT-O/W NEs, HA-CT-O/W NEs at 0.1 and 1% of oil. *p<0.001; **p<0.05.*

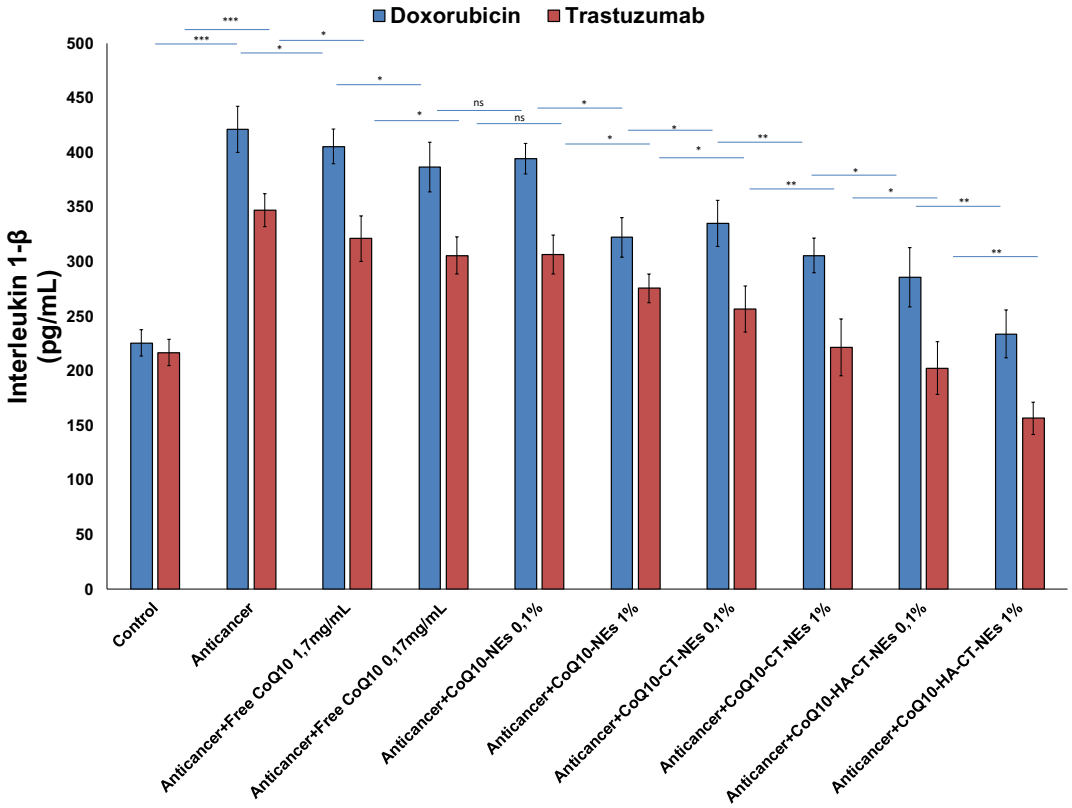

***Figure 11**: Interleukins1-β expression in liver cells either unexposed or exposed to doxorubicin or trastuzumab alone or combined with free CoQ_{10} or CoQ_{10} loaded O/W NEs, CT-O/W NEs, HA-CT-O/W NEs at 0.1 and 1% of oil. *p<0.001; **p<0.05.*

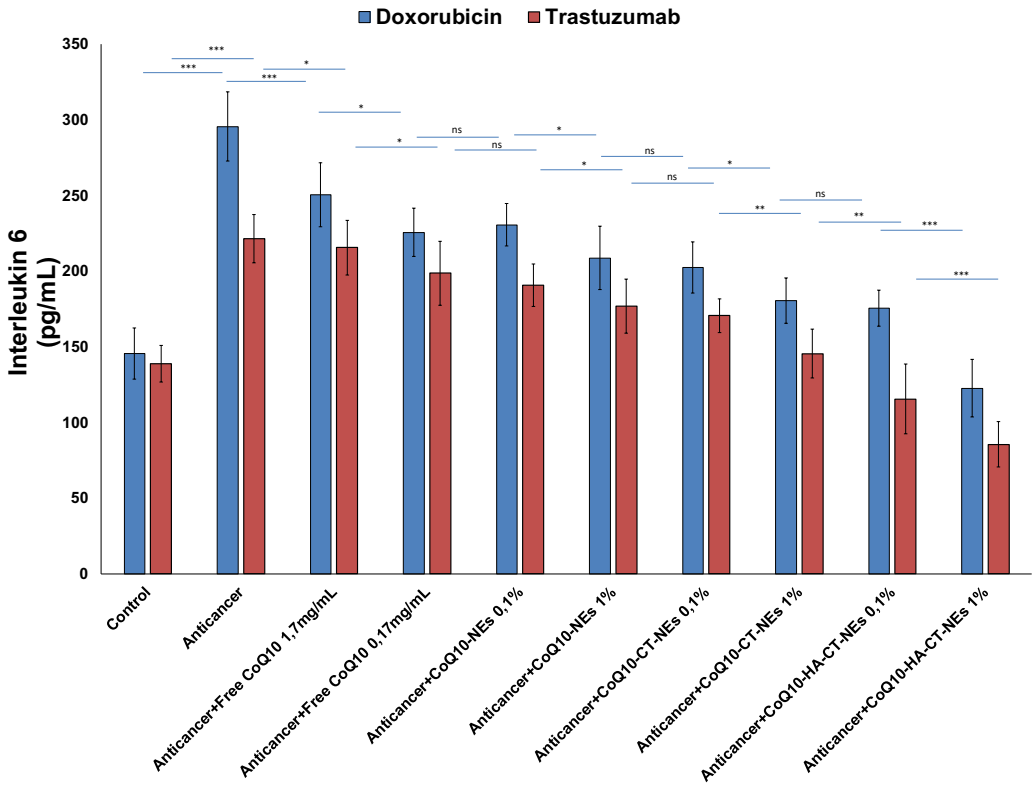

***Figure 12**: Interleukins 6 expression in liver cells either unexposed or exposed to doxorubicin or trastuzumab alone or combined with free CoQ_{10} or CoQ_{10} loaded O/W NEs, CT-O/W NEs, HA-CT-O/W NEs at 0.1 and 1% of oil. *p<0.001; **p<0.05.*

Discussion

Breast cancer is the most common cancer among women[34]. In the last twenty years early diagnosis, neoadjuvant and adjuvant systemic treatment targeted to specific molecular targets have significantly reduced the mortality from breast cancer[34,35]. However, the increase in survival has allowed to observe the cardiotoxic effects of anticancer therapy and increased mortality from cardiovascular causes, resulting in a large literature where experts try to identify the correct management of this critical issue[2,3]. It is known that the highest rates of trastuzumab induced cardiotoxicity are observed in patients receiving trastuzumab after treatment with an anthracycline[8,10]. Although the anthracycline containing treatment regimens remain superior with regard to both disease-free and overall survival in long-term follow-up, the differences are small and often weigh against the risk of cardiotoxicity[7]. The pathophysiology of the cardiotoxicity is always based on pro-oxidative, anti-metabolic and pro-inflammatory processes in cardiac tissues[36,37]. These metabolic pathways involve several interleukins, cytokines, growth factors and hormones of key importance for cardiomyocyte survival[38]. Nutraceuticals are natural bioactives that exert anti-inflammatory activities[39]. CoQ_{10} is a highly lipophilic molecule with a chemical structure quite similar to those of Vitamin-K[17]. Although being a common component of cellular membranes, CoQ_{10} induces the production of adenosine triphosphate in the mitochondria increasing cell viability[17]. Several trials during the past 30 years examining CoQ_{10} in patients with HF have been limited by small numbers and lack of contemporary HF therapies[40]. The recent publication of the Q-SYMBIO randomized controlled trial demonstrated a reduction in major adverse cardiovascular events with CoQ_{10} supplementation in a contemporary HF

population[41]. Although having limitations, this study has renewed interest in evaluating CoQ_{10} supplementation in patients with HF. Current literature suggests that CoQ_{10} is relatively safe with few drug interactions and side effects, as example the increases in the metabolism of warfarin[42]. One of the main clinical limitations of CoQ_{10} is related to its low bioavailability after oral administration, thus limiting its biological action[43]. For this reason, the aim of the study was based on improving the stability and bioavailability of the molecule by nanoemulsions already tested in animal models in previous studies published by our research group[44].

Here we show that the biological effect of CoQ_{10} is enhanced when loaded in bioavailable nanocarriers, providing multiple molecular mechanisms of cardioprotection during doxorubicin and trastuzumab treatments. The anti-inflammatory activities of the nanocarriers described herein hold potential in terms of modulating the heart microenvironment thereby providing insights for further preclinical studies, also in combination with other cardiotoxic anticancer drugs, namely anti-VEGF antibodies and immune check point inhibitors. In particular, the best cytoprotective properties were seen with CoQ_{10}-HA-CT-NEs, which are aimed to be delivered by intravenous injection exploiting the antifouling properties of the hyaluronic acid and its natural affinity against CD44. Very promising is also the CoQ_{10}-CT-NEs system, which due to the external chitosan coating, may be orally delivered by taking advantage from the gastroprotection and mucoadhesive properties provided by chitosan[44]. Preclinical studies are currently performed in our group to evaluate modification of left ventricular ejection fraction and global longitudinal strain upon administration of nanocarriers during doxorubicin and trastuzumab treatments.

Conclusion

Doxorubicin and trastuzumab induced cardiotoxicity is a well known side effect seen in HER2+ breast cancer patients allowing to greater risk of discontinuation or interruption of drug therapies. The pro-inflammatory and mitochondrial-based toxicities have the same key roles in the toxicities of both drugs. This study shows that nanomedicines are able to increase the biological effects of CoQ_{10}, particularly when they are coated with hyaluronic acid, in cardiomyocytes and hepatocytes, considering the prognostic role of CD44 expression in these cells. The overall picture obtained in this study places the biochemical evidences and preliminary results aimed to use highly bioavailable nanomedicines loaded with CoQ_{10} as potential preventive strategy of cardiovascular and hepatic side events in HER2+ breast cancer patients.

Materials and methods

Materials

Both soybean oil (density at 20 ° C of 0.922 g mL^{-1}) and surfactant Lipoid E80 (egg lecithin powder 80%–85% enriched with phosphatidyl choline (PC) and 7%–9.5% content in phosphatidyl ethanolamine (PE)) were purchased from Lipoid GmbH and used without further purification. Millipore Milli-Q water was used for the preparation of all nanoemulsions and solutions. Chitosan (CT, LMW 90–150 kDa, DDA 84% determined via ^{1}H-NMR) was purchased from Sigma Aldrich (Milan, Italy). Hyaluronic acid 250 kDa were purchased from Creative PEGWorks (HA) and used without further purification. Ubidecarenone CoenzymeQ_{10} (CoQ_{10}) was kindly offered from Faravelli.

Preparation of nanoemulsions

Primary nanoemulsions were prepared adapting a previously developed protocol[25,26]. Briefly, first the oil phase was prepared by adding the surfactant to the soybean oil. A 5.8 g of Lipoid E 80 was dissolved in 24 mL of soybean oil at 60°C and mixed using the immersion sonicator (Ultrasonic Processor VCX500 Sonic and Materials). An amount of 4.08 g of CoQ_{10} were dissolved in the oil phase at 60 °C for 1 h, then added dropwise to the aqueous phase (Milli-Q water) and mixed again using the immersion sonicator. The pre-emulsions were finally passed at 2000 bar through the high-pressure valve homogenizer (Microfluidics M110PS) for the first three individual cycles to greatly reduce the initial size, then the reservoir was continuously refilled for 200 steps. This method was used for the preparation of all oil-in-water nanoemulsions (O/W NEs) at 20 wt% of oil concentration. NEs were characterized by measuring size, polydispersity index (PdI) and Z-potential values through dynamic light scattering (DLS, Malvern Zetasizer). Before each experiment, 20 µL aliquots

were withdrawn from each sample and diluted 1:40 (v/v) with Milli-Q water. The diluted samples were poured into disposable cells, and the size and the ζ-potential were determined at 25 °C at least 3 times for each sample. In particular, the particle size distribution was measured by DLS (λ= 632.8 nm) using a detecting angle of 173°.

Layer by layer deposition of polymers on nanoemulsions

A first layer of CT was deposited above the nanoemulsions (secondary nanoemulsions). 0.1 M acetic acid solution of CT pH 4 (0.2 wt%) was prepared. Nanoemulsions 20 wt% oil were added to the CT solution quickly under vigorous stirring and kept under stirring for 15 min to allow uniform chitosan deposition. Final concentrations of oil and CT were 10 and 0.1 wt%, respectively, while the pH of the final secondary nanoemulsions was 4. These nanoemulsions were re-dispersed using the method reported previously[25] and stored at room temperature. The second layer of hyaluronic acid (HA) was prepared by aid of two syringe pumps (HARVARD APPARATUS 11 PLUS) and an ultrasonic bath (FALC INSTRUMENTS) according to a previously reported method[26]. Starting from the secondary nanoemulsions 10 wt% oil - 0,1 wt% CT, a polymer layer was deposited by mixing 1:1 (v:v) of a 0.24 wt% aqueous solution of HA, with the secondary nanoemulsions suspension. The two liquid phases were injected at the same flow rate (0.4 $mL \cdot min^{-1}$) through two micrometric capillaries interfaced at their extremities. Each drop was then collected inside a glass tube immersed in the ultrasonic bath at room temperature, 59 kHz and 100% power for 15 minutes. Multilayer systems were characterized at each step of preparation by DLS as previously described.

Cryo-TEM characterization

The morphology of nanoemulsions was observed by Cryo transmission electron microscopy (Cryo-TEM) analysis. For the preparation of the frozen-hydrated sample the plunge freezing method was performed. Briefly a drop of 3 µL of the sample were deposited on a 200 mesh holey carbon grids (Ted Pella, USA), then it was inserted in the chamber of a FEI Vitrobot Mark IV (FEI company, the Netherland) at 4°C and 90% of humidity. The droplet of sample was blotted with filter paper for 1 s, (blot force 1, drain time 0.5 s) and then the grid was plunged into the liquid propane. The grid was then stored in liquid nitrogen in a grid box until it was finally transferred to a cryo-specimen 626 holder (Gatan, Inc., USA) and loaded into the cryo-transmission electron microscope for imaging. To obtain the image of the nanoparticles we used a Tecnai G2 20, a Cryo-TEM transmission electron microscope (FEI company, the Netherland) equipped with LaB6 emitter (acceleration voltage of 200 kV) and recorded at with a 2 k × 2 k CCD-Eagle 2HS camera. The Frozen-hydrated sample is radiation-sensitive material so to avoid damaging; the observation was carried out in Low Dose Mode.

Mitochondrial viability of hepatocytes and cardiomyocytes

To evaluate the cardioprotective effects of CoQ_{10}-loaded nanocarriers on Human Fetal Cardiomyocytes (HFC cells) (American Type Culture Collection, Manassas, VA, USA) and human liver cells (THLE-2 cell line) (CRL-2706™American Type Culture Collection, Manassas, VA, USA), we measured the mitochondrial dehydrogenase activity of these cells using an MTT [3-(4,5-dimethyldiazol-2-yl)-2,5- diphenyltetrazoliumbromide] assay according to the manufacturer's instructions (Dojindo Molecular Technologies Inc., Rockville, MD, USA)[45].

Human hepatocytes were cultured in BEGM Single Quots medium containing 10% FBS and DMEM/F-12 (1:1) mixture containing 10% FBS in 96-well plates at a density of 10,000 cells per well at 37°C in a humidified 5% CO_2 atmosphere. After 24h of appropriate growth, cells were treated for three days with doxorubicin or trastuzumab alone (both at 200 nM) or co-incubated with unformulated CoQ_{10} at 0.017, 0.17, 1.7 and 4.25 mg/mL or CoQ_{10}-loaded NEs, CT-NEs or HA-CT-NEs at 0.01, 0.1, 1 and 2.5 % w/v of oil in cell culture medium (corresponding to each concentration of the unformulated drug). After treatments, cells were washed three times with PBS at pH neutral and incubated with 0.1 mL of an MTT solution properly appropriately diluted in cell culture medium) for 4 h at 37°C. Absorbance readings were acquired at a wavelength of 450 nm with the Tecan Infinite M200 plate-reader (Tecan Life Sciences Home, Männedorf, Switzerland) using I-control software. Relative cell viability (%) was calculated with the following formula $[A]_{test}/[A]_{control}\times 100$, where "$[A]_{test}$" is the absorbance of the test sample, and "$[A]_{control}$" is the absorbance of the control cells incubated solely in culture medium. Then, we evaluated cell cytotoxicity; we measured the total protein content using the Pierce Micro BCA protein assay kit (Thermo Fisher, Milan, Italy). In brief, cells were washed with ice-cold PBS, and incubated for 15 min in 0.15 mL of a cell lysis buffer (0.5 % v/v Triton X-100 in PBS) that included 150 µL of the Micro BCA protein assay kit reagent (prepared according to the manufacturer's instructions). Absorbance at 562 nm was measured on a plate reader. Cytotoxicity measurements were normalized by the amount of total protein content in each well.

Quantification of intracellular reactive oxygen species (iROS)

The quantification of intracellular reactive oxygen species, a source of pro-inflammatory and mutagenic mediators, was evaluated using a DCFH-DA probe, as described elsewhere[46]. Briefly, cells were grown under standard condition as described in paragraph 2.3. Subsequently, $5x10^3$ cells/well were seeded in a 24-well plate and allowed to grow for 24h. After washing twice with PBS, cells were pretreated or not with CoQ_{10} loaded nanocarriers at 0.1 and 1% w/v of oil (corresponding to the equivalent dose of CoQ_{10} of 0.17 and 1.7 mg/mL) for 4 h and then incubated with 5 μM DCFH-DA in PBS for 30min. After the DCFH-DA removal, cells were stimulated with doxorubicin or trastuzumab at 200 nM for 12 h. The dose of the drugs used in this study is a subclinical concentration used in other work because re-entering within the ranges (25–250 nmol/L) for steady-state plasma concentrations reported after administration in humans[47]. After treatments, cell fluorescence was measured using a microplate spectrofluorometer (xMark Microplate, Spectrofluorometer Biorad, Milan, Italy). Intracellular antioxidant activity was expressed as percentage (%) of untreated cells.

Analysis of lipid peroxidation

After the appropriate cell growth, cardiomyocytes and hepatocytes were seeded in a 24-well plate and allowed to growth for one day. Lipid peroxidation, having a key role in the etiopathogenesis of the cardiac and hepatic damage of anticancer drugs, was induced by incubating cells with doxorubicin or trastuzumab (200 nM) for 6 h; anti-oxidant studies were performed by a pre-incubation for 4h with unformulated or formulated CoQ_{10} –loaded nanocarriers and subsequently treatments with anticancer drugs. After treatments, cells were washed three times with cold PBS, harvested with

0.25% v/v Trypsin and centrifuged at 1000 ×g for 10 min. The supernatant was discarded and the cell pellet sonicated in cold PBS. After a centrifugation step at 800 ×g for 5 min, we quantified malondialdehyde (MDA) by using a commercial kit with a spectrophotometer according to the manufacturer's protocols (Sigma Aldrich, Milan, Italy)[48]. We measured the protein content of the cell homogenates using the Micro BCA protein assay kit (Pierce, Thermo Fisher, Milan, Italy) according to kit instructions.

Expression of leukotriene B_4 (LTB_4)

Cardiomyocytes and hepatocytes were treated or not with unformulated or formulated CoQ_{10} for 4h before exposure to doxorubicin or trastuzumab (200 nM) for 12 h. After treatments, the leukotriene B_4 ((5S,12R)-dihydroxy-6,14Z-8,10E-eicosatetraenoic acid) expression in cell lysates was calculated by using ELISA (Cayman Chemical) following the supplier's instructions[49]; data were expressed as pg of leukotriene B_4/mg of cell proteins calculated by QuantiPro Assay (Biorad, Milan, Italy).

Determination of p65/NF-kB expression

Cardiomyocytes and hepatocytes were treated or not with unformulated or formulated CoQ_{10} for 4h before exposure to doxorubicin or trastuzumab (200 nM) for 12 h. After treatments, cellular extracts were analyzed using the TransAM NF-κB p65 transcription factor assay kit (Active Motif, Carlsbad, CA), according to the manufacturer's recommendations[50]. NF-κB complexes were isolated by a specific binding to a consensus 5′-GGGACTTTCC-3′ oligonucleotide immobilized on a 96-well plate. The NF-κB bounded to the oligonucleotide was quantified by using an anti-p65 primary antibody followed by horseradish peroxidase (HRP)-conjugated goat anti-rabbit IgG. The quantification of the complexes was obtained using a spectrophotometric

detection at a wavelength of 450 nm using a microplate spectrofluorometer (xMark Microplate, Spectrofluorometer Biorad, Milan, Italy). Data were expressed as the percentage of NF-κB/p65 DNA binding relative to untreated cells.

Quantification of pro-inflammatory interleukins

The expression of Interleukin-6, and Interleukin-1β in cardiomyocytes and hepatocytes was evaluated with ELISA method, as described elsewhere[51]. Briefly, cells were grown under standard conditions as described in paragraph 2.3. After incubation for 24 h and starvation in serum-free medium for 2.5 h, cells were treated or not with unformulated or formulated CoQ_{10} for 4h before exposure to doxorubicin or trastuzumab (200 nM) for 12 h. After, culture supernatants were centrifuged to pellet any detached cells and measured using IL-1β, IL-6, ELISA kits according to the manufacturer's instructions (Sigma Aldrich, Milan, Italy). The sensitivity of this method was below 10 (pg/mL), and the assay accurately detected cytokines in the range of 1–32000 pg/mL.

Statistical studies

All the values were reported as ± Standard Deviation; the differences between the experimental groups were identified with a one-way analysis of variance and subsequently with Tukey's multiple comparison tests in Sigma Plot Software. $p < 0.05$ was the lowest acceptable threshold for significance.

References

1. Coleman, M. P. *et al.* Cancer survival in Australia, Canada, Denmark, Norway, Sweden, and the UK, 1995-2007 (the international cancer benchmarking partnership): An analysis of population-based cancer registry data. *Lancet* **377**, 127–138 (2011).

2. Youssef, G. & Links, M. The prevention and management of cardiovascular complications of chemotherapy in patients with cancer. *American Journal of Cardiovascular Drugs* **5**, 233–243 (2005).

3. Yeh, E. T. H. & Bickford, C. L. Cardiovascular complications of cancer therapy: incidence, pathogenesis, diagnosis, and management. *Journal of the American College of Cardiology* **53**, 2231–2247 (2009).

4. Yeh, E. T. H. *et al.* Cardiovascular complications of cancer therapy: diagnosis, pathogenesis, and management. *Circulation* **109**, 3122–31 (2004).

5. Jerusalem, G., Lancellotti, P. & Kim, S. B. HER2+ breast cancer treatment and cardiotoxicity: monitoring and management. *Breast Cancer Research and Treatment* **177**, 237–250 (2019).

6. Damodar, G., Smitha, T., Gopinath, S., Vijayakumar, S. & Rao, Y. An evaluation of hepatotoxicity in breast cancer patients receiving injection doxorubicin. *Ann. Med. Health Sci. Res.* **4**, 74 (2014).

7. Geisberg, C. A. & Sawyer, D. B. Mechanisms of anthracycline cardiotoxicity and strategies to decrease cardiac damage. *Current Hypertension Reports* **12**, 404–410 (2010).

8. Nowsheen, S. *et al.* Incidence, Diagnosis, and Treatment of Cardiac Toxicity From Trastuzumab in Patients With Breast Cancer. *Current Breast Cancer Reports* **9**, 173–182 (2017).

9. Ishizuna, K., Ninomiya, J., Ogawa, T. & Tsuji, E. Hepatotoxicity induced by trastuzumab used for breast cancer adjuvant therapy: a case report. *J. Med. Case Rep.* **8**, 417 (2014).

10. Bria, E. *et al.* Cardiotoxicity and incidence of brain metastases after adjuvant trastuzumab for early breast cancer: The dark side of the moon? A meta-analysis of the randomized trials. *Breast Cancer Research and Treatment* **109**, 231–239 (2008).

11. Chen, J. *et al.* Incidence of heart failure or cardiomyopathy after adjuvant trastuzumab therapy for breast cancer. *J. Am. Coll. Cardiol.* **60**, 2504–2512 (2012).

12. Han, X., Zhou, Y. & Liu, W. Precision cardio-oncology: understanding the cardiotoxicity of cancer therapy. *npj Precis. Oncol.* **1**, (2017).

13. Guglin, M. *et al.* Randomized Trial of Lisinopril Versus Carvedilol to Prevent Trastuzumab Cardiotoxicity in Patients With Breast Cancer. *J. Am. Coll. Cardiol.* **73**, 2859–2868 (2019).

14. Tarantini, L. *et al.* Trastuzumab adjuvant chemotherapy and cardiotoxicity in real-world women with breast cancer. *J. Card. Fail.* **18**, 113–119 (2012).

15. Mohan, N., Jiang, J., Dokmanovic, M. & Wu, W. J. Trastuzumab-mediated cardiotoxicity: current understanding, challenges, and frontiers. *Antib. Ther.* **1**, 13–17 (2018).

16. Hepatotoxicity Secondary to Chemotherapy. *J. Clin. Transl. Hepatol.* **2**, (2014).

17. Sharma, A., Fonarow, G. C., Butler, J., Ezekowitz, J. A. & Felker, G. M. Coenzyme Q10 and heart failure. *Circ. Hear. Fail.* **9**, (2016).

18. Littarru, G. P. & Tiano, L. Bioenergetic and antioxidant properties of coenzyme Q10: Recent developments. in *Molecular Biotechnology* **37**, 31–37 (2007).

19. Zhang, P.-Y., Xu, X., Li, X.-C. & Zhang, P. *Cardiovascular diseases: oxidative damage and antioxidant protection*.

20. Botelho, A. F. M. *et al.* Coenzyme Q10 Cardioprotective Effects Against Doxorubicin-Induced Cardiotoxicity in Wistar Rat. *Cardiovasc. Toxicol.* (2019).

21. Bhagavan, H. N. & Chopra, R. K. Plasma coenzyme Q10 response to oral ingestion of coenzyme Q10 formulations. *Mitochondrion* **7**, (2007).

22. Jordan, A. R., Racine, R. R., Hennig, M. J. P. & Lokeshwar, V. B. The role of CD44 in disease pathophysiology and targeted treatment. *Frontiers in Immunology* **6**, (2015).

23. Suleiman, M., Abdulrahman, N., Yalcin, H. & Mraiche, F. The role of CD44, hyaluronan and NHE1 in cardiac remodeling. *Life Sciences* **209**, 197–201

(2018).

24. Krolikoski, M., Monslow, J. & Puré, E. The CD44-HA axis and inflammation in atherosclerosis: A temporal perspective. *Matrix Biology* **78–79**, 201–218 (2019).

25. Vecchione, R. *et al.* Tunable stability of monodisperse secondary O/W nano-emulsions. *Nanoscale* **6**, 9300–9307 (2014).

26. Vecchione, R. *et al.* Ultrastable Liquid–Liquid Interface as Viable Route for Controlled Deposition of Biodegradable Polymer Nanocapsules. *Small* **12**, 3005–3013 (2016).

27. Maurea, N. *et al.* Pathophysiology of cardiotoxicity from target therapy and angiogenesis inhibitors. *J. Cardiovasc. Med.* **17**, S19–S26 (2016).

28. D., M. *et al.* Pathophysiology of anthracycline cardiotoxicity. *J. Cardiovasc. Med.* **17**, S3–S11 (2016).

29. Robison, T. W. & Giri, S. N. Effects of chronic administration of doxorubicin on plasma levels of prostaglandins, thromboxane B2, and fatty acids in rats. *Cancer Chemother. Pharmacol.* **19**, 213–20 (1987).

30. Wang, L. *et al.* Doxorubicin-induced systemic inflammation is driven by upregulation of toll-like receptor TLR4 and endotoxin leakage. *Cancer Res.* **76**, 6631–6642 (2016).

31. Luedde, T. & Schwabe, R. F. NF-κB in the liver-linking injury, fibrosis and hepatocellular carcinoma. *Nature Reviews Gastroenterology and Hepatology* **8**, 108–118 (2011).

32. Van Der Heiden, K., Cuhlmann, S., Luong, L. A., Zakkar, M. & Evans, P. C. Role of nuclear factor κB in cardiovascular health and disease. *Clinical Science* **118**, 593–605 (2010).

33. Liu, T., Zhang, L., Joo, D. & Sun, S. C. NF-κB signaling in inflammation. *Signal Transduction and Targeted Therapy* **2**, (2017).

34. Momenimovahed, Z. & Salehiniya, H. Epidemiological characteristics of and risk factors for breast cancer in the world. *Breast Cancer: Targets and Therapy* **11**, 151–164 (2019).

35. Rugo, H. S. Achieving improved survival outcomes in advanced breast cancer. *New England Journal of Medicine* **381**, 371–372 (2019).

36. Varga, Z. V., Ferdinandy, P., Liaudet, L. & Pacher, P. Drug-induced

mitochondrial dysfunction and cardiotoxicity. *American Journal of Physiology - Heart and Circulatory Physiology* **309**, H1453–H1467 (2015).

37. Zhang, X. *et al.* Role of oxidative stress in cardiotoxicity of antineoplastic drugs. *Life Sciences* **232**, (2019).

38. Cuomo, A. *et al.* Heart Failure and Cancer: Mechanisms of Old and New Cardiotoxic Drugs in Cancer Patients. *Card. Fail. Rev.* **5**, 112–118 (2019).

39. Sosnowska, B., Penson, P. & Banach, M. The role of nutraceuticals in the prevention of cardiovascular disease. *Cardiovascular Diagnosis and Therapy* **7**, S21–S31 (2017).

40. Morisco, C., Trimarco, B. & Condorelli, M. Effect of coenzyme Q10 therapy in patients with congestive heart failure: a long-term multicenter randomized study. *Clin. Investig.* **71**, S134-6 (1993).

41. Mortensen, S. A. *et al.* The effect of coenzyme Q10 on morbidity and mortality in chronic heart failure: Results from Q-SYMBIO: A randomized double-blind trial. *JACC Hear. Fail.* **2**, 641–649 (2014).

42. Heck, A. M., DeWitt, B. A. & Lukes, A. L. Potential interactions between alternative therapies and warfarin. *Am. J. Heal. Pharm.* **57**, 1221–1230 (2000).

43. Vitetta, L. *et al.* The plasma bioavailability of coenzyme Q 10 absorbed from the gut and the oral mucosa. *J. Funct. Biomater.* **9**, (2018).

44. Vecchione, R. *et al.* Curcumin bioavailability from oil in water nano-emulsions: In vitro and in vivo study on the dimensional, compositional and interactional dependence. *J. Control. Release* **233**, 88–100 (2016).

45. Quagliariello, V. *et al.* Hyaluronic Acid Nanohydrogel Loaded With Quercetin Alone or in Combination to a Macrolide Derivative of Rapamycin RAD001 (Everolimus) as a New Treatment for Hormone-Responsive Human Breast Cancer. *J. Cell. Physiol.* **232**, 2063–2074 (2017).

46. Pal, A. K., Bello, D., Budhlall, B., Rogers, E. & Milton, D. K. Screening for Oxidative Stress Elicited by Engineered Nanomaterials: Evaluation of Acellular DCFH Assay. *Dose-Response* **10**, dose-response.1 (2012).

47. Darrabie, M. D. *et al.* Exposing cardiomyocytes to subclinical concentrations of doxorubicin rapidly reduces their creatine transport.

Am. J. Physiol. Circ. Physiol. **303**, H539–H548 (2012).

48. Quagliariello, V. *et al.* Low doses of Bisphenol A have pro-inflammatory and pro-oxidant effects, stimulate lipid peroxidation and increase the cardiotoxicity of Doxorubicin in cardiomyoblasts. *Environ. Toxicol. Pharmacol.* **69**, 1–8 (2019).

49. Quagliariello, V. *et al.* Cardiotoxicity and pro-inflammatory effects of the immune checkpoint inhibitor Pembrolizumab associated to Trastuzumab. *Int. J. Cardiol.* **292**, 171–179 (2019).

50. Poulaki, V. *et al.* Constitutive nuclear factor-kappaB activity is crucial for human retinoblastoma cell viability. *Am. J. Pathol.* **161**, 2229–40 (2002).

51. Quagliariello, V. *et al.* Cardioprotective Effects of Nanoemulsions Loaded with Anti-Inflammatory Nutraceuticals against Doxorubicin-Induced Cardiotoxicity. *Nutrients* **10**, 1304 (2018).

CHAPTER 6: Conclusions and outlooks

The application of nanotechnology in the drug delivery field for cancer therapy was the topic of this PhD thesis, with particular focus on the active targeting.

Nanocapsule-based delivery systems provide new opportunities to overcome the limitations associated with traditional drug therapy. The efficiency of drug delivery to target a tumor site is dependent on the NCs physic-chemical properties. In particular, it is important for the delivery platform to selectively accumulate in the site of interest avoiding any clearance by the mononuclear phagocyte system. To this aim, in this PhD thesis, the effort was to design and develop a basic nanocarrier that could then be funtionalized for active targeting on their surface with specific peptides depending on the final application. In particular, firstly the development of a novel multi-functional emulsion based nanocapsules made of biocompatible and biodegradable materials and stabilized by natural polymeric deposition by layer-by-layer protocol around O/W NEs were presented. We obtained a product with a narrow particle size distribution of around 100 nm, stable enough to build up dimensionally controllable multilayer nanocapsules of interest for nanomedicine. O/W NEs are an ideal carrier for drug delivery because of their capability to dissolve several hydrophobic drugs and natural substances like curcumin and coenzyme Q_{10}, and protect their cargo from hydrolysis and enzymatic degradation under physiological conditions. Then, the system was rendered "smarter" introducing as targeting moieties first a peptide able to recognize CD44 receptor, highly over-expressed in many kind of cancers, and then, to show the versatility of the tool, a peptide able to recognize transferrin receptor (TfR), a well known target for the blood brain barrier (BBB). The

peptides were attached outside the carrier thanks to a safe additive decoration strategy, which avoids any purifications step and use of potential toxic chemicals. Our *in vitro* results clearly demonstrate the ability of peptide functionalized NCs to target specifically tumor cells thanks to peptide-receptor recognition that induces their internalization and subsequently release of the cargo. In the last part of the PhD project, it was investigated the use of O/W NEs to support oncological patients during the clinical treatment, demonstrating the cardioprotective and hepatoprotective effects of Coenzyme Q_{10} loaded O/W NEs against Doxorubicin and Trastuzumab toxicities, widely used during anticancer treatments. The future upgrade for these applications is the functionalization of the nanocarrier with peptides able to selectively target liver and cardiovascular tissues so that the nanocarrier can work not only in a 2D culture but also in vivo by accumulating in the tissues of interest. A targeting peptide (CREKA) with potential applications in the field of cardiovascular disease has been already identified and it will be integrated to our NCs. Definitely, during this PhD project, we provided a modular system, which may add complexity by exploiting its capability to further deposit layers and provide multi-compartmentally and therefore multi-functionality. It holds promise as a useful tool to improve therapeutic efficacy for several anti-cancer treatments and for prevention treatment of support for oncological patients.

List of abbreviation

BBB	Blood–brain barrier
CD44	Cluster of differentiation 44
CD44BP	CD44 binding peptide
CMC	Critical micelle concentration
CNT	Carbon nanotubes
CPP	Cell-penetrating peptides
CSC	Cancer stem cells
CT	Chitosan
DDS	Drug delivery systems
ECM	Extracellular matrix
EGFR	Epidermal growth factor receptor
EPR	Enhanced permeability and retention
GAG	Glycosaminoglycan
GI	Gastrointestinal tract
GRAS	Generally recognized as safe
HA	Hyaluronic acid
HF	Heart failure
i.e.	id est
IKK	IκB kinase
ITC	Isothermal titration calorimetric
LbL	Layer-by-Layer
mAB	Monoclonal antibodies
MPS	Mononuclear phagocyte system
MSN	Mesoporous silica nanoparticles

MFI	Mean fluorescence intensity
NCs	Nanocapsules
NE	Nanoemulsions
NF-κB	Nuclear factor kappa-light-chain-enhancer of activated B cells
NP	Nanoparticles
O/W	Oil in water
PEG	Poly(ethylene glycol)
PTX	Paclitaxel
QD	Conductive nanocrystals
RES	Reticuloendothelial system
RMT	Receptor-mediated transcytosis
SPION	Super Paramagnetic Iron Oxide Nanoparticles
SPR	Surface plasmon resonance
Tf	Transferrin
TfR	Transferrin receptor
uPA	Urokinase plasminogen activator
VEGFR	Vascular endothelial growth factor receptor
W/O	Water in oil